

Paul Goldberg, Shannon J.P. McPherron, Harold L. Dibble,
and Dennis M. Sandgathe

Introduction

From the outset of the Pech IV project, geoarchaeology played an integral role in the excavations. In addition to performing detailed field observations, much of the geoarchaeological analyses employed the technique of archaeological micromorphology. In addition, observations made on the archaeological material that have relevance to site formation processes are discussed in this chapter. These observations include artifact orientations, edge damage, burning and breakage of lithic artifacts, and an analysis of

the small lithics fraction (5–25 mm) coming from the screens.

Principally, we focused on a number of aspects of the site including:

- (1) Detailed microstratigraphic observation and recording of the deposits, particularly noting lateral variations through time;
- (2) Correlation of the revised stratigraphy with that developed by F. Bordes from his excavations in the 1970s;
- (3) Reconstruction of site formation history, documenting geogenic processes, anthropogenic activities, as well as post-depositional, and syn-depositional processes;
- (4) Establish temporal relationships among Pech I, II, and IV based on the stratigraphic observations and analyses.

P. Goldberg (✉)

School of Earth and Environmental Sciences, Centre for Archaeological Science, University of Wollongong, Wollongong, NSW 2522, Australia
e-mail: paulberg@bu.edu

P. Goldberg

Institute for Archaeological Sciences, Eberhard Karls Universität Tübingen, Tübingen, Germany

P. Goldberg

Department of Archaeology, Boston University, Boston, USA

S.J.P. McPherron · H.L. Dibble

Department of Human Evolution, Max Planck Institute for Evolutionary Anthropology, Leipzig, Germany
e-mail: mcpherron@eva.mpg.de

H.L. Dibble

e-mail: hdibble@sas.upenn.edu

H.L. Dibble

Department of Anthropology, University of Pennsylvania, Philadelphia, PA, USA

H.L. Dibble

School of Human Evolution and Social Change, Institute for Human Origins, Arizona State University, Tempe, AZ, USA

D.M. Sandgathe

Department of Archaeology and Human Evolution Studies Program, Simon Fraser University, Burnaby, BC, Canada
e-mail: dms@sfu.ca

D.M. Sandgathe

Museum of Archaeology and Anthropology, University of Pennsylvania, Philadelphia, USA

Site Setting

As described in Chap. 1, the Pech sites are situated along the cliffs of a small dry valley (the Farge), about 5 km SE of the town of Sarlat-la-Canéda. The bedrock of Pech de l'Azé is part of Upper Coniacian yellow sandy bioclastic limestone (Unit C4b), composed of subangular quartz, muscovite, some glauconite, and rounded microfossils (Capdeville and Rigaud 1987) (<http://infoterre.brgm.fr/>). All of the Pech de l'Azé sites are associated with erosion of an anticlinal ridge of mostly Mesozoic limestones during the Oligocene, Miocene, and Pliocene, with karstic dissolution along joints during the Quaternary (Salomon and Astruc 1992; Turq et al. 2011); evidence of numerous solution cavities—some of which are exploited commercially—occur in the vicinity. Figure 2.1 shows the general alignment of Pech I, II, and IV, which reflects karstic development along the same structural axis; minor jointing that parallels this axis was observed in the bedrock floor of Pech IV.

Bordes originally described Pech IV as a collapsed rockshelter, presumably based on its morphology: a steep

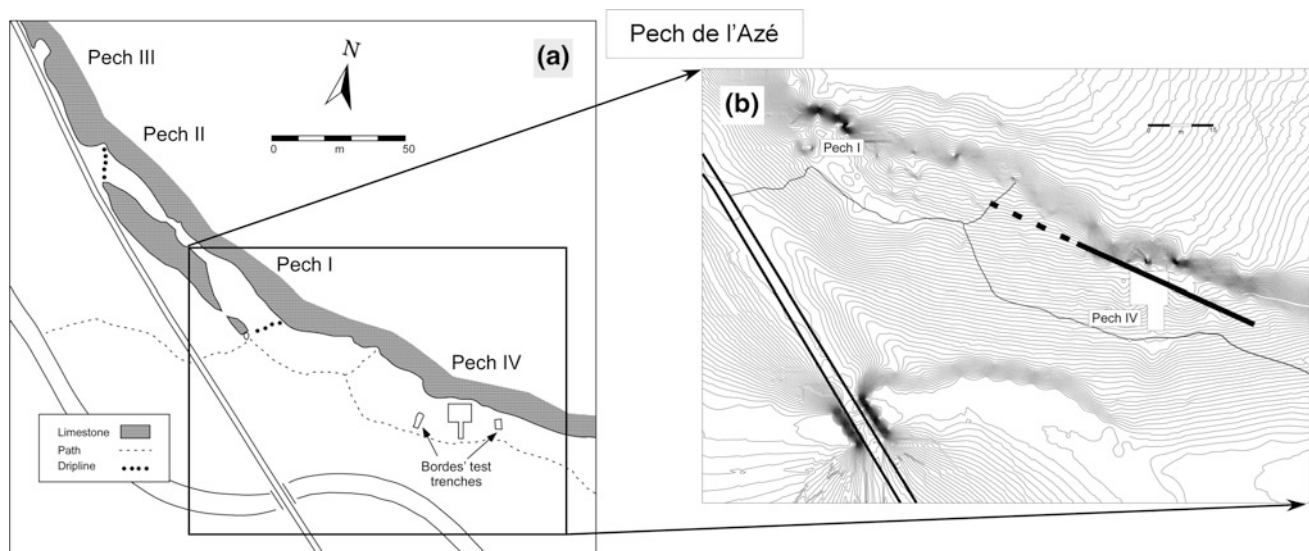


Fig. 2.1 a Four sites of Pech de l'Azé. Note that Pech IV generally follows the orientation of the chamber connecting Pech I and II. b Topographic map of the Pech IV site before the recent excavations.

The line depicts the limits of the north wall of the cave; dashed lines indicate the projection of the cave concealed under slope fill

bedrock wall at the back (north) with the remains of a small bedrock overhang just above the excavation. Our recent research, however, has revealed that Pech IV is most likely a collapsed cave connected to the karstic system associated with that of Pech I and II (Fig. 2.1). Supporting evidence for this inference is discussed below, but here it briefly includes the position of large blocks of roof collapse visible in the south, west, and east areas of the excavations, coupled with deposits that locally slope from north to south (i.e., from the inside of the inferred cave interior towards the entrance), and fabric (orientation) analyses (see below). Finally, fist-sized remnants of dripstone derived from the original cave roof were found within the lower deposits; these would not form in an aerated space such as that of an open rockshelter.

Thus, erosion of the valley—somewhat oblique to the axis of the Pech I, II, and IV (Fig. 2.1)—has caused the retreat of the cave mouth of Pech IV, resulting in its appearance as a rockshelter with coarse limestone block remnants representing a collapsed overhanging roof. A similar picture can be seen at Pech I today (Soressi et al. 2013), though in this case the southern portion of the cave wall is largely intact.

Stratigraphy

Bordes' original description of the deposits encompassed a mixture of lithology and lithic industries within the different layers (Bordes 1975) (see Chap. 1; Table 2.1), although he never published a detailed and systematic lithological description of these units. The stratigraphic subdivision of the deposits from the current excavations consists of eight major geological units which are subdivided into a total of

13 layers, and their relationship to the levels identified by Bordes is shown in Table 2.2. The current stratigraphic divisions are based on lithostratigraphy using the criteria of color, composition, texture, grain morphology, internal structure, and lateral and vertical changes (Fig. 2.3).

As can be seen in Fig. 2.4a and Table 2.2, there is general similarity between our units and his, and a number of layers generally overlap or correspond to those of Bordes. However, since our sequence is based on different exposures from the ones seen by him (his section drawing is along the 15 column, or 4 m east of our West Section drawing), some localized mismatches are to be expected. Nevertheless, as can be seen in Fig. 2.4b, despite some mismatches and lensing/pinching out of layers, the stratigraphic units are traceable across the entire expanse of both excavations. Consequently, we are confident with Bordes' overall sequence, our correlations with it, and its lateral variations.

The deposits described below are based mostly on observations during our excavations (squares C11 through H13—best illustrated in the West and South Sections), as well as the witness sections left by Bordes: a corridor of excavated squares that act as access to the site (the 15 line) and a section in the eastern part of the excavations (Figs. 2.2 and 2.3). Below is a general summary of the stratigraphy at the end of the recent excavations (Fig. 2.4).

Micromorphological Methods

As discussed below, our work at Pech IV concentrated on comprehensive examination of the deposits exposed in Bordes' and our sections in order to identify Bordes' original

Table 2.1 Pech de l'Azé IV—Summary of Bordes' stratigraphy (Bordes 1975)

Level	Lithology/geology	Industry
A1	Brown sand and éboulis with modern vegetation	Poor in lithics. Medieval
A2	Brown sand and éboulis	Iron age to Medieval
B	Brown sand and éboulis	Traces of Mousterian
C	Brown sand and éboulis	Traces of Mousterian
D	Reddish sand with éboulis	Richer in lithics
E	Reddish sand with éboulis	Similar to D but fewer lithics
• F1	Rich in finer éboulis at the rear and medium-sized éboulis at the front. Subdivided in four subunits somewhat arbitrarily	• F1: MTA (B)
• F2		• F2: MTA (B)
• F3		• F3?: MTA (A-B)
• F4	Erosional pockets at the base	• F4: MTA (A)
G	(not stated)	Mousterian
H	Sand with scattered éboulis	Few tools; Typical and Mousterian?
• I1	Finer éboulis, locally strongly cemented. I2 becomes redder and softer toward the cliff at the rear of the cave	Typical Mousterian
• I2		
• J1	• J1: light reddish brown sand with large limestone blocks from roof collapse	Typical Mousterian?
• J2	• J2: Éboulis rounded by cryoturbation, with broken flints in a sandy matrix. Toward the back, the éboulis is more angular and the lithics are almost intact	• J2: Typical Mousterian?
• J3	• J3 (subdivided into a, b, c): loose sand poor in éboulis, rich in worked lithics; traces of hearths; it is red at the top, becoming gray and black toward its base. Rests on large slabs of limestone from the roof	• J3: Typical Mousterian
• J3a		• J3a-c: Asinipodian
• J3b		
• J3c		
X	Underlies blocks of J3 and is black to gray; abundant broken and cryoturbated flint. Laterally, intercalated with dark brown layer containing traces of fireplaces	Typical Mousterian
Y	Reddish and found in the front of the cave; toward the rear it appears to be replaced by roof collapse	Typical Mousterian
Z	Rests on bedrock, which is locally reddened by fire	Typical Mousterian

stratigraphic divisions (Bordes 1975) and bring them up to date. Nevertheless, there is only so much sedimentary and stratigraphic information that can be gleaned from field observations, no matter how diligent one tries to be. In order to supplement these observations in our interpretations of site formation processes, we employed micromorphology, which is the study of undisturbed sediments and soils—predominately in thin section—using a petrographic microscope (Courty et al. 1989). Since it is concerned with the microcontextual attributes of sedimentary and soil features and objects (e.g., bones, flints, charcoal) (Goldberg and Berna 2010), micromorphology is effective in reconstructing the formation of natural and archaeological layers and soils (Goldberg and Macphail 2006).

About 200 samples were collected as large intact blocks of sediment using the procedures outlined in Goldberg and Macphail (2003). These blocks were wrapped tightly in the field with tissue paper and packaging tape, and their coordinates were recorded using a total station and integrated into the site database (McPherron et al. 2005); loose, bulk sediment samples were also collected. The sample blocks were transported to Boston University, and then oven dried for one week at 60 °C. The samples were impregnated with a mixture of polyester resin and styrene (7:3) catalyzed with MEKP and allowed to harden for ~4–5 days. The hardened blocks were again heated in the oven overnight at 60 °C, then trimmed and sliced using a diamond blade rock saw. At this time, areas were identified for thin section analysis and

Table 2.2 Approximate correlation between Bordes' levels and the geological layers used here

Bordes level	Our layers
A-E	1, 2
F ₁	3A
F ₂	
F ₃	
F ₄	3B
G	4A
H ₁ /H ₂	4B
I ₁	4C
I ₂	
J ₁	
J ₂	5B
J ₃	6A
J ₃ A	
J ₃ B	
J ₃ C	6B
X	7
Y	8
Z	

they were prepared into thin sections, 50 × 75 mm with a thickness of 30 μm.

About 130 thin sections were made from the samples collected in 2001, 2002, and 2003 (Table 2.3). The sections were scanned on a flatbed scanner (Arpin et al. 2002) and examined with stereoscopic and petrographic microscopes at varying magnifications and illuminations: plane-polarized light (PPL), cross-polarized light (XPL), and dark field illumination; in addition, some were observed using blue light epi-fluorescence. Oblique incident light was used in some cases to distinguish organic material from charcoal and burned bone from stained bone (Courty et al. 1989). Descriptive nomenclature follows that in (Stoops 2003) and (Courty et al. 1989).

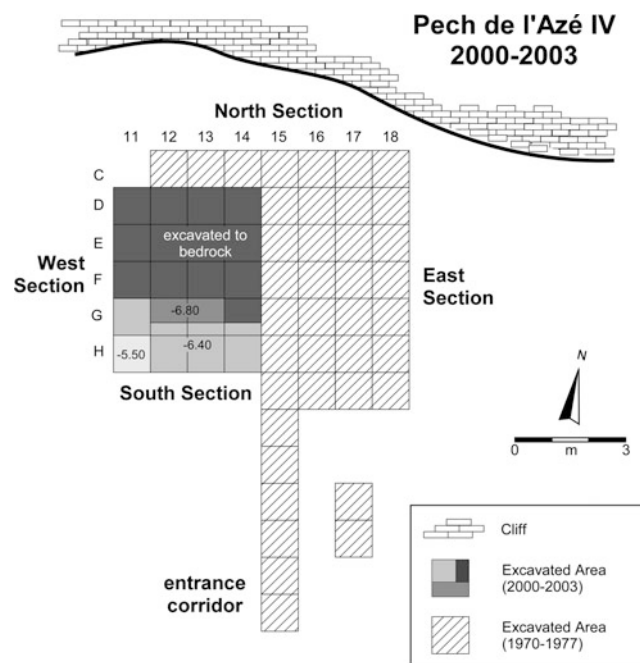
Results

Layer 8 (≡Bordes' Levels YZ)

Bordes originally identified three mostly anthropogenic basal layers (X, Y, and Z) above the bedrock that were similar in archaeological composition. He described them as burned areas and stated that the “bedrock is strongly rubefied by fire (Bordes 1975: 294).” He also distinguished the layers on the basis of texture: the first, X (roughly equivalent to our Layer 7), was “blackish gray with cryoturbated layers at the top”; the second, Y (the upper part of our Layer 8), was a “reddish layer at the front of the shelter that grades into *éboulis* toward the interior”; and the third, Z (the base of our Layer 8), was described as “resting on bedrock and reddened by fire”. In light of the fact that it is difficult to clearly differentiate among them, we have grouped the lower two layers (Y and Z) into one major unit, Layer 8.

Overall, Layer 8 consists of massive to coarsely bedded dark reddish brown, greasy clayey, organic-rich silty sand with burned bone (some calcined) and flint, with little rock fall. The darkest levels are exposed along the west side of the entrance section, particularly in squares G-H 14 (Figs. 2.3, 2.5 and 2.6). The base of the layer is locally cemented by carbonate (see below), whereas the top of the layer exhibits a marked increase in abundance of anthropogenic components (Fig. 2.7). This layer is especially prominent in the south-western portion of the site (squares G-H-I, 12-13-14; Figs. 2.3 and 2.5), where it is thickest (~45–50 cm); however, it thins laterally to the north and south: it pinches out to the north along the D squares, just at the location where the bedrock floor rises, and it does not extend to the rear wall of the cave (Figs. 2.3 and 2.4).

Along the E, D, and I rows of squares, the organic zones interfinger with lighter brown, noncalcareous sand, whereas organic-rich sands are well exposed to the west along the F/G line indicating that the intense use of fire continued along this direction but not much to the north and south.

**Fig. 2.2** Plan of site, showing grid, location of excavated squares, depth to which different sections were excavated, and the main sections discussed in the text

preparation, and in the case of a large sample, multiple thin sections were made. The trimmed blocks were shipped to Spectrum Petrographics (Vancouver, WA, USA), where



Fig. 2.3 **a** General view of Pech IV showing clockwise, the South, West, and North Sections, respectively. *Arrow* points to red circular stain on bedrock thought by Bordes to represent the effects of burning. The dark layer resting on bedrock (Sq. H12-14) is Layer 8, which pinches out to the north (*right*) as the bedrock floor rises. The remains of large blocks of excavated roof fall constitute the main part of the South wall and cover layers 7 and 8. **b** West wall of Pech IV showing stratigraphic units of the current excavations and those of Bordes. Note the increased proportion of sandy sediments toward the north (*right*), particularly in Layers 4 and 3. **c** Detailed view of lower part of West Section and part of the South Section at *lower left*. Note the pinching out of Layer 8 at the base, the slope of the bedrock floor to the *left* (south), and the angular rock fall in the base of Layer 6

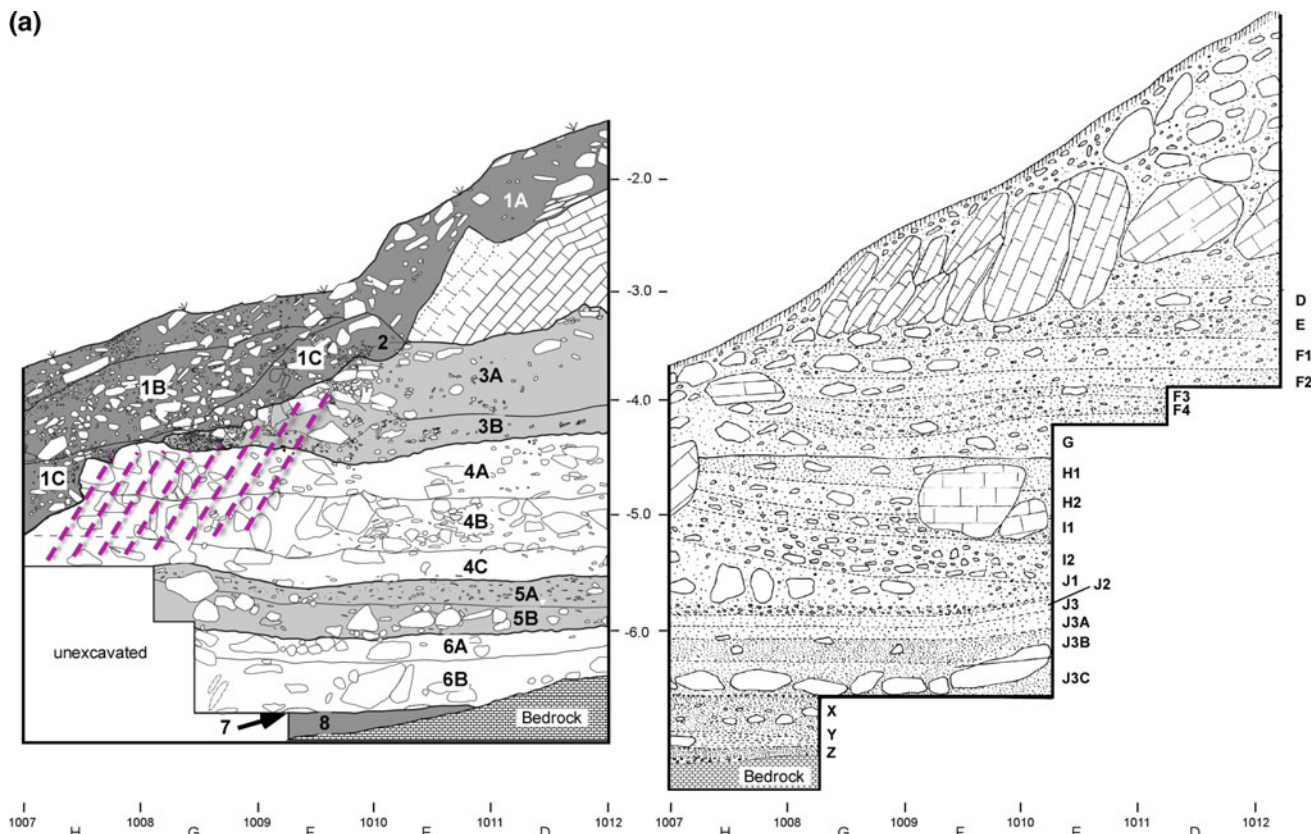
They appear to be concentrated under the large blocks of unexcavated rock fall occurring in the block of squares defined from G12 to I14 and represent the locus of repeated burning activity, which took place just inside the cave beneath the former dripline/brow (Figs. 2.3a and 2.5d).

It is important to note that the overall dark color of Layer 8, particularly where it occurs as cm-thick black organic bands and stringers (Fig. 2.7), reflects not so much the presence of charcoal, but that of char (gelified organic matter or fat from bones and meat formed by burning) (Ligouis 2006; Villagran et al. 2013) (Figs. 2.8b, d and 2.9a–c); in fact, it is this char that provides the “greasy” feel of the deposits in the field. Moreover, some of the darker bands are capped by thin, cm-thick bands of ash (Fig. 2.9d), and a number of them (especially in Sq. E13) tend to be cemented (Fig. 2.9d and 2.10c–f). This punctuated induration of only the ashes suggests that they were cemented relatively rapidly after deposition (Berna and Goldberg 2008; Madella et al. 2002), as the other sediments between them are not cemented. In any case, most of these couplets of dark band/ash represent in situ hearths/fires/burning events. On the other hand, parts of Layer 8 that consist of more diffuse dark bands or an overall homogeneous “dark” deposit (e.g., Fig. 2.9) are products of hearth rake out, locally accompanied by trampling whereby previously combusted materials were spread out before the next burning event took place.

In addition to the above, other localized microfacies variations occur in Layer 8. Along the south face of square F13, for example, 3–4-cm-thick red (2.5YR5/6) bands occur (Figs. 2.8c and 2.9a–f). At first, these were thought to be rubefied layers resulting from heating by fire. However, one 5-cm-thick continuous band (Fig. 2.9a, b) appears to be too thick to be caused simply by heating, especially over such a wide lateral extent. Such colorations were also found on the bedrock floor of the cave (Figs. 2.3a and 2.9c) and were similarly noted by (Bordes 1975). Finally, the fact that red coloration was observed to cut across the natural bedding suggests that at least part of the reddening is a post-depositional effect, possibly tied to oxidation of the organic matter in these lowermost layers (Karkanas et al. 2002).

Lastly, the basal part of Layer 8, which rests on bedrock, is locally cemented with micrite and microsparite, possibly, or at least in part, representing recrystallized ashes. Moreover, the sediment in these cemented areas is locally porous, with vesicles and channels within a compact matrix (Fig. 2.11). Presumably, these phenomena are tied to water flow that was concentrated along floor of the cave, as the overlying deposits above these basal 10–15 cm are not

(a)



(b)

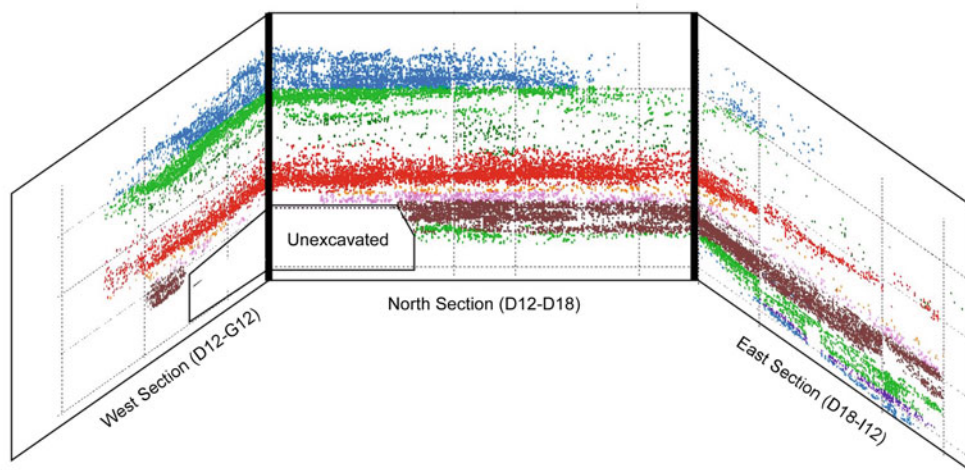


Fig. 2.4 **a** *Left* Drawing of West section showing the stratigraphic units used in the current project. The *diagonal hatching* indicates strong secondary calcite cementation of the deposits, demarcating the former positions and retreat of the dripline (see text). *Right* Bordes' West

section, which is approximately 3–4 m east of our final West Section. **b** *Panel diagram* showing lithic projections on three sections, colored by level, showing the lateral continuity across the site

cemented except for localized calcification of ashes (Fig. 2.11).

Layer 7 (=The Uppermost Part of Bordes' Level X)

Bordes (1975) noted the presence of a ca. 5 cm unit of angular, worn, and abraded flints at the top of his XYZ sequence (Figs. 2.7e and 2.12). We decided to separate this

thin, lithologically distinct unit from Bordes' Layer XYZ because of its generally geogenic character, lack of organic matter, and its lighter color. Overall, Layer 7 consists of cm-sized angular pieces of flint in a massive, strong brown (7.5YR5/8) sandy matrix; bones are relatively rare but also heavily rounded. Cryoturbated angular flint and bone-rich sand truncate Layer 8 in squares DEFG 13 and 14, but in

Table 2.3 Location and field descriptions of thin sections

Sample no.	Spectrum no.	Square	Layer	X	Y	Upper Z	Lower Z	Description
<i>2001</i>								
PDA-4-1	<i>LSI-1</i>	D11	3A	999.721	1011.25	−3.731	−3.731	Compact to weakly cemented clayey sand with flint chips and bone. Quite massive and homogeneous, with inclusions of rotten, rounded, cm-sized bedrock
PDA-4-2	<i>LSI-2; LSI-3</i>	F19	8	1006.56	1009.99	−6.812	−6.998	From very base of profile. Bottom ~3 cm weathered micaceous sandy limestone bedrock with some quartz that grades into and is overlain by dark reddish brown (5YR3/3 damp), noncalcareous, organic-rich “dirty” sand, somewhat washed. Much burned bone and flint. In one locality ca. 1 cm thick, locally concreted ash layer. Also, a few 1 cm diameter carbonate nodules/rhizoliths. Laterally, sediments are somewhat redder and look rubefied. In fact, on W entrance section, there are stringers of reddened sediment, charcoal and lighter zones that appear to be ash
PDA-4-3	<i>LSI-4; LSI-5</i>	F19	8	1006.61	1010.01	−6.802	−6.681	Organic-rich, greasy clayey/silty sand with abundant burnt flint and bone. Somewhat mottled and looks bioturbated, especially to S. Locally appears to be slightly rubefied (burrowed areas?). In all, appears to be burrowed hearth-like material. Organic-rich, greasy clayey/silty sand with abundant burnt flint and bone
PDA-4-4	<i>LSI-6; LSI-7</i>	E19	6B	1006.63	1010.16	−6.461	−6.655	Bottom of Layer J, including remains of decayed roof fall at bottom. Above roof fall, sediment consists of crumbly organic-rich sand with some clay. Looks somewhat similar to sample 4-3, but lighter color. Many roots, and some cm in diameter root concretions but otherwise is noncalcareous
PDA-4-5	<i>LSI-8</i>	F19	5B	1006.77	1009.79	−6.045	−6.192	Massive gritty clayey sand, locally with angular rockfall, bones, and flints, which are generally horizontal. Laterally quite extensive, although to N are larger rockfall. Possible clay translocation. Many pores and modern rootlets; some calcareous hypocoatings
PDA-4-6	<i>LSI-9</i>	F19	6	1006.79	1009.77	−6.218	−6.359	Similar to 4-5 but much stonier, with abundant bone and lithics. But overall, fine-grained matrix. Massive and laterally extensive but no bedding (trampled?)
PDA-4-7	<i>MNJ-24</i>	G19	8	1006.46	1008.74	−7.084	−7.165	Lightly stratigraphically lower than sample 4-2. About 4–5 cm thick of orangey sand in middle and black above and below. Black generally loose and rich in bone and roots. Appears burrowed

(continued)

Table 2.3 (continued)

Sample no.	Spectrum no.	Square	Layer	X	Y	Upper Z	Lower Z	Description
PDA-4-8	<i>LSI-10; MNJ-19</i>	D13	6B	1001.5	1011.23	−6.031	−6.136	From ledge of sediment on top of large tabular slabs of roof fall. Massive, soft, poorly sorted silty clay coarse sand with larger granule inclusions. Many flint chips which are commonly vertically oriented
PDA-4-9	<i>LSI-11</i>	F19	5B	1006.75	1009.68	−5.902	−5.983	About 10–15 cm thick. Poorly sorted sandy gravel, consisting of rounded and spherical 1 cm in diameter limestone gravel and about 2 cm subangular to sub-round gravel. Clearly eroded into Layer J and corresponds to early stage of roof collapse of the overlying blocks in Layer I. Back plots along the 18 line show somewhat lower densities, possibly because of erosion. Seems to represent small, localized channels, although difficult to determine direction of flow
PDA-4-11	<i>LSI-11</i>	E19	4C	1006.72	1010.37	−5.292	−5.415	Stony sand. Calcareous, massive and mixed with limestone blocks, varying from rounded cm-sized clasts to angular pieces about 1–5 cm across. Many roots. Locally cemented with calcite in broad zones. Many blackened bones; several flakes
PDA-4-12	<i>LSI-13</i>	E19	5A	1006.71	1010.6	−5.572	−5.641	Similar to sample 4-11 and is stratigraphically above 4-10 but ~80 cm to N and ~30 cm below sample 4-11. More cemented than 4-11 and several mm-sized (modern?) root casts of carbonate. Several unburnt bones
PDA-4-13	<i>LSI-14; LSI-15</i>	D13	4A	1006.84	1011.74	−4.758	−4.851	Weathering rind on bedrock consisting of 1: Yellow (10YR7/6) soft, calcareous (?) sand. Hard in upper part 2: Very pale brown (10YR8/4) chalky sand with many fine pores and roots. Looks like moon milk. Abundant fine roots at contact between 1 and 2 3: Similar to 1 and grades laterally from 2
PDA-4-14	<i>LSI-16</i>	D19	3	1006.82	1011.54	−4.579	−4.666	Additional transition sample with part closer to wall being similar to 4-13 (3). The part away from the wall is more compact sand, which is typical of the finer sediment in the shelter
PDA-4-15	<i>MNJ-20</i>	D19	3	1006.85	1011.18	−4.654	−4.745	Compact clay sand with rhizolithic concretions
PDA-4-17	<i>LSI-17</i>	E-19	3B	1006.86	1010.87	−4.686	−4.6	From gravelly pocket in the middle of E: compact mixture of weathered (phosphate rinds?) limestone clasts in a yellowish red (5YR 5/8) silty sand matrix. Matrix has fine pores and appears to be decalcifying. Limestone clasts vary from cm-sized rounded up to 8–10 cm flattish sub-rounded to subangular clasts, which are scattered throughout and are matrix supported. At base, some are

(continued)

Table 2.3 (continued)

Sample no.	Spectrum no.	Square	Layer	X	Y	Upper Z	Lower Z	Description
								horizontally bedded and perhaps in cryoturbation pockets. Entire feature is ~ 100 by 100 cm. Matrix on both sides of feature is similar red clayey sand
PDA-4-18	<i>LSI-18</i>	D19	5B	1006.75	1011.43	-5.771	-5.825	Similar to sample 4-15. Soft clayey sand. Mottled with localized clay concentrations as well as lighter washed zones. A few rare rhizoliths. Many roots. Looks like percolation zone
PDA-4-19	<i>LSI-19; LSI-45</i>	G19	4C	1006.71	1008.53	-5.399	-5.458	Just above large rock fall in Sq. F19; from stony sand just above this. Locally cemented. Collected between rock fragments
PDA-4-20	<i>LSI-20; LSI-21</i>	G11	4A	999.025	1008.8	-4.39	-3.96	Top of cemented zone beneath layers 1A and 1B that unconformably sits on it. Many flattish to circular, cm-sized stones. Clasts are rounded, some with weathered/AP(?) thin patchy rinds. Seems almost to be a laminar crust at the very top of W face
PDA-4-22	<i>LSI-23</i>	D11	3A	999.853	1011.67	-3.868	-3.96	About 35 cm below PDA-4-1, on N end of square. Here, sediments appear to be somewhat finer grained, i.e., greater proportion of matrix to weathered limestone debris. This matches the general trend of finer grained material closer to the N, rear wall
PDA-4-23	<i>LSI-24</i>	D11	3B	999.841	1011.73	-4.023	-4.124	From finer unit ca. 15 cm below sample 4-22. Soft clay sand with remnants of weathered limestone pieces. Some bone, flint chips. Becomes coarser to the south
PDA-4-24	<i>LSI-25; MNJ-21</i>	D11	4A	999.842	1011.91	-4.553	-4.702	Massive, dense clayey sand, with few artifacts
PDA-4-25	<i>LSI-26</i>	D11	4A	999.843	1010.95	-4.421	-4.368	At zone of interfingering between fine sandy facies and stony sandy facies. Vertically in between samples 4-23 and 4-24. Poorly sorted silty sand with some carbonate roots. Looks calcareous. Gets stonier to S
PDA-4-26	<i>NTO-002; NTO-003</i>	E11	3B	999.836	1010.65	-4.41	-4.285	Lateral equivalent to boundary across samples 4-23 and 4-25. Sample spans contact between finer sediment below and more angular limestone above. On freshly broken surface contact not clear but perhaps in thin section. Could be similar to sample 4-17 but fewer cryoturbation fragments appear. Angular bone and flint chips throughout. Limestone fragments appear weathered. Sample ~ 85-90 cm below I-2/I-3 contact

(continued)

Table 2.3 (continued)

Sample no.	Spectrum no.	Square	Layer	X	Y	Upper Z	Lower Z	Description
PDA-4-27	LSI-27	E11	3A			−3.768	−3.836	Appears to be a lobe-like mass that eroded into underlying 3. Seems to be oriented NW to SE. Sediment is crumbly, partly cemented calcareous silt sand with limestone clasts that are generally weathered and sub-rounded. Some roots. In hand lens looks partly decalcified and jumbled; possibly colluvium or solifluction
PDA-4-28	LSI-28	D11	4B	999.798	1011.53	−4.876	−4.967	Continuation of soft clay sand below sample 4-23. Very bottom could be in top of J as it is somewhat stony and lighter in color. Equivalent unit to S is stonier but some weathered stones here as well
PDA-4-29	LSI-29	D11	5A	999.623	1011.73	−5.575	−5.681	Soft crumbly sand with abundant bone and flint that seems clast supported. Somewhat darker than other samples but gives the same Munsell color of 5YR 5/8. Widespread across the site and rich in bone and flint but here it is burrowed either by animals or by <i>clandestins</i>
PDA-4-30	LSI-30	D11	4B	999.794	1011.01	−5.199	−5.266	Small sample from between stones of soft reddish sand. Some bone; locally quite stony
PDA-4-31	LSI-31	F11	5A	999.878	1009.94	−5.764	−5.813	Soft, crumbly bone-rich sand. Seems to be more calcareous than reddish sand but with same old color here. Bones are ~ cm in size, and some appear rounded and even polished (cryoturbation??). Black sediment on front part of sample could be terrier or related to wall construction
PDA-4-32	NTO-004; NTO-005	F11	6A	999.932	1009.79	−6.039	−6.158	Just below layer of loose rockfall. Upper part is coarse and grades to more sandy at base. Limestone pebbles quite rounded [probably by cryoturbation]. Rich in lithics and bones. Asinipodian layers
PDA-4-33	LSI-32	D11	5B	999.89	1011.26	−5.784	−5.861	Rocky sediment from cryoturbation level. Many well-rounded limestone pebbles and artifacts have worn appearance. Difficult to collect sample because of stoniness. The large sample with much padding might be somewhat disturbed. Also collected smaller sample of mostly fine clay sand between rockfall. This layer thickens to S and is below 4-31 and 4-32. Possibly equivalent layer of “gravel” in sample 4-9
PDA-4-34	LSI-33	H10	1A	999.009	1007.51	−3.777	−3.78	Clayey sand with many aggregates, roots, and tabular rock fragments with slabs measuring about 8 cm thick by about 30–40 cm across. Some more rounded cm-sized clasts

(continued)

Table 2.3 (continued)

Sample no.	Spectrum no.	Square	Layer	X	Y	Upper Z	Lower Z	Description
PDA-4-36	<i>LSI-34</i>	G10	4A	1008.16	-4.368	-4.368	-4.409	From and above contact with 3B. Two subsamples: upper (4-36) is composed of 1–2 cm in diameter, angular to sub-rounded limestone fragments produced by cryoturbation/solifluction. Subsample 36 bis is just below this and consists of cemented reddish sand with many fine pores and carbonate hypocoatings. Seems to be eroded by cryoturbation gravels
PDA-4-37	<i>LSI-35; LSI-36</i>	D18	8	1006.79	1011.77	-6.167	-6.327	From just above bedrock. “Greasy”, moist, organic sand. Many flints and bones, some of which are burnt. Some rockfall. Roughly equivalent to sample 4-4. To S gets slightly lighter color and looks bioturbated
PDA-4-38	<i>LSI-37</i>	Pech I	–	–	–	–	–	Cross-bedded Middle to Upper Coniacian sandstone collected from the wall made by Bordes in Pech I
PDA-4-39	<i>LSI-38</i>	Pech I	–	–	–	–	–	Lower Coniacian marly limestone from next to bike path below Pech I. Possibly bioturbated
PDA-4-40	<i>LSI-39; LSI-40</i>	D18	4A	1006.8	1011.51	-4.952	-5.076	Massive sand with some carbonate rhizoliths. Uppermost is coterminous with bottom of sample 4-13
PDA-4-42	<i>NTO-006; NTO-007</i>	D18	4C	1006.77	1011.58	-5.288	-5.397	Similar to 4-40 and -41 but perhaps richer in clay. In fact, appears to be broad domains of perhaps translocated clay. Perhaps darker (5YR5/6). Some flint at bottom, fewer rhizoliths. Perhaps sandy zone next to wall is produced by decalcification of sandy bedrock followed by translocation of clay
PDA-4-43	<i>LSI-41</i>	D18	5A	1006.78	1011.45	-5.516	-5.516	Same as -41 and -42 but, more modern roots; more flints, larger rhizoliths; clayey domains appear more prominent and larger
PDA-4-44	<i>NTO-008; NTO-009</i>	D18	5A	1006.79	1011.44	-5.618	-5.741	Between samples 4-34 and 4-18. Similar to others with abundant fine roots. Flints at an angle here and in sample -42 (bioturbation?). Clear clay band at bottom and clayey domains
PDA-4-45	<i>LSI-42</i>	E11	3A	999.831	1010.74	-3.613	-3.708	Soft, poorly sorted massive calcareous silty sand with modern roots; 1- to 4-cm-sized fragments of angular to rounded limestone. Flint and bone chips, many burnt. Could be soliflucted level and some cryoturbation
PDA-4-46	<i>MNJ-22</i>	E11	3A	999.822	1010.73	-4.076	-4.076	Generally similar to sample 4-45 but fewer roots, more compact and massive
PDA-4-47	<i>LSI-43; LSI-44</i>	E11	4A	999.825	1010.58	-4.504	-4.608	Transition between red sandy facies and stony sand facies. Some bone. A few cm-sized stones. Locally cemented. More stony to S

(continued)

Table 2.3 (continued)

Sample no.	Spectrum no.	Square	Layer	X	Y	Upper Z	Lower Z	Description
PDA-4-48	<i>NTO-010; NTO-011</i>	E11	4A	999.833	1010.35	-4.683	-4.779	Slightly lower and more stony than sample 4-47. Below layer of angular stones
PDA-4-49	<i>LSI-46; LSI-47</i>	F11	4B	999.891	1009.76	-4.816	-4.961	Fine, cm-sized limestone fragments in a sandy matrix. Large rock fall to the S. Looks like cryoturbation zone
PDA-4-50	<i>LSI-48; LSI-49</i>	F11	4A	999.449	1009.02	-4.614	-4.81	Large cemented block of breccia with bone, many pores, calcite hypocoatings that appear partially replaced by apatite. Pebbles about 1–2 cm in diameter. Looks like phosphatic vegetated spring deposit
PDA-4-51	<i>LSI-50; LSI-51; LSI-52; LSI-53</i>	E13	8	1001.92	1010.3	-6.603	-6.938	Massive to coarse bedded, greasy organic sand. Some cm-thick reddish levels. Between is ~3–7 cm sediments that are concreted with very finely crystalline, shiny cement. Very hard. Loose material is called “4-51 base.” Possible thin mm stringers of ash and darker bands of diffuse charcoal. Essentially similar to W part of entrance trench
PDA-4-52	<i>MNK-28</i>	E13	8	1001.8	1011.06	-6.54	-6.673	Organic-rich sand with weak brown/red bands. Much burnt flint and bone. Rests on hard, cemented band about 3 cm thick. About 60 cm N of sample 4-51. Appears less bioturbated than originally thought
PDA-4-53	<i>LSI-54</i>	E13	8	1001.77	1010.96	-6.73	-6.682	Just below sample IV -52. Cemented layer (calcite?) roughly equivalent to hard layer at base of -sample 4-51. Porous and very open work. Possible clay coatings. Some cm-sized limestone fragments tightly cemented
PDA-4-54	<i>MNJ-25</i>	Sq. E13	8	1001.81	1010.94	-6.784	-6.828	Just below sample 4-53 but distinct fine conglomerate layer. Very hard and porous
PDA-4-55	<i>MNK-29</i>	Sq. E13	6B	1000.24	1010.62	-6.165	-6.248	Well-cemented massive sand with abundant flint chips oriented at a variety of orientations. Some charcoal, bone splinters. Large block. Sediments less cemented away from the rock in this square
PDA-4-56	<i>MNJ-23</i>	G14	8	1002.65	1008.05	-7.1	-7.185	From basal 7 cm: bands and red and charcoal-rich sediment similar to that of sample -51
PDA-4-57	<i>LSI-55; LSI-56; LSI-57; LSI-58</i>	G14	8	1002.63	1008.15	-6.767	-7.093	32 cm-long section of partly cemented, cm-thick charcoal-rich bands, rubefied. Many bones, burnt flint. Many white spots with white porous material that resembles small worm tubes. Calcined bone. Dark areas (dusky red—2.5YR3/2), “greasy” organic sand. Quite damp. Possible rubefied aggregates (1–2 cm) or pieces of weathered bedrock

(continued)

Table 2.3 (continued)

Sample no.	Spectrum no.	Square	Layer	X	Y	Upper Z	Lower Z	Description
2002								
PDA-101	<i>NTO-012; NTO-001??</i>	E13	8	1001.7	1010.99	−6.838		Very hard, cemented angular pebbles/scree. Flint, burnt bone and some charcoal. Many pores and intergranular voids. Quite crystalline and fresh
PDA-104	<i>NTO-013; NTO-014; NTO-015</i>	D11	5A					Very loose mixture of burned bone, sand and stone next to large burrow sampled last year. Layer goes around to N wall where it is more compact and locally cemented. Overall, bones are quite large in this layer, which dips to SE according to lithics and bone plots; in Layer 3A, they tend to be horizontal
PDA-105	<i>NTO-016</i>	F11	5A	999.715	1009.98	−5.481		Massive to cemented strong brown, silty sand with bone and flint. Laterally with angular stone fragments. Many roots and some rhizoliths. Locally cemented (1 m back, the same layer is overlain by large angular blocks of roof fall.)
PDA-106	<i>NTO-017</i>	H18	5B	1006.36	1007.46	−5.75	5.794	Fine gravelly sand with sand-sized grains of quartz and limestone. Rounded and angular, decimeter-sized blocks of rock fall. Southernmost part on E wall here. Just above Bordes' wall. Some roots
PDA-107	<i>NTO-018; NTO-019</i>	D13	5B	1001.53	1011.53	−6.663		Moist pebbly sand, moderately concreted and rests above very cemented gravel unit. Some limestone but seems to be overall noncalcareous. Apparent clay films. Some bright red (heated?) rocks, burnt flakes. Definitely seems clayier than others. Generally horizontal and rests on concreted layer that slopes upward along the bedrock floor toward the back of the cave. Laterally equivalent to Layer 6 in central part of the cave to the S
PDA-108	<i>NTO-020; NTO-021</i>	C13	6B	1001.93	1012.04	−6.343	−6.435	Two lithologies: Basal—organic-rich, clayey (?) sand with many burned flints. Seems to rest on bedrock, some of which seems fire reddened. Overall seems noncalcareous. Bone fragments. Some rounded cm-sized limestone grains that appear weathered and decalcifying. Lighter, upper part is sandy and seems to slope up against the back wall
PDA-109	<i>NTO-022</i>	C13	6A	1001.64	1012.12	−6.107		Soft with abundant flint and bone fragments, mostly burned. No orientation or bedding, and artifacts are at different orientations (cryoturbation?)
PDA-110	<i>NTO-023</i>	E13	8	1001.54	1010.1	−6.877		Hard, calcite-cemented “breccia”, consisting of burnt bone fragments (1–2 cm), <5 cm above bedrock and likely cemented because of its position above bedrock. Overlain and surrounded by reddish sediment in this area

(continued)

Table 2.3 (continued)

Sample no.	Spectrum no.	Square	Layer	X	Y	Upper Z	Lower Z	Description
PDA-111	<i>NTO-024; NTO-025; NTO-026</i>	F13	8	1001.62	1009.96	-6.745	-6.905	Ca. 15 cm block that includes BF-1, BF-3 and possibly BF-5 at base. Difficult to observe in field because of moisture content and poor lighting, but overall consists of dark layer at top (BF-1; 0–6 cm) with abundant burnt bone and flint, over ~4–5 cm of lighter, reddish band in middle overlying darker unit at bottom with many burnt bones (BF-3). Sample does not include cemented unit at bottom, nor Layer 7
PDA-113	<i>NTO-028</i>	plateau						On plateau just N of site, ca. 25 m from where path reaches plateau, steep slope down to valley, just N of cave. Sample from base of tree throw: Clayey fine sand with locally clay coats around roots. Looks like Bt horizon
PDA-115	<i>NTO-029; NTO-030</i>	E13	8	1001.26	1010.55	-6.862	-6.763	Concretion with vertical tube-like hole in the center. Appears to have vughy, geode like crystals of calcite. Could represent old drip line or stal or water emanating from phreatic water trapped at bedrock sediment contact. Some of artifacts and bones nearby are vertical and limestone fragments have different angles of dip. Only ca. 50 cm from cemented gravel in Sq. E13
PDA-116	<i>NTO-031</i>	F11	5A	999.717	1009.26	-5.61		Loose to compact, chaotic mixture of sand, flint and bone. Sand seems to vary from well sorted fine quartz to poorly sorted quartz and calcite sand. Pebbles are angular, flat to rounded and equant. Should be similar to sample -33 from D11 but is from different layer ~20 cm lower
PDA-117	<i>NTO-032</i>	D12	7	1000.71	1011.81	-6.476		Cemented sand with moderate porosity and zones of washed sand. Also looks like clay coatings locally. Seems to be above large roof fall above Layer 7
PDA-118	<i>NTO-033</i>	E11	5B	999.593	1010.74	-5.966		Rounded limestone gravel with cemented sandy matrix. Perhaps some pendants on stones
PDA-119	<i>NTO-001</i>	E11	5B	999.825	1010.44	-5.954		Similar to sample -118 but more matrix. Sand, mostly noncalcified, with clay and iron concentrations. Curious that both fresh artifacts and rounded, worn chunky types of flints occur together. Many pebbles seem to exhibit Mn staining on them (possibly inherited)
PDA-120	<i>NTO-035; NTO-036; NTO-042</i>	D11	5B	999.769	1011.93	-5.822	-5.996	Moist, soft, massive sand with scattered rock fragments and very abundant bone and flint at top of the layer; this is true elsewhere as well. Artifacts are fresh and angular. Layer 5B with rounded limestone [also 1 flat basalt pebble]. Lower part in Layer 6 should be roughly equivalent to PDA4-8 and is slightly above PDA4-55

(continued)

Table 2.3 (continued)

Sample no.	Spectrum no.	Square	Layer	X	Y	Upper Z	Lower Z	Description
PDA-121	<i>NTO-037</i>	D12	7	1000.07	1011.43	−6.592		Lower part: Layer 7 consists of fine, angular gravel composed of quartz, limestone, and rolled flint. Quite porous, with mostly packing voids between clasts; fines look winnowed. Cemented with microspar as in Layer 8 and sample rests on bedrock. Some secondary clays in voids. Upper part: Layer 6 is composed of poorly sorted, partly calcareous sand
PDA-122	<i>NTO-038</i>	H13	5B	1001.3	1007.39	−5.994		Cemented clayey sand with rhizoliths
PDA-123	<i>NTO-039</i>	H13	5B	1001.28	1007.28	−5.495		Similar to -122 but somewhat more cemented. Finer rhizoliths and no stones
PDA-124	<i>NTO-040</i>	H11	4C	999.843	1007.86	−5.387		Cemented clayey sand with some roots and possibly fine rhizoliths. Looks like cemented area situated below former drip
PDA-125	<i>NTO-041</i>	C16	8	1004.65	1012.19	−6.212	−6.293	Sample has 2 parts. Lower is composed of silty sand with small domains of silt mixed with fine organic matter; possible siltans within fissures. Some limestone granules; crumbly and looks bioturbated with possible worm casts or insect burrows. Lower part, ~7 cm thick, rests on bedrock and seems to pinch out in Sq. 17. Locally cemented; modern roots. Upper part: only a small part of which is preserved here and most in sample 125 bis. Sits on the lower part with a sharp contact. Compact organic-rich silty sand with many burn bones and flints. Fairly massive but weakly bedded. Very similar to the base of Layer 8
2003								
PDA-4-201	<i>OYF-001</i>	D12	6B	999.979	1011.51	−6.165	−6.29	Massive clayey sand, with angular chips of burnt bone, 1–2 cm in diameter; likely anthropogenic. Abuts against roof fall in E12. Fairly horizontal bedding, and with slight dip
PDA-4-202	<i>OYF-002; 003</i>	DE12	6B	999.973	1011.02	−6.218	−6.293	Laterally equivalent to -201
PDA-4-203	<i>OYF-004</i>	F14	7	1002.54	1008.97	−6.742	6.815	Washed sand with well-rounded, edge-damaged flint artifacts. Some limestone chips are fresh and angular
PDA-4-204	<i>OYF-005</i>	F14	7	1002.05	1009.13	−6.75		Seems washed. With large weathered limestone block and marbled lighter and darker matrix. Partly cemented although friable. Variable thickness. Bedrock, locally rotten
PDA-4-205	<i>OYF-006</i>	G13	7, 8	1001.81	1008.81		−6.799	Cemented sandy silt. Looks washed as in sample −204. Thin tubes of calcite (hypocoatings) but could be in process of dissolving. Not many angular stones
PDA-4-206	<i>OYF-007</i>	F14	7, 8	1002.47	1009.08	−6.724	−6.839	Upper part cemented with some angular stones

(continued)

Table 2.3 (continued)

Sample no.	Spectrum no.	Square	Layer	X	Y	Upper Z	Lower Z	Description
PDA-4-207	<i>OYF-008</i>	F14	8BB1, 8BB2	1002.56	1009.08	−6.796	−6.83	Top is 1–2 cm-thick cemented ash overlying soft dark reddish brown charcoal/organic matter-rich sand. Bones are black and likely burned; some calcined
PDA-4-209	<i>OYF-009; -010</i>	E11	8	999.78	1010.27	−6.759	−6.884	At base is “nougat-like” zone of reddish sand with cm-sized pebbles of white and reddish limestone. Some charcoal. This nougat climbs up along bedrock and is about 2–3 cm thick. Sample is about 11 cm thick. Bottom 5 cm has splotches of washed sand and overall are quite sandy. Not cemented but quite compact
PDA-4-210	<i>OZV-001; -002</i>	F11	8	999.779	1009.52	−6.817	−6.98	Sublayers of charcoal and rubefaction. Bedrock stained red just under sample. Washed at base
PDA-4-213	<i>OYF-011</i>	J14	8	1002.69	1005.07	−7.181	−7.29	On west side of cave entrance, from more sterile part of Layer 8, just above bedrock. Lower part sand, locally cemented and with some carbonate hypocoatings. Lower part of sample could be part of weathered bedrock. Flint and bone chips; some brown (organic matter?) dusty matrix. Abundant cultural material. Sand could be washed
PDA-4-215	<i>OYF-012; -013; -014</i>	F12	8	1000.95	1009.39	−6.775	−6.995	Layers 8AA1, 8BB1 and 8BB2; 8CC (orange layer) and 8DD. Sample also cracked in the upper 1/3, along 8CC/8DD, but probably all right. Upper part richer in bones and lithics. Lowermost part of 8CC is washed. Middle part has ghosts of limestone
PDA-4-216	<i>OYF-015; -016; -017</i>	F12	8	1000.05	1009.34	−6.797	−6.997	Upper part is mostly charcoal rich. Layer 8AA is thin veneer at top (ca. 1–2 cm); darker 8BB (~8 cm thick); redder 8CC (~5–6 cm thick) on top of darker 8DD (~2–3 cm thick). NO Layer 8EE here. Sample broke in the middle and lowermost part is disturbed. Loose samples of 8BB [dark reddish brown; 5YR3/3] and 8CC [reddish brown; 5YR4/4]. Red layer consists of poorly sorted washed sand but with burnt bone and decayed limestone. Darker 8BB is also washed sand and some carbonate hypocoatings. To west (F11) this massive dark layer spits into 3 distinct dark zones. Here, red staining on floor also increases

square I13 it grades into sand. The contact between Layers 7 and 8 is distinct and undulates slightly (Figs. 2.5a and 2.9e). In the northern portion of the site, Layer 7 directly overlies bedrock, whereas in the southern portion it is present intermittently as patches between blocks of roof fall (Figs. 2.6 and 2.9a, b). It is generally about 5 cm thick, but

in certain areas (e.g., square G14) it reaches up to 10 cm where it has been forced up between two pieces of roof fall (Figs. 2.5d and 2.7e). The upper surface of Layer 7 dips to the west and southwest pointing to erosion and/or compression of the large blocks that fell in the early stages of Layer 6B time.

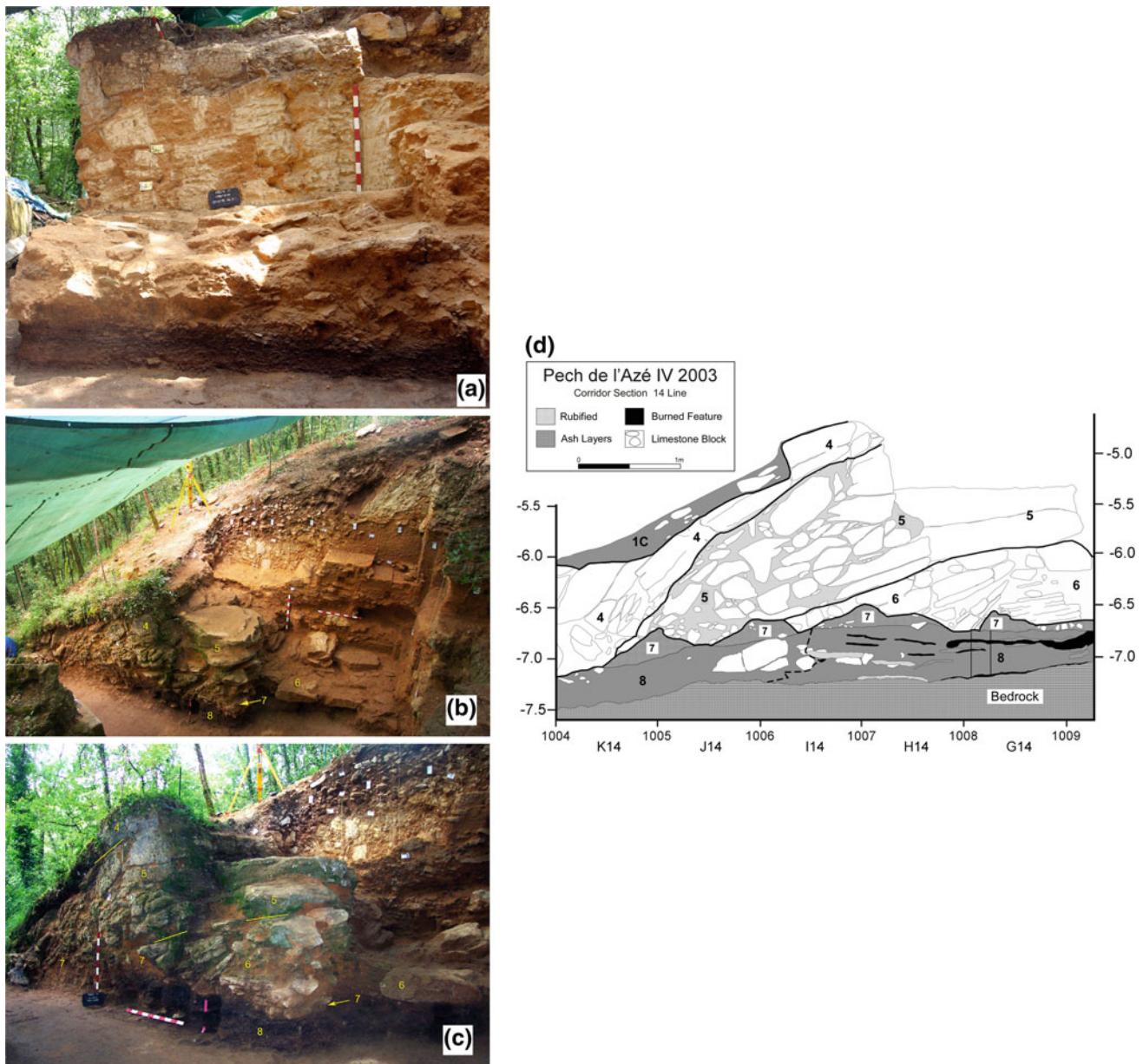


Fig. 2.5 **a** South section at end of 2002 season from bedrock at the base up to Layers 4 and 1 at the very top. Note that Layer 8 thins from *left* to *right* (east to west). Note the thin band of Layer 7 above it, and the sandy infillings between the blocks of Layers 5 and 6. The bench in the foreground is situated mostly in squares G12-14. **b** View of western half of the site in the 2001 season, showing partially excavated Western and Southern sections. Note the flat-lying limestone slabs in the center of Layer 6 that signals the initial collapse of the cave roof from within the confines of the cave; later, the brow retreated northward beginning with the accumulation of the large blocks in Layer 4. **c** View of southern area of the site in the 2001 season, showing the entrance

corridor and imbricated roof collapse spanning Layers 6, 5, and 4. **d** Section along west side of the corridor leading into the site (see Fig. 2.2), showing Layers 8 through 4. Note the imbrication of the large slabs of collapsed bedrock roof fall and patches of Layer 7. The two vertical lines in Layer 8 in square G14 indicate the limits of sample 51. Note that Layer 8 tends to be thickest in squares H and I 14, and thins away from this: in square I14, dark organic sands grade into lighter colored sand to the *left* (south) as shown by the *dashed line*. As the blocks of roof fall overlie Layer 8, it is clear that the burning activities were situated just inside cave from the brow

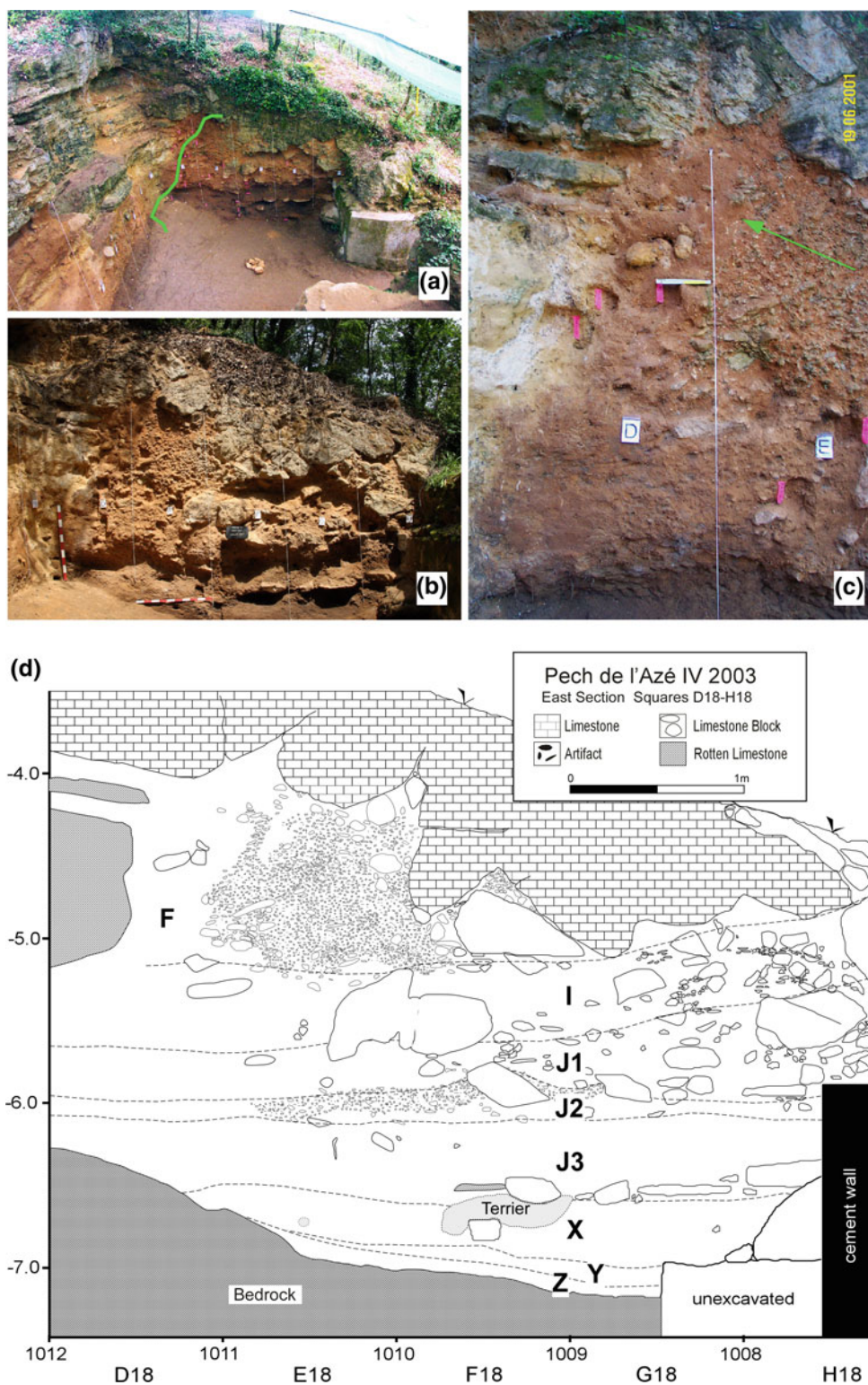
Layer 6 (≡Bordes' Levels J3, J3a, J3b, and J3c).

As with many units, Layer 6 is laterally variable from north to south, being generally sandy in the north (e.g., D-E lines), but becoming stonier to the south. In addition, the lower part is characterized by large (>1 m sized) blocks of roof fall that

rest on Layer 7 (Figs. 2.3, 2.4 and 2.5a). Because of these latter differences, the layer was subdivided into two subunits, Layers 6A and 6B.

The basal part of Layer 6 (6B) is characterized by large, flat-lying blocks of limestone roof fall that are in direct

Fig. 2.6 **a** Photograph of East section at end of 2002 season. Note how the bedrock wall on the north (*left*) side of the photo extends to the south and that the roof of the collapsed cave is more evident here in contrast to the West section, which is less close to the north wall, and nearer to the interior of the concealed entrance to the main cave. **b** East section at end of the 2003 season. Note the thickness of the rock fall at top that represents collapse of the roof that here is considerably more intact than on the West section. **c** Detail of East Section at the contact between the weathered bedrock wall at left (north) and the sedimentary fill. The arrow points to a zone of decalcified bedrock, characterized by quartz sand, some heavy minerals, and extensive red iron-rich dusty clay coatings. **d** Drawing of East Profile shown in 6B. Note that it was not possible to achieve the stratigraphic definition of the units as was the case for the West Section, so layer attributions are approximate



contact with the upper surface of Layer 7 (see Figs. 2.3c and 2.4). These blocks tend to be tabular, about 20–30 cm in average thickness, and reach up to 120 cm in length, although the larger block sizes are concentrated in the western portion of the site (squares D–E–F/12–13).

Although most tend to be flat lying, many are on edge and are imbedded in the layer obliquely (Figs. 2.3, 2.4 and 2.5). Remains of some of the slabs can be still seen on the witness section of the north wall. Layer 6B also contains smaller limestone blocks, cobbles, and gravel, as well as

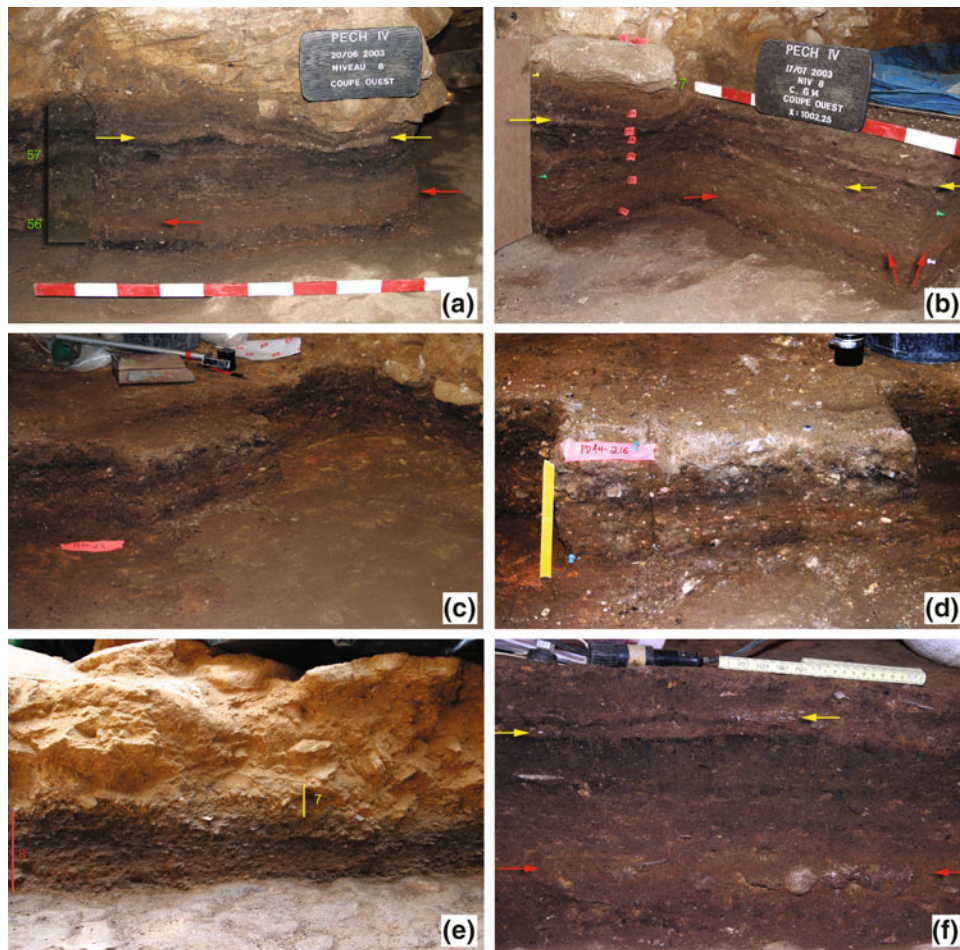


Fig. 2.7 **a** Layer 8 looking west along the entrance trench in square J14. The *red arrows* point to reddened zones thought by Bordes to represent burning associated with hearths; rather they are apparently diagenetically formed. The *yellow arrows* indicate layers of intact calcareous ashes that overlie organic-rich zones and together represent intact hearths. Elsewhere, the dark bands are more diffuse and a result of hearth rake out and spreading out of previously combusted materials. Samples 56 and 57 come from the column in the *left hand* part of the photo. **b** Another view of Layer 8 looking southwest in sq. G14. *Yellow arrows* are ash layers whereas *red* ones point to reddish bands previously thought to be produced by heating. Layer 7 is the thin pale

yellow deformed zone just underlying the piece of roof fall at the left. **c** Sample 216 from Layer 8. Note the red staining of the bedrock floor to the right. **d** Detail of sample 216 from Layer 8, showing the overall homogeneity of the deposits other than the diffuse black band at the *top*. Note the red staining on the bedrock floor and the *reddish band* in the *middle* of the photograph that stains limestone clasts. Sample 215 was removed just to the left of 216. Scale bar is 18 cm. **e** South face of Sq. F14 showing Layer 8 (*red line* is 20 cm thick), overlain by irregular cryoturbated lenses of worn flints and stones of Layer 7. **f** Layer 8, South section. Note the diffuse darker band ~10 cm below the surface, which represents hearth rake out

anthropogenic components (bone; especially in the East Section). In addition, the finer fraction is comprised of massive, soft silty sand with granule- to cm-sized clasts of limestone (Figs. 2.13, 2.14 and 2.15).

The upper part of Layer 6 (6A) differs overall from 6B in that it contains many fewer large blocks, although some tilted tabular blocks of roof fall still occur in squares E11 and E12. Otherwise, the sublayer consists of soft, yellowish red to strong brown (5YR to 7.5YR 5/6) massive sand with granule-sized limestone inclusions (Fig. 2.13). Some of the flint artifacts are vertically oriented (likely due to cryoturbation, or frost/soil creep—see below).

On the East Section, Layers 6A and 6B are less differentiated (Fig. 2.7), although the lower part (Layer 6B) also exhibits tabular slabs of bedrock; these clasts tend to be smaller than those on the West Section. In addition, the finer fraction of Layer 6 on the East Section appears to be more organic rich, and slightly darker brown (7.5YR4/4; dark yellowish brown), with possibly greater abundances of flint and bone. This latter observation suggests that burning activity took place on the eastern part of the site as well, extending further east beyond the East Section.

Layer 6 continues south of square F where in square G and H, the distinction between Layers 6A and 6B becomes

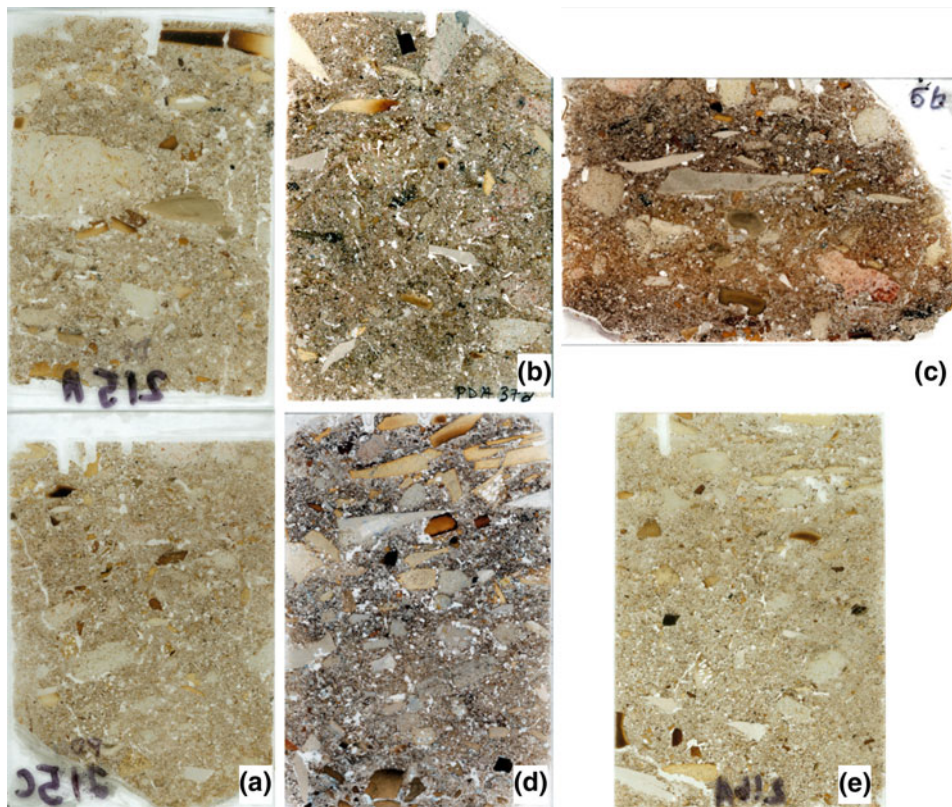


Fig. 2.8 **a** Sample 215 (Layer 8; Sq. F12) scans of thin sections from upper (215A) and lower (215C) parts of the impregnated block. Note the distribution of brown burned bones, including a broken (trampled) one at the top of 215A. All thin sections are 50×75 mm and are in plane-polarized light (PPL) unless noted otherwise. **b** Sample 37A (Layer 8; Sq. D18), Layer 8, macro scan showing dense matrix containing a mixture of burnt bones, char (diffuse black domains), and angular chert clasts. **c** Sample 56 (Layer 8; Sq. G14), base of Layer 8.

Visible here is red staining of the matrix (including limestone clast in the lower right of the sample). **d** Sample 57B (Layer 8; Sq. G14), from above sample 56 in Layer 8. Visible here are burned and trampled bones at the top, overlying a darker layer containing char. **e** Sample 216A (Layer 8; Sq. F12). This sample comes from the outer extent of Layer 8, which is evident by the overall light color and lower quantity of bone

somewhat less clear due to the appearance of large tabular blocks as in squares D–E–F (Fig. 2.4a). In this southern part, the finer, sandy sediments of 6A contain large tabular blocks of roof fall that are similar to those in squares D–E–F, indicating that Layer 6 represents a major period of roof fall accumulation. We note, however, that the first phase of this collapse was initially centered in squares D–E–F and with time successively migrated southward as shown for Layers 5 and 4 (Figs. 2.3 and 2.5d).

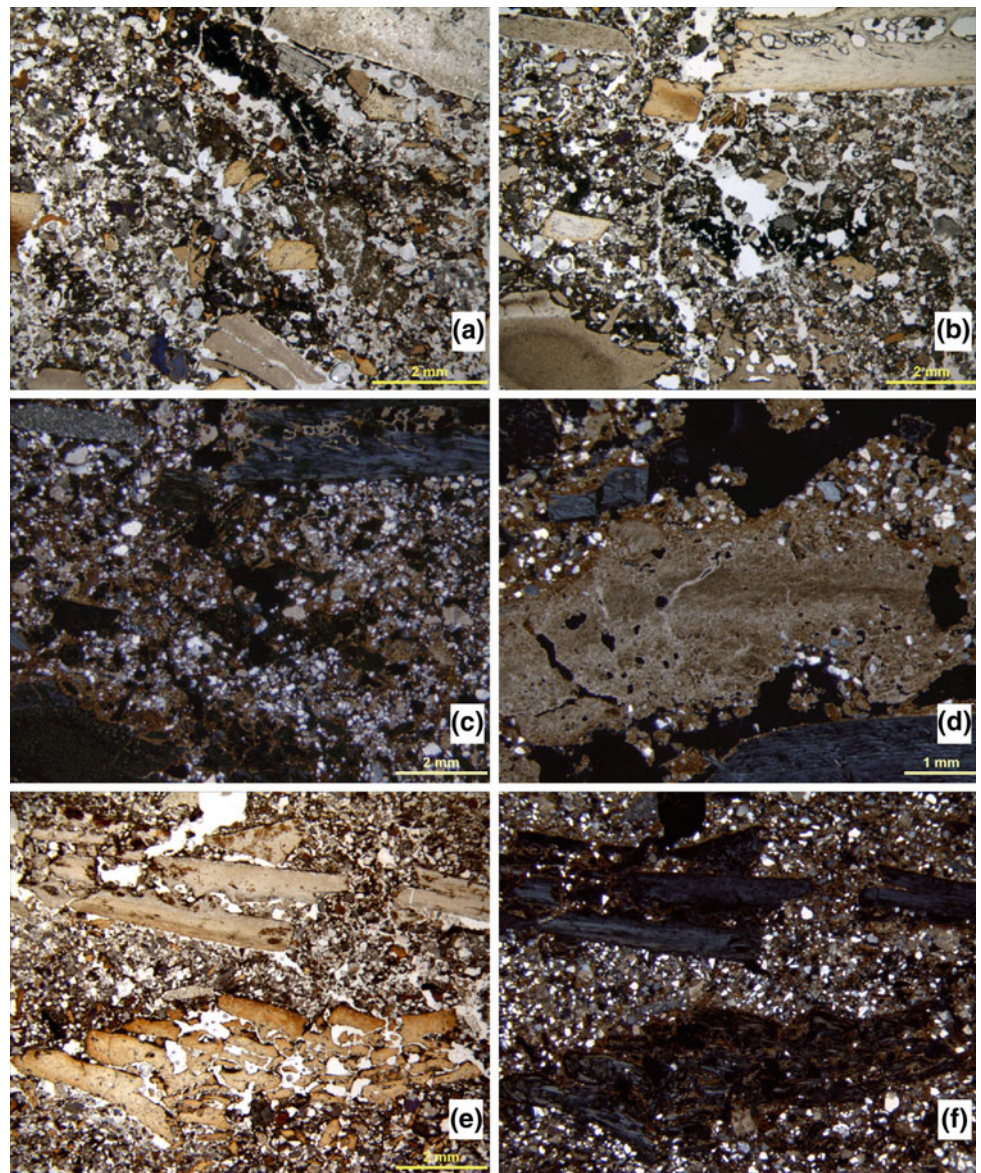
Layers 5A and 5B (Roughly \equiv Bordes' Levels J1, J2, and J3)

This stony sandy complex does not correspond directly to Bordes' terminology, and we have regrouped some of his layers into our Layers 5A and 5B. Layer 5 rests on Layer 6A with a sharp and irregular contact (Figs. 2.3b and 2.4). Moreover, the contact between Layer 5B and the underlying 6A is generally inclined to the west and southwest. In square G11, however, Layer 5B appears to climb up over a large

block of roof fall in squares G and H 11 (Fig. 2.4a). Moreover, Layer 5B thickens to the south and southwest, being about 15 cm thick in square C12, and thickening to about 40 cm in square G12. Bordes' somewhat schematic section drawing (see below) shows slight thickening of his Layer J₂ although it is overall thinner than our Layer 5B.

Layer 5B consists of numerous—typically rounded lithoclasts within a yellowish red (5YR5/8) silty sandy matrix (Figs. 2.16 and 2.17). Interestingly, some of the cm-sized limestone clasts are both well rounded and very fresh (Figs. 2.16 and 2.17), and have equant shapes that become more platy and angular from square E11 into D11 and C12—i.e., in the direction of the cave wall. Some of the ~ 4 –5 cm diameter clasts are very smooth and rounded and originally interpreted as evidence only of cryoturbation (similar clasts can be seen in Pech II (Bordes 1972; Goldberg 1979); they may also be derived from older sediments within the now-concealed cave interior and represent relicts of the former phreatic system (Braillard 2000).

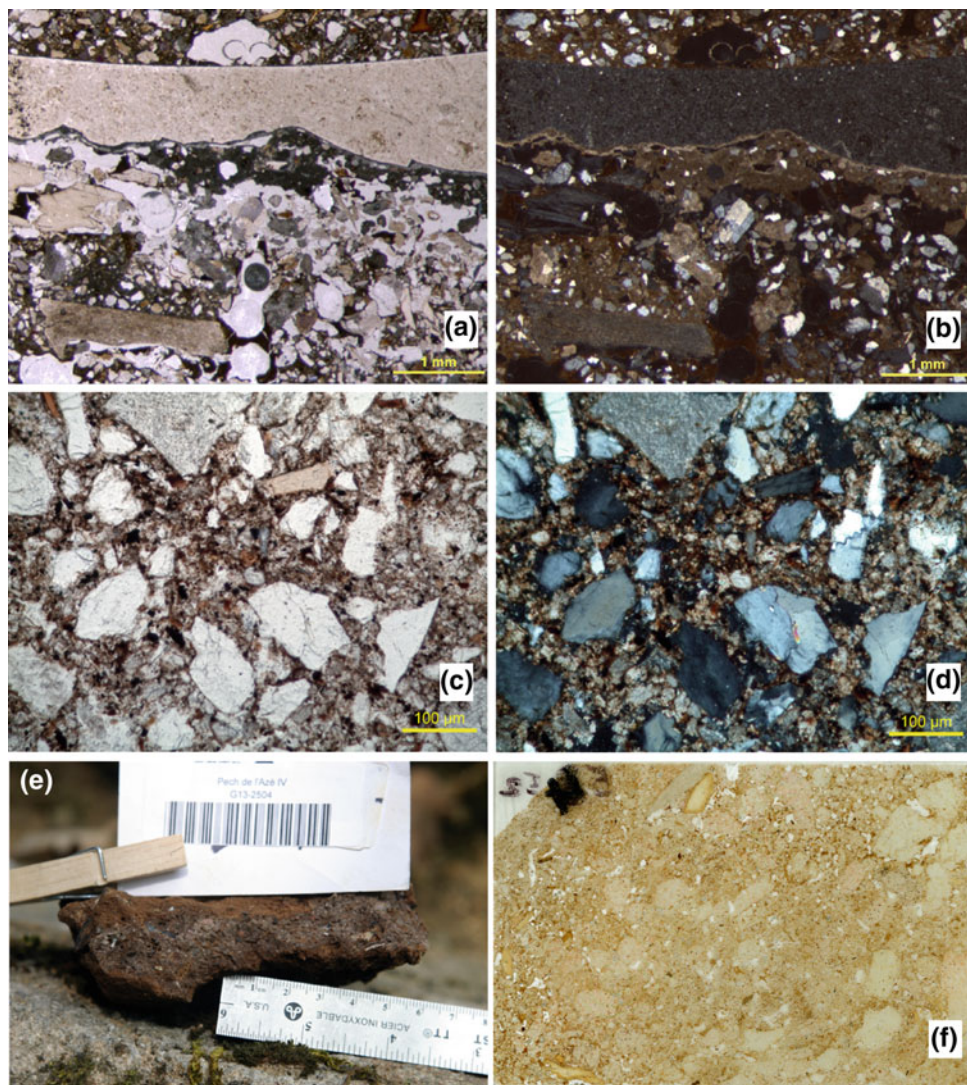
Fig. 2.9 **a** Sample 51A (Layer 8; Sq. E13). Photomicrograph showing burned and calcined bone and darker areas of char. Plane-polarized light (PPL). **b** Sample 51B, (Layer 8; Sq. E13). Burned and calcined bone with zone of black char in the middle. PPL. **c** Sample 51B (Layer 8; Sq. E13). Same as b but in XPL. Note some reddish iron-rich dusty clay coatings in the irregular voids. **d** Sample 51A (Layer 8; Sq. E13). Layer of cemented, fractured, and bedded calcareous ashes from the top of thin section 51. Cross-polarized light (XPL). **e** Sample 52 (Layer 8; Sq. E13), Layer 8. Trampled and crushed bone with “scissor” fractures. PPL. **f** Sample 52. Same as in e but in XPL. Note the red, iron-rich coatings around the bones



Layer 5A is somewhat similar to Layer 5B but is characterized by flatter, well-bedded limestone clasts in a sandy matrix, and contains numerous generally angular decimeter-sized blocks of limestone roof fall. These are scattered throughout the layer, as well as in the East Section where larger blocks (20–40 cm across) occur at this stratigraphic level. Layer 5A thins slightly from north to south (Figs. 2.3b, c and 2.4). In thin section, both bones and lithics were relatively common (Figs. 2.16, 2.17 and 2.18), and many of the former are burned, some calcined (Fig. 2.18). In addition, in many samples (e.g., sample 32B from Layer 6A; Fig. 2.15b), remains of calcareous roots are present, indicative of plants growing on the surface beneath the dripline; as discussed below they appear to demarcate

former positions of the dripline as it retreated (Figs. 2.3b and 2.4a). In thin section (Fig. 2.16b) a diffuse band of burned bones ~1 cm in diameter can be observed in Layer 5A; interestingly no combustion features were noted. Finally, sediments closer to the rear wall of the cave (e.g., sample 29; square D11) exhibit reddish grain coatings of iron-rich dusty clay (Fig. 2.18d, e). Such coatings appear to be penecontemporaneous with the calcification of roots, because in thin section, the iron/clay can be seen to impregnate some of the calcified roots but, in turn, they are pierced by fresher, unstained calcareous roots (Fig. 2.18a). In general, however, for most of the sediments observed in thin section, calcification of roots and coeval formation of hypocoatings appear to be the last post-depositional events, and for the most part,

Fig. 2.10 **a** Sample 56 (Layer 8; Sq. G14), Layer 8. A large flint flake at top rests on cemented ash-rich bed. PPL. **b** Same as in **a** but in XPL. **c** Sample 215C (Layer 8; Sq. F12) from cemented lower part of the sample in Layer 8. Note the compact nature of the sediment, with coarser quartz and chert grains in a finer matrix composed of dusty fine calcareous sand and silt. PPL. **d** Sample 215C. Same as in **c** but in XPL. **e** Hand sample from square G13 of well-indurated, microsparite-cemented sediment from the base of Layer 8 that rests directly on bedrock. Cementation here appears to have been fostered by the collection of water at the sediment–bedrock interface (see also Fig. 2.11c–f). **f** Thin section scan of sample 54 (Layer 8; Sq. E13) from the base of Layer 8 in contact with the bedrock. Note the rounded cm-sized limestone grains, a few yellow bones, and the numerous vesicles and channels that perforate a compact matrix. Width is 46 mm



postdate the iron/clay coatings; some calcification could be of relatively recent age.

The lateral continuation of Layers 5A and 5B south of the G line is not very clear. However, pockets of sandy material containing well-rounded cm-sized limestone clasts are found in spaces between large blocks of fallen roof (Fig. 2.5a). These “pocket-fills” occur at elevations comparable to those where Layers 5A and 5B occur in squares D, E, and F (Fig. 2.3b, c).

The occurrence of the finer sediments between the individual limestone blocks indicates that these blocks fell prior to or are penecontemporaneous with this finer material. As in the case of Layer 6, we note that the blocks are inclined southward (Figs. 2.3c and 2.5) so that successively younger blocks are found further to the south. They do not represent one roof fall event, but rather a series of small collapse episodes. Furthermore, this imbrication denotes that the roof fall “peeled off” first from the *underside* of the roof within

the cave environment. In any case, the blocks do *not* represent a total collapse or retreat of the cave brow from the outward edge toward the cliff face.

The lithologies of Layers 5A and 5B on the East Section (Figs. 2.6 and 2.7) are not as striking as those on the West Section, and correlations between them essentially follow Bordes’ designations; we did not excavate this side of the site. In the East Section, Layer 5B appears to be represented by poorly sorted sandy gravel, consisting of rounded and spherical limestone gravel 1 cm in diameter, and ca. 2 cm subangular to sub-rounded gravel in a reddish yellow sandy matrix. The sediments become increasingly finer grained and redder toward the North wall (Fig. 2.6), mirroring the same phenomenon seen on the West Section. In any case, it is clear that the sediments of what appear to be Layer 5 in the East Section are eroded into the underlying softer sand, as is the case for the Layer 5/6 contact on the West Section.

Fig. 2.11 **a** Sample 54 (Layer 8; Sq. E13) showing angular bone fragments in a compact, calcite-cemented matrix. PPL. **b** Sample 54, XPL view of **a** at left with surrounding micritic cement. **c** Sample 54, showing two large voids with iron/clay coatings with subsequent phase of acicular (needles) calcite. Note the compactness of the cemented matrix. **d** Similar view as in **c** but in XPL. **e** Detailed view of **c** and **d** showing Fe/clay coating and acicular calcite. **f** Detailed view of **e** highlighting the acicular microsparite crystals lining the void. XPL

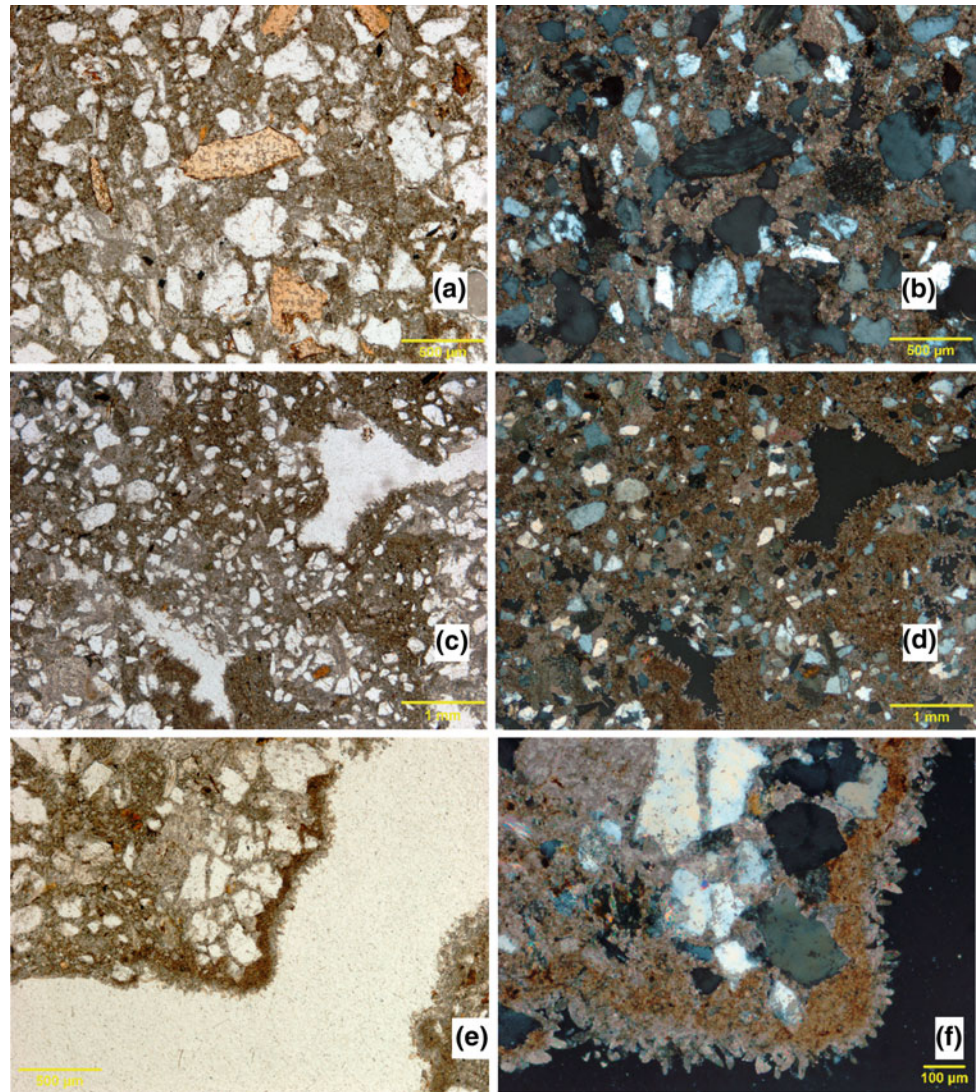
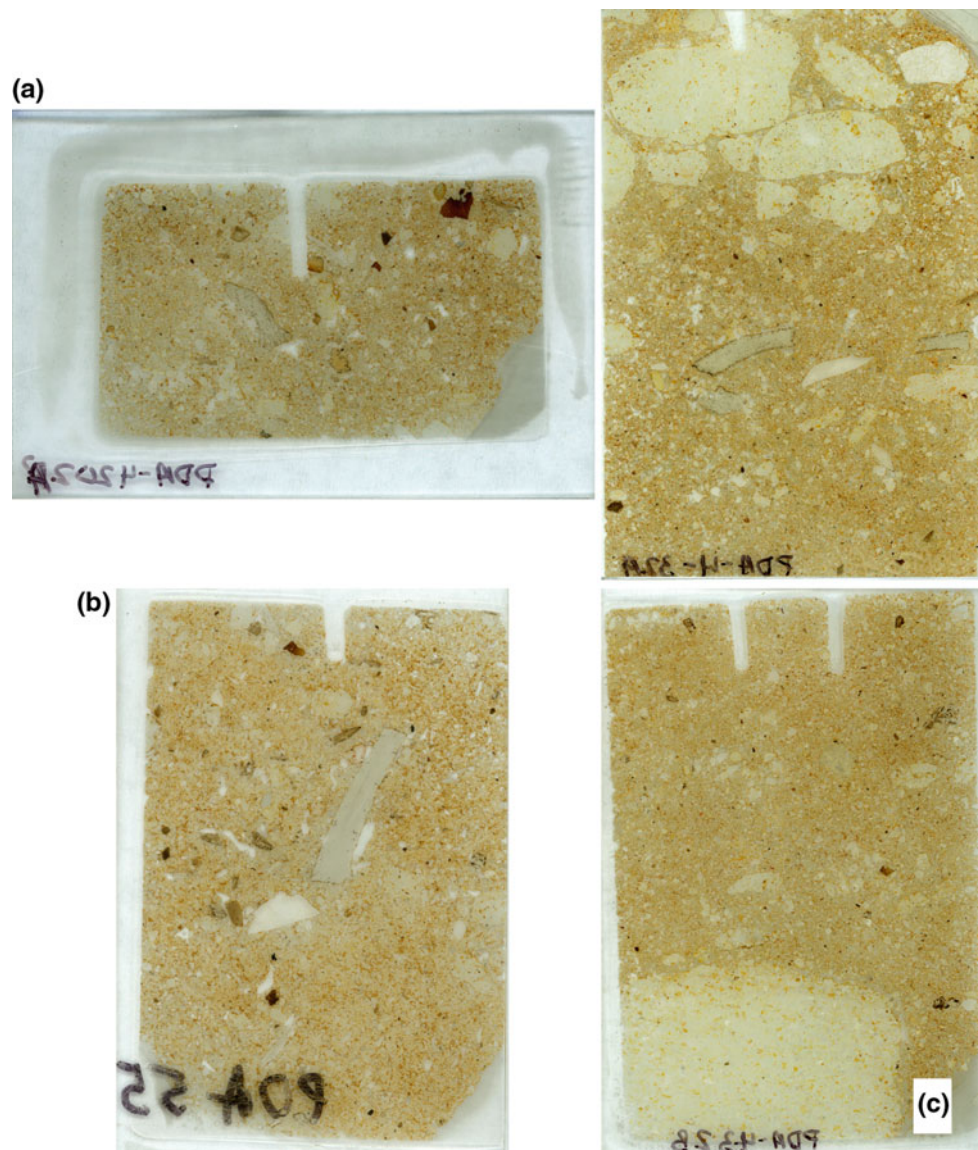


Fig. 2.12 Rounded, cryoturbated pebbles from Layer 7



Fig. 2.13 **a** Scan of sample 202A (Layer 6B; Sq. D/E 12) showing fine limestone sand and granules, with a piece of burned bone at the *top*. **b** Scan of sample 55 (Layer 6B; Sq. E13)—burned bone fragments (*brown specks*) and unburned bones in sandy matrix with iron-rich clay between grains. **c** Scans of samples 32A and 32B (Layer 6A; Sq. F11). Generally similar to sample 55 above but note the rounded limestone clasts and layer of angular bone and chert fragments in sample 32A



Layers 4A, 4B, and 4C (\equiv Bordes' Levels G, H₁, H₂, I₁, and I₂)

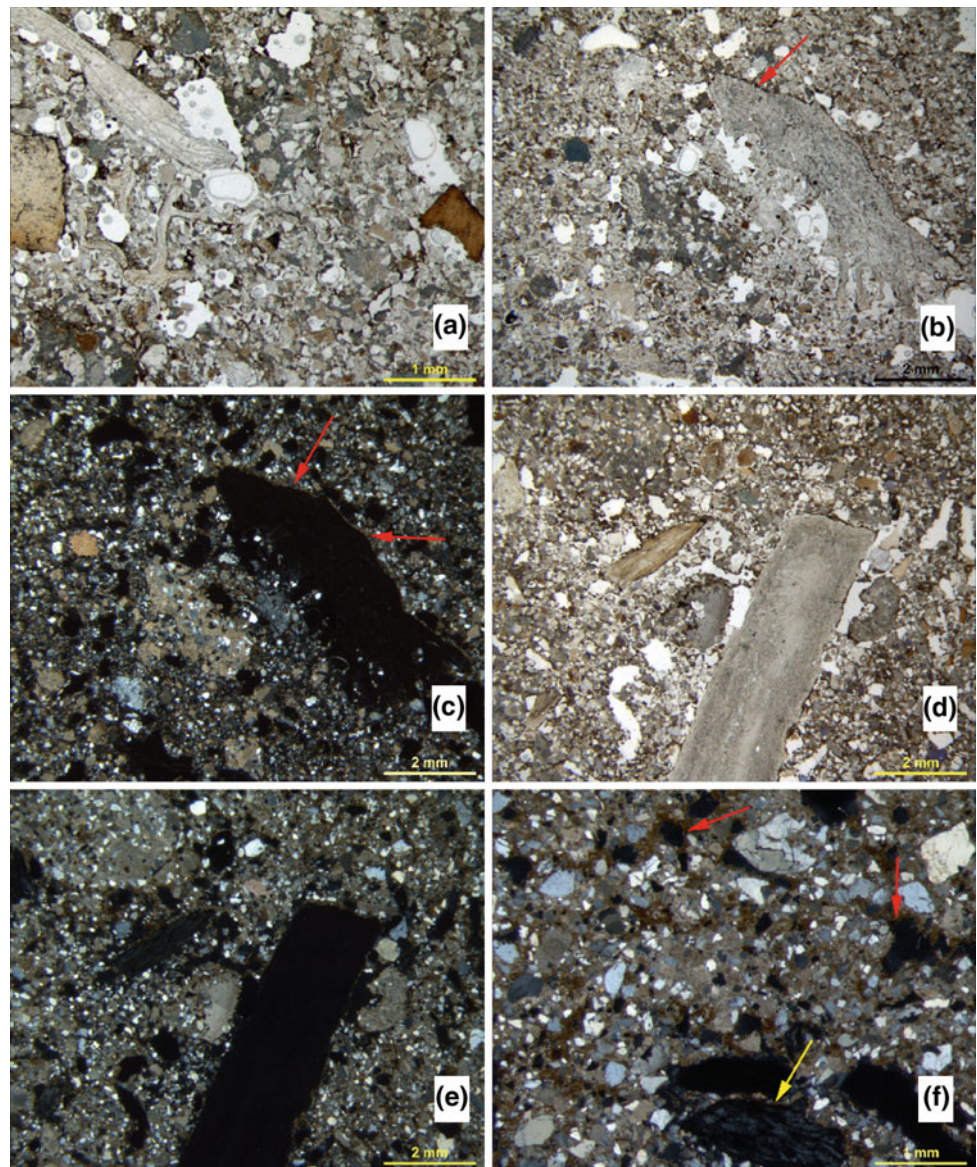
This relatively thick (95–130 cm) stratigraphic unit is set off from both the overlying and underlying angular gravelly deposits by being not only generally fine grained but also by containing numerous blocks of roof fall whose abundance increases to the south; the contact with the underlying Layer 5A is sharp and erosional (Figs. 2.3 and 2.4). Layer 4 is subdivided into Layers 4C, 4B, and 4A (from bottom to top), with roof blocks being more common in Layer 4B. Stratigraphic subdivisions are clearest closer to the bedrock walls, as in square D11, and progressively to the south, there is a greater proportion of blocks of roof fall.

The shape of the roof fall is variable, as for example in squares D11, E11, and F11, where they range from tabular

blocks to subangular, flattish pieces. Similar shapes are reflected in the smaller (e.g., cm-sized) clasts as seen in thin section (Figs. 2.19, 2.20, 2.21, 2.22 and 2.23). In any case, the lowermost occurrence of these blocks is in Layer 4C but they dramatically and progressively increase in Layer 4B, where concentrations of gelifracsts were at the base of Layer 4B in square E11. Layer 4A also contains some roof fall but in general is finer grained, with cm-sized angular fragments of limestone in a sandy matrix (Figs. 2.19c, d, 2.20b and 2.23).

Layer 4 and its subdivisions are locally cemented (Figs. 2.3b–c and 2.4a), and Layer 4A is more calcareous in square E11 than in square D11, where it is sandier and markedly less calcareous. Interestingly, in squares F11 and G11, much of both Layers 4A and 4B is secondarily

Fig. 2.14 **a** Sample 202A (Layer 6B; Sq. D/E 12) showing yellow brown burned bones and pale yellow bone fragments in a quartzitic and calcareous sand matrix. PPL. **b** Sample 202A (Layer 6B; Sq. D/E 12) with quartzitic and calcareous sand matrix and thin calcareous silty clay coating (*arrow*) on chert grain. PPL. **c** Sample 202 A: same as **b** but in XPL. Note the relative paucity of fresh carbonate grains and relative high amounts quartz grains reflecting dissolution of the carbonate in place. This sample is close to the walls (Sq. D12) where carbonate dissolution is common. **d** Sample 55 (Layer 6B; Sq. E13). Burned bone fragments with reddish iron-rich dusty clay coatings around them PPL. **e** Sample 55 from Layer 6B, same as in **d** but in XPL. Note the presence of fresh calcareous sand and granules, which contrasts with sample 202A that is from square D12, close to the wall; this sample from square E13 is farther from the wall. **f** Detail of sample 55 illustrating its fresh calcitic nature, as well as brown, iron-rich dusty clay coatings around voids (*red arrows*) and coating grains, such as the bone fragment at the base of the photo (*yellow arrow*)



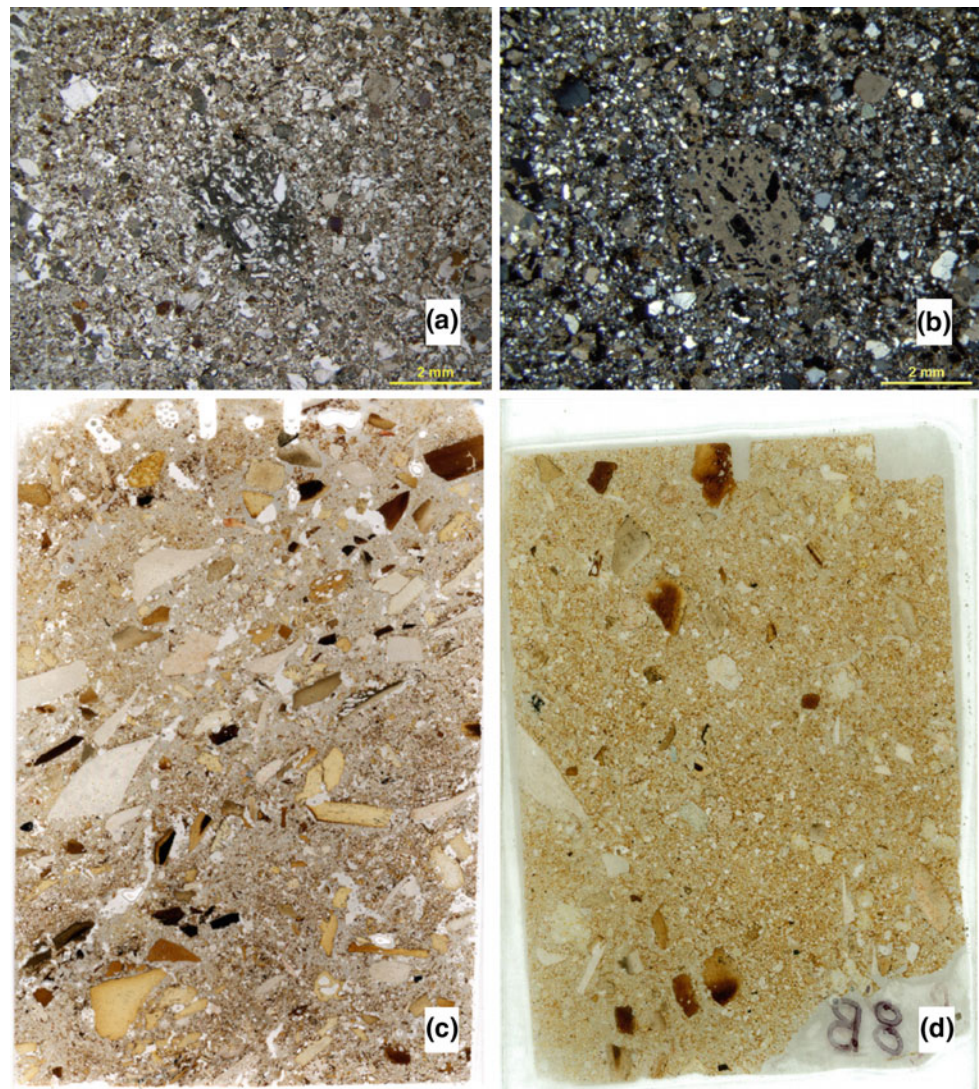
cemented as shown by interstitial micritic cements and calcified rootlets and hypocoatings (Figs. 2.21c, 2.22e–f and 2.23a, b); as mentioned above, the latter are a result of water dripping from the former brow of the cave. As is true for many of the sediments at Pech IV, iron-rich dusty clay coatings occur, and they are more abundant and pronounced near the back wall of the excavations (particularly squares C and D; Figs. 2.22c and 2.23b–d) and less so in square F for example (e.g., Fig. 2.21f).

The lateral stratigraphic correlation of Layer 4 with the large blocks occurring south of square H11 is not clear, owing to the erosional channel associated with the deposition of historic (Medieval?) deposits of Layers 1A/B/C (Figs. 2.3b and 2.4a). It appears, however, that by the time of deposition of Layer 4B, the bulk of the large blocks of roof fall (in squares I/J/K; Figs. 2.5 and 2.6) had already

fallen. The roof at the time of accumulation of Layer 4B was probably situated somewhere near squares G and H (Fig. 2.3b). Thus by this time, the cave was considerably more open. Support for this inference comes from the lithology of Layer 4A, which reveals some large pieces of rock fall in squares G and H; immediately below these blocks, Layer 4B sediments are very well indurated (Figs. 2.3b and 2.4a). On the East Section, the stratigraphic correlation of Layer 4 is also not well defined, particularly for the upper part, which contains mostly large blocks of roof slump, as the cave roof was more intact at this time (Figs. 2.7 and 2.8).

The average thickness of Layer 4C is about 20–30 cm and possibly thins to 20 cm towards the south. Layer 4B is about 30–40 cm thick, although the contact with Layer 4A is limited and not very clear in squares F/G/H. Layer 4A is

Fig. 2.15 **a** Sample 32B (Layer 6A; Sq. F11), consisting of quartz sand and some sand-sized limestone grains. PPL. **b** Same as **a**, but in XPL. The porous area in the center is fine calcified root fillings associated with vegetation growing on the former surface at the time. **c** Scan of sample 4B (Layer 6B; Sq. E19) showing bedded bones (mostly burnt) and lithics, with a finer, sandier matrix in the upper half of the slide. **d** Scan of sample 8B from Layer 6B (Sq. D13) showing the scatter of burnt bones, although the matrix is yellow brown and not rich in organic matter



about 45–60 cm thick, but its upper part is truncated in squares G and H by the Layer 1 complex.

Layers 3A and 3B (≡Bordes' Levels F₁ to F₄)

Layer 3, which is volumetrically much less widespread than the other layers, occurs mostly in squares D, E, and F. It is lithologically quite distinct from the Layer 4 complex, being more compact and cemented than Layer 4 and containing fewer limestone fragments (Figs. 2.24, 2.25 and 2.26). It rests on Layer 4 with a sharp, irregular contact that is inclined toward the south-southwest (Figs. 2.3a, b and 2.4a). Layer 3 is subdivided into two sublayers, which overall are lithologically similar, although Layer 3B is somewhat coarser and richer in flints and exhibits clearer bedding.

Overall, Layer 3 consists of gritty, compact to cemented quartz and limestone sand (Figs. 2.24, 2.25 and 2.26). Layer 3B (Figs. 2.24b and 2.25) is composed of somewhat coarser sand with fewer limestone clasts, but it contains a greater

proportion of lithic and bone materials, which are bedded. The limestone fragments that do exist are rounded and appear to be somewhat dissolved (Fig. 2.24b); the finer matrix material is reddish and sandy, and the lower part is bedded. Many mm-sized calcareous rootlets occur throughout, and the deposits of Layer 3B are particularly well indurated toward the south (e.g., square G and part of square F; Fig. 2.25a–c) because of drip from the brow of the cave that occupied this position at this time.

The contact between Layers 3A and 3B is clear but gradational, particularly in square D, but becomes less clear toward the south. Layer 3A tends to be finer grained but contains many mm- to cm-sized rounded clasts of limestone, many of which appear to be chemically attacked (Fig. 2.24d). In addition, Layer 3A on the whole contains a higher proportion of coarser material to the south than does Layer 3B (Figs. 2.3 and 2.4a), so that in square E11 some angular clasts of roof fall (up to 10 cm) can be observed; there is also

Fig. 2.16 **a** Scan of sample 123 (Layer 5B; Sq. H13). Note the large limestone clast at the bottom and smaller, more rounded limestone grains scattered throughout the matrix. **b** Scan of sample 29 (Layer 5A; Sq. D11), showing numerous angular fragments of burned bone and well-rounded limestone clasts with reddish iron-rich dusty clay coatings. **c** Scan of sample 31bis (Layer 5A; Sq. F11). Note rounding of many of the larger, cm-sized limestone grains by cryoturbation

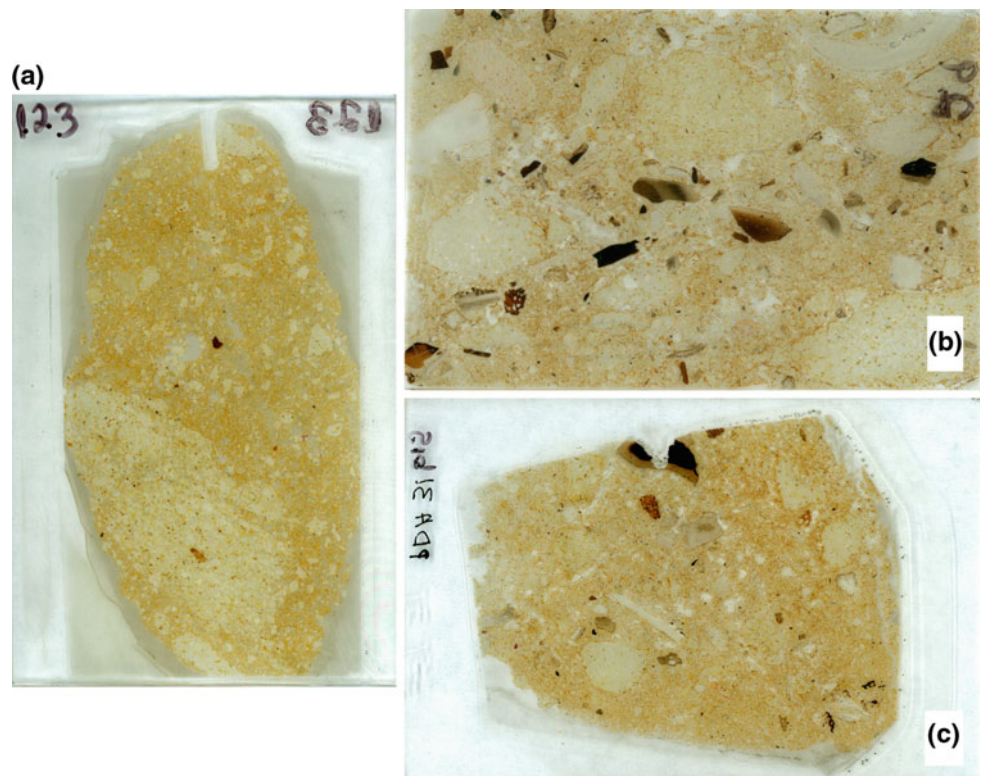
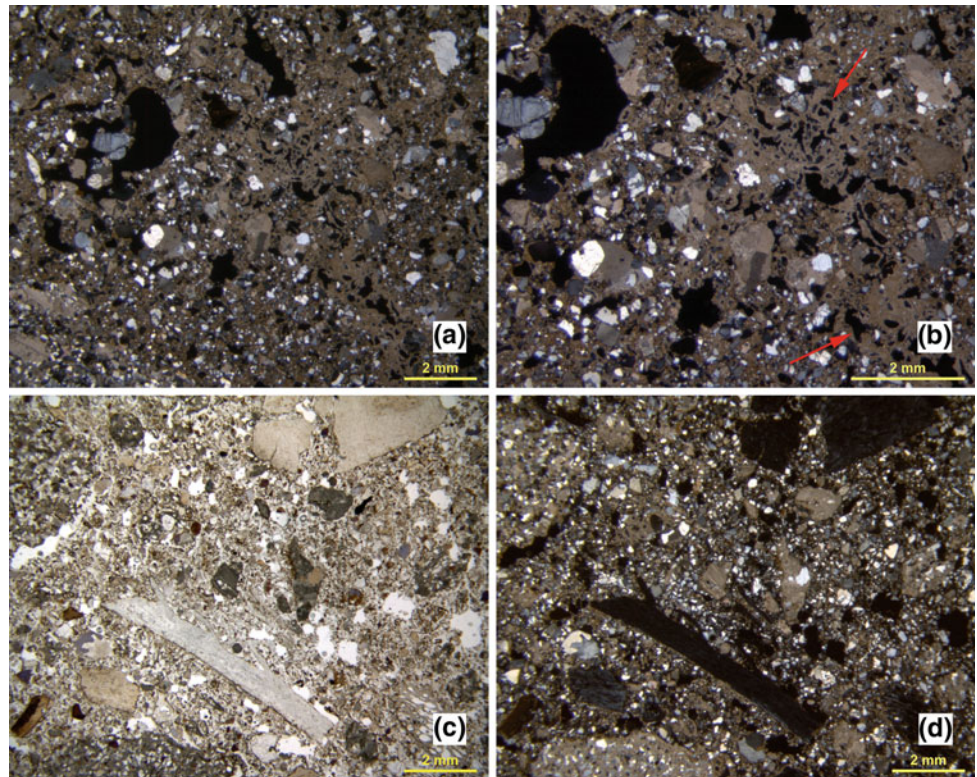


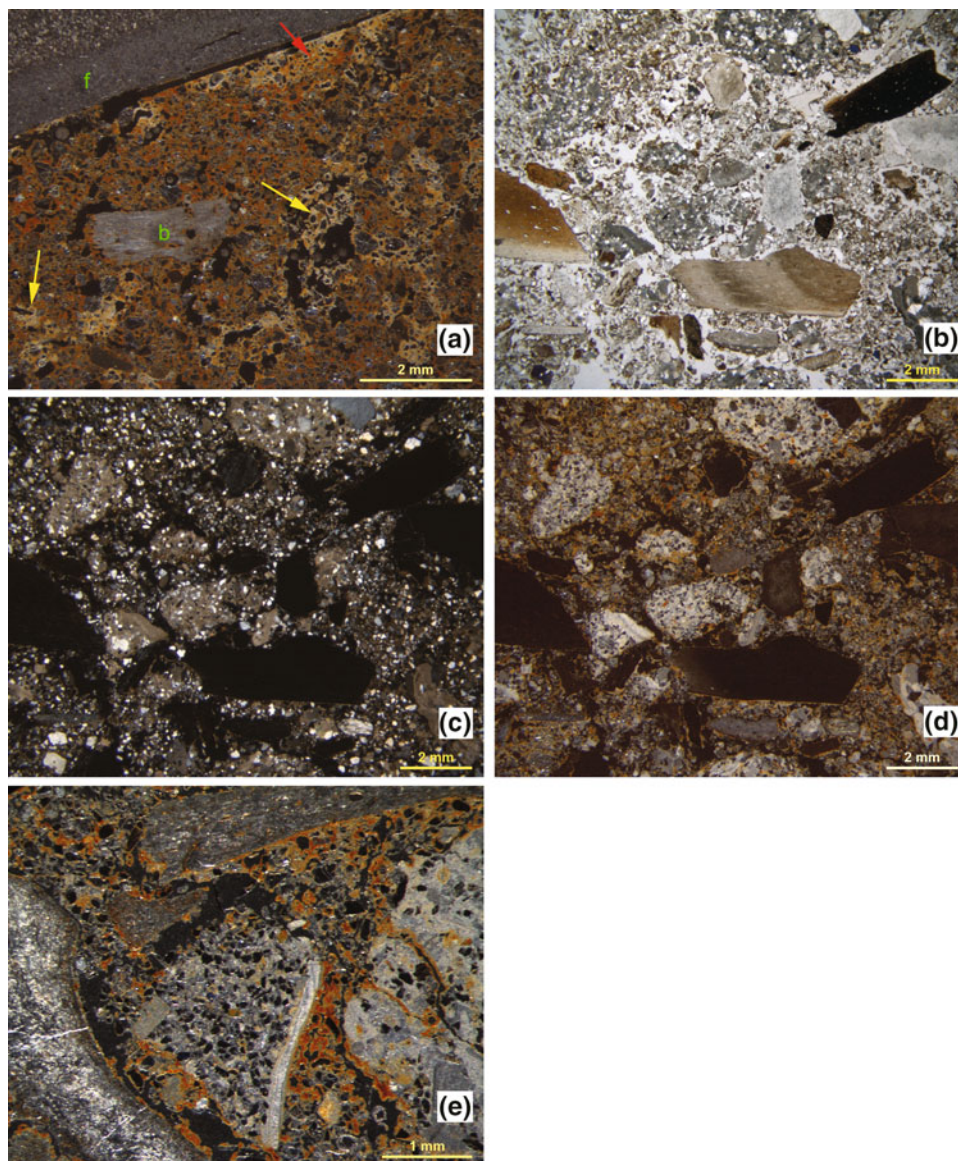
Fig. 2.17 **a** Sample 123 (Layer 5B), which is characterized by relatively abundant calcified roots that are shown in greater detail in **b**. XPL. **b** Detail of sample 123 shown in **a**. The hypocotings and porous calcified fine roots (arrows) are more apparent in this view. XPL. **c** Sample 31bis (Layer 5A). Angular bone and flint fragments in a sandy matrix of quartz and clasts of calcareous bedrock. **d** Sample 31bis (Layer 5A). Same as in **c** but in XPL. Note the rounding of some of the coarser bedrock sand, likely associated with cryoturbation and solifluction



a greater abundance of cm-sized rounded clasts in Layer 3A. On the other hand, towards the wall at the north end of the excavations (square D/C), the sediments become

increasingly sandy, as was the case for Layer 4A. In squares C12 and 13, for example, the sediment consists of massive, firm reddish sand (Figs. 2.3b and 2.4).

Fig. 2.18 **a** Sample 31bis (Layer 5A). Dark field photomicrograph of flint flake (*f*) and bone fragment (*b*). Note the red staining of iron-rich dusty clay, which formed coevally with calcite around many of the roots. The latter is shown by the iron staining of calcified roots (*red arrows*), as well as a late phase of calcification that is not iron stained (*yellow arrow*). **b** Sample 29 (Layer 5A; Sq. D11) with many burned bone fragments, the lowermost of which appears calcined. PPL. **c** Same as **b** but in XPL. Note the overall calcareous nature of the deposit, with little, if any, dissolution of carbonates. **d** Sample 29 (Layer 5A; Sq. D11) as **b** and **c** but with dark field illumination, showing the well-rounded nature of the limestone clasts, and thin coatings of reddish iron-rich clay. **e** Sample 29 (Layer 5A; Sq. D11), a detailed view with dark field illumination. Note the thin iron-rich staining and coatings of many of the clasts, which are composed of limestone and chert



Layer 3B is about 15 cm thick whereas Layer 3A is about 70 cm in thickness. The correlations with the East Section are not definitive (Figs. 2.7 and 2.8), as the connecting section between them was removed during Bordes' excavations.

Layer 2 (Possibly Bordes' Level D?)

This layer occurs only in a limited part of the West Section (Figs. 2.3b and 2.4a), partially as a result of truncation by Layer 1 in historical times. Limited exposures occur in squares F and E11 where the sediments appear as a jumble of mostly limestone cobbles of various sizes (a few mm up to 25 cm diameter) and shapes (angular to sub-rounded). In between the stones is a matrix composed of silty, mostly calcareous sand, which appears to represent local breakdown

of the bedrock clasts. The matrix is partially cemented with numerous very fine, mm-sized rhizoliths.

The overlying contact with Layer 1C, which truncates it (Figs. 2.3b and 2.4a) is quite sharp, whereas the contact with Layer 3A and 3B to the north is much more subtle. Nevertheless, Layer 2 can be distinguished from Layer 3 by the fact that the matrix in Layer 2 is sandier and contains fewer granule-sized fragments of limestone than does Layer 3. The Layer 2/3 contact is somewhat vertical and almost basin shaped. The upper part is washed somewhat by movement of water associated with what probably represents historical disturbance.

Layer 2 appears to represent a small depression (either basin or trench) probably produced by water cascading from the former brow of the cave. This depression was filled as a

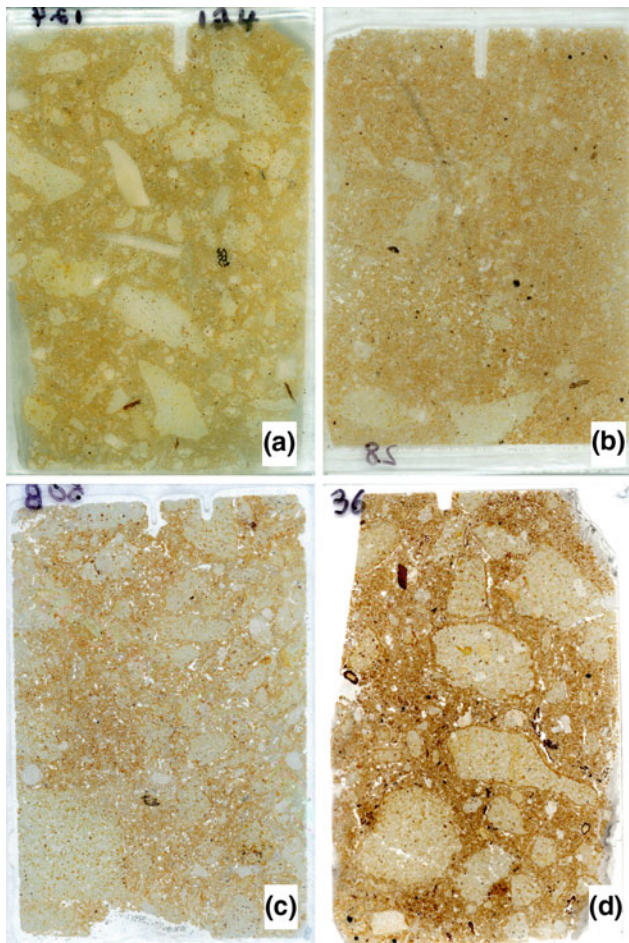


Fig. 2.19 **a** Scan of sample 124 (Layer 4C; Sq. H11). Rounded and angular limestone clasts with isolated fragments of burned bone. **b** Scan of sample 28 (Layer 4B; Sq. D11). This sample, close to the rear wall of the excavations, is finer than equivalent samples in the same layer farther to the south, away from the wall, reflecting partial dissolution of the limestone clasts. **c** Scan of sample 50B (Layer 4A; Sq. F11). Porous mixture of rounded limestone clasts in a sandy matrix with some interstitial reddish brown iron-rich dusty clay. **d** Scan of sample 36 (Layer 4A; Sq. G10). Rounded limestone clasts with fine mm-sized bone fragments in a dusty iron-rich sandy matrix

combined result of large blocks rolling off the brow, as well as by sediment slumping into the depression from Layer 3. The latter would explain the scatter of lithics that were found here in Layer 2. The width of the layer is ~ 1 m and the height ~ 75 cm.

Layers 1A, 1B, 1C, (Possibly Bordes' Levels A₁-D)

This sedimentary complex is a slope and roof fall deposit that formed during historical times, and it truncates many of the underlying deposits (Figs. 2.3b and 2.4a). It encompasses a poorly sorted mixture of angular and rounded limestone boulders, as well as smaller clasts in organic-rich silty sand. Several subdivisions were made based on texture and color:

Layer 1C contains relatively high proportions of cm-sized rock clasts derived from the underlying sediments and has a very sharp contact with these latter deposits. It generally follows the modern slope (Figs. 2.3b and 2.4a). Layer 1B, on the other hand, truncates Layer 1C and consists of sandy clay with abundant worm casts and modern roots. Layer 1A is somewhat finer grained and darker brown and contains many aggregates, roots, and tabular rock fragments. The thickness of the sublayers is generally similar: Layer 1C = ~ 20 – 35 cm; Layer 1B = ~ 40 cm; Layer 1A = ~ 35 cm. Layer 1 does not occur on the east side of the cave, possibly because the original roof is largely more intact there and there is less of a slope (Figs. 2.7a, b and 2.8).

Specific Micromorphological Aspects of the Deposits

Micromorphological analysis of the Pech IV deposits revealed both geogenic and anthropogenic constituents. The majority of the geogenic coarse fraction in all layers is composed of mm- to cm-sized limestone bedrock fragments

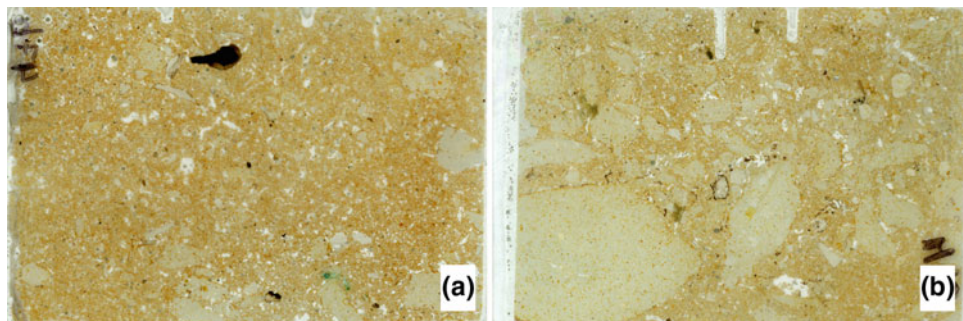
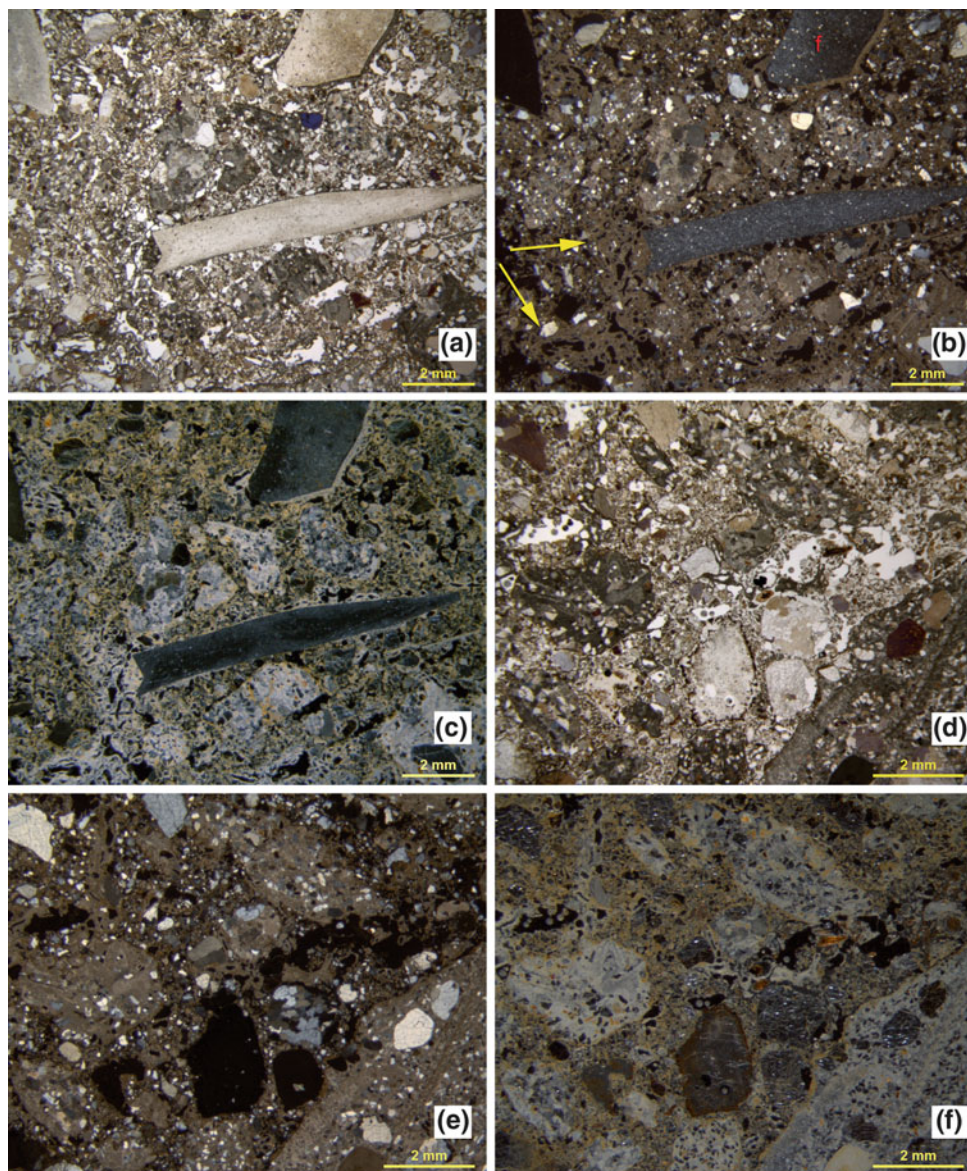


Fig. 2.20 **a** Scan of sample 47B (Layer 4A; Sq. E11). Generally similar to sample 50B but with some burned bones. **b** Scan of samples 49B (Layer 4B; Sq. F11). This overall similar to sample 124 from Layer 4C but slightly more porous. Note also the rounding of the limestone grains

Fig. 2.21 **a** Sample 201 (Layer 4C; Sq. H11) showing flint flakes and rounded limestone clasts. PPL. **b** Sample 124. Same as in **a**, but in XPL. Note the number of flint pieces (*f*) and overall calcareous nature of the sediment, including fresh limestone clasts and calcified roots (*yellow arrows*). **c** Sample 124 as in **a** and **b**, but with dark field illumination, where secondary calcification of roots is more evident. **d** Sample 49B (Layer 4B; Sq. F11). Note the similarity to sample 124, including the presence of limestone grains, which are mostly rounded. PPL. **e** Sample 49B as in **d** but in XPL. **f** Sample 49B with dark field illumination, which shows the orange red iron-rich dusty clay coatings and interstitial infillings



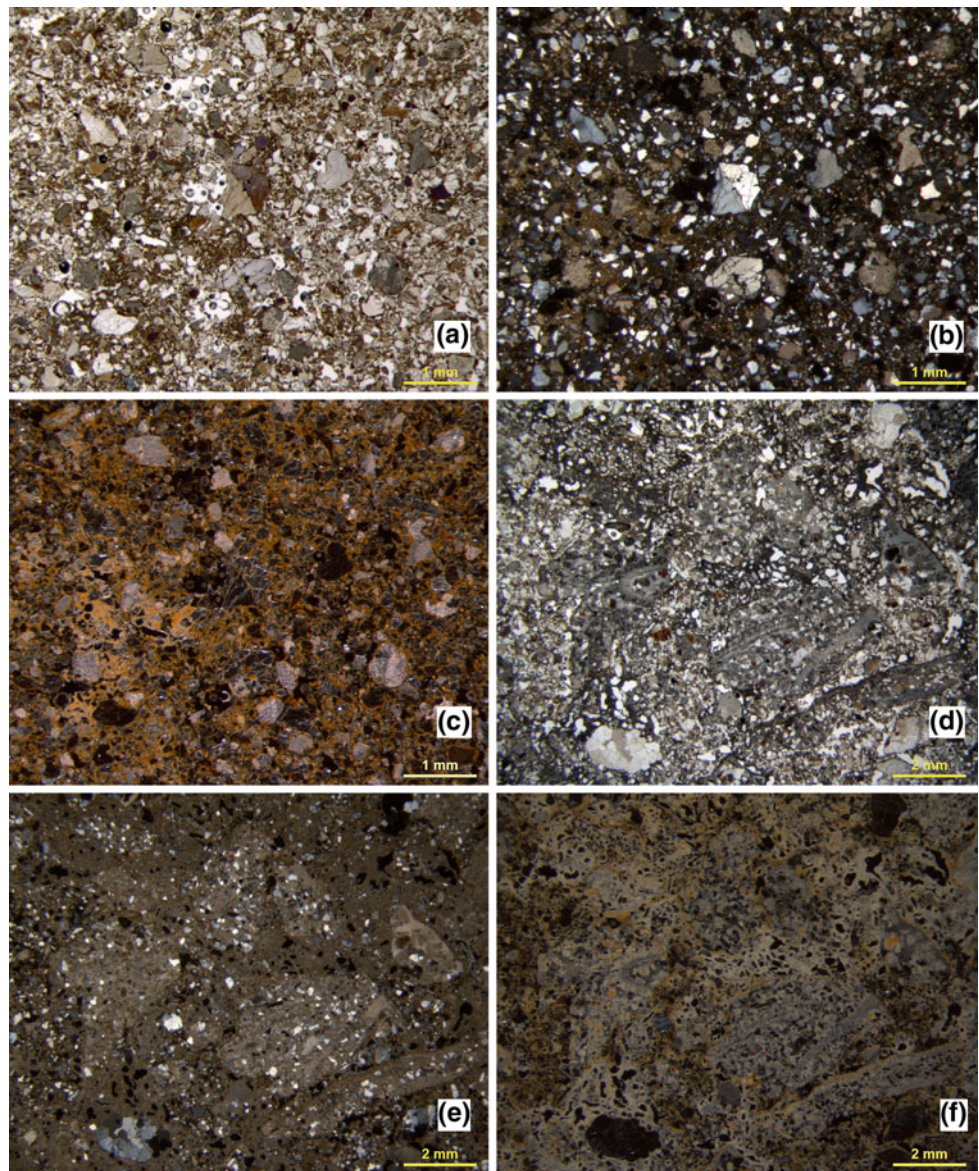
and loose quartz grains ranging in size from silt to coarse sand. Limestone fragments in thin section are commonly rounded (e.g., Figs. 2.10f, 2.13b, 2.16c and 2.19), and boundaries of grains range from sharp to gradational. Less common are natural grains of muscovite, glauconite, carbonate sands, fragments of travertine, and nodules/concretions of iron and manganese oxide. The fine fraction is composed of clays and secondary micritic (calcite) accumulations with a crystallitic birefringence fabric (b-fabric).

In Layers 8, 7, and 6 in particular, the coarse and fine fractions also contain high proportions of anthropogenic material, including bone and tooth fragments, fat-derived char and traces of charcoal, flint fragments, and ash (Layer 8 only); bones (burned and unburned) and flint artifacts occur in other layers (e.g., Layer 5; Fig. 2.16b–c), but in much

lower numbers. Overall, however, fragments of bone and teeth make up the largest proportion of the anthropogenic coarse fraction. They are angular to rounded and are comparatively small, both in the field and in thin section; average fragment sizes range from ~0.25–2 cm. The bones are both fresh and burned, with a range in color from yellow to dark brown (e.g., Fig. 2.11a, b). Anthropogenic materials from samples above Layer 6 are generally isolated bone fragments, which are often sand-sized and subangular to rounded, but (e.g., sample 29, square D11, Layer 5A) they can be more locally abundant (e.g., Fig. 2.16b). Above Layer 6, biogenic materials are virtually absent, with the exception of a single coprolite fragment from sample 5 (square F19, Layer 5B).

The anthropogenic components of Layers 8, 7, and 6 deserve separate mention, particularly in the lowermost

Fig. 2.22 **a** Sample 28 (Layer 4B; Sq. D11). This sample, which is close to the north wall of the excavations, consists of quartz sand and some rounded, sand-sized grains of limestone. PPL. **b** Sample 28: as in **a** but in XPL. The greater proportion of siliclastics in this wall sediment is evident as can be seen in Fig. 2.3b. **c** Sample 28 with dark field illumination. Not the abundance of reddish iron-rich dusty clay, which is reflected in the field as well (Fig. 2.3b). **d** Sample 50B (Layer 4A; Sq. F11), overall similar to sample 124 in Sq. H11 (Layer 4C) in their degree of secondary calcification, reflecting former positions of the dripline. PPL. **e** Sample 50B but in XPL and showing the rounded clasts of limestone and abundance of secondary calcite. **f** Sample 50B same view as in (p) and (q) but with dark field illumination, showing numerous calcified rootlets throughout



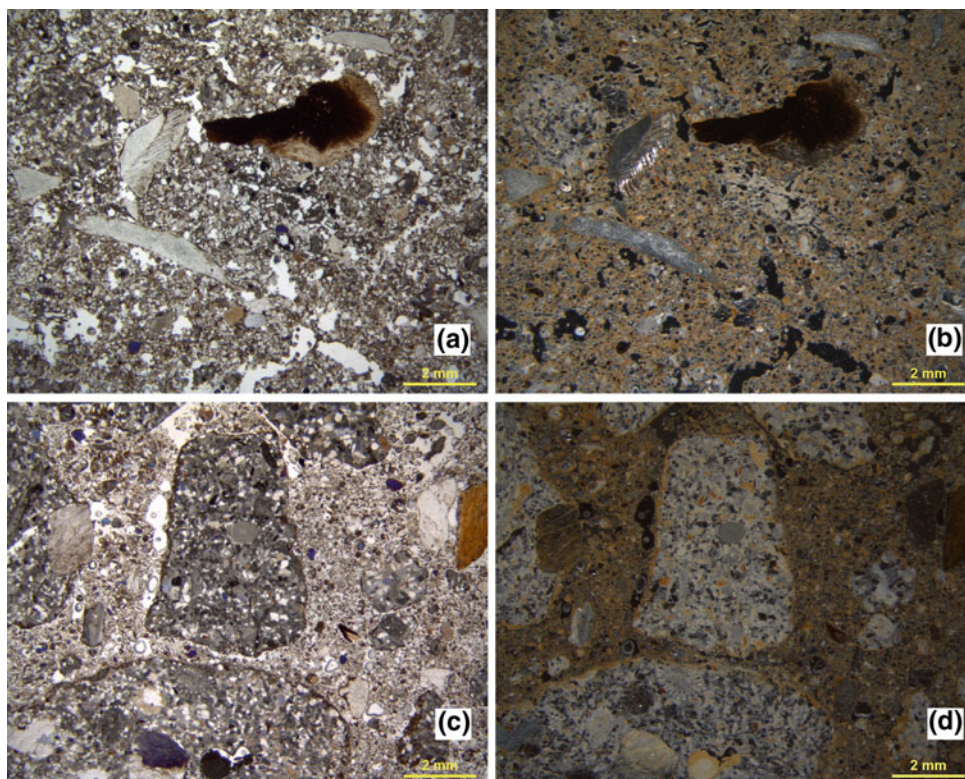
layer. Burned bone is present in nearly every sample, and in most slides, it is homogeneously mixed with unburned bone, and commonly exhibits layering. On the other hand, both in the field and in macro scans of the thin sections, bones can be seen concentrated into cm-thick zones, some of which correspond to large, roughly circular burned features that were excavated in 2002 (Fig. 2.9).

Several bone fragments in Layer 8 exhibit in situ break-age—scissor fractures—in which angular pieces of the bone refit and are only barely separated (Figs. 2.8a, d and 2.9e–f); these types of fracture are produced by trampling (Miller et al. 2010). Bone fragments also exhibit some post-depositional chemical features. Many are partially or fully stained with iron or coated with iron-rich dusty clay (e.g., Figs. 2.9e–f and 2.14b–c). Interestingly, such chemical changes do not appear to have affected bone preservation, as

the bones are quite compact during excavation and distinct in thin section. Charcoal is present in Layer 8, but is relatively rare. Rather, the dark material that is responsible for the striking color of Layer 8 is fat-derived char resulting from burning of bones and commonly characterized by a dense vesicular black mass that is commonly fractured (Figs. 2.8b, d and 2.9a, b) (Ligouis 2006).

Wood ashes in Layer 8 (Fig. 2.7a, c, d, f) occur as three main types. The first is well preserved, nearly pure layers (~5 mm thick) containing intact rhomb-shaped calcite grains. These layers are compact, massive, and laminated and are cemented by secondary micrite (microcrystalline calcite) (Figs. 2.9d and 2.10a, b). The second type of ash occurs as isolated pieces of cemented ash layers reworked by trampling or possibly cryoturbation. The third type of ash occurs as distributed grains of particles in the groundmass

Fig. 2.23 **a** Sample 47B (Layer 4A; Sq. E11) with burned bone fragment and rounded and platy limestone grains; an angular splinter of chert is visible at the left. PPL. **b** Sample 47B as in **a**, but with dark field illumination. More visible in this view is the presence of calcified roots just below the burned bone, as well as the reddish brown interstitial iron-rich dusty clay. **c** Sample 36 (Layer 4A; Sq. G10) with rounded limestone clasts and a burned bone. PPL. **d** Sample same as in **c** but with dark field illumination. Note the relative abundance of reddish iron-rich dusty clay as coatings around the limestone grains and as in interstitial positions between the quartz sand



and these are commonly re-cemented by calcite (Fig. 2.10a, b). This loose ash also contains rhomb-shaped grains but is dustier in appearance due to the incorporation of other materials, such as clay-sized grains and charcoal fragments. Ash mixed with groundmass often caps large fragments of limestone, flint, and bone or appears directly beneath such objects (Fig. 2.10a, b).

The composition, internal organization, and external geometry of the anthropogenic components provide clear evidence that burning events occurred during the deposition of Layer 8 and possibly Layer 6. These events, exemplified by the intact stringers of ash overlying carbon-rich layers, likely correspond spatially to the round combustion structures excavated in 2002.

The fissures present in some of the cemented layers indicate that the cementation likely occurred relatively soon after deposition and not much later. On the other hand, Layer 8 also exhibits features associated with carbonate dissolution: as mentioned above, many limestone fragments appear to be actively dissolving and many cemented ash fragments often contain thin channel voids, which are characteristic of calcite depletion (Bullock et al. 1985). Compared to Layer 5 and above, however, calcite in the lowest layers is relatively well preserved. This preservation may result from the physical protection and groundwater buffering capacity of the limestone roof blocks of Layer 6B. In any case, the ashes are primarily composed of calcite and do not show any signs

of secondary phosphatic diagenesis, as is the case at Roc de Marsal (Goldberg et al. 2012).

The upper layers of the site are markedly different from Layer 8 in color, anthropogenic content, percentage of coarse material, and abundance of limestone fragments. There are also differences among these layers and lateral variations within them.

A characteristic of many of the deposits—particularly those of Layer 6 (sample 32/6A; sample 201/6B), Layer 5B (e.g., samples 119, 120) and slightly less so for Layer 5A (sample 12), Layer 4 (sample 124/4C; sample 49B; samples 20, 36, 48/4A), and Layer 3 (e.g., sample 17, 26B/3B; samples 27, 45/3A)—is the presence of cm-sized rounded clasts of limestone. Most of them are relatively fresh (e.g., sample 124—Layer 4C; Fig. 2.19a), but in some cases, where sediments have undergone some decalcification (e.g., square D11), they are somewhat etched and their surfaces are indented and not smooth (e.g., sample 50B—Layer 4A, square F11; Fig. 2.19c). In addition, many exhibit thin (~10 μm thick) discontinuous coatings of reddish brown iron-rich dusty clay (e.g., sample 36, Layer 4A, square G10; Figs. 2.19d and 2.23c, d). The fact that these coatings usually do not coat grains uniformly or completely and are not specifically oriented on a specific part (e.g., upper surface) indicate that these grains have been moved and rotated, which suggests solifluction, cryoturbation, and/or frost creep. Such processes match the overall depositional style of

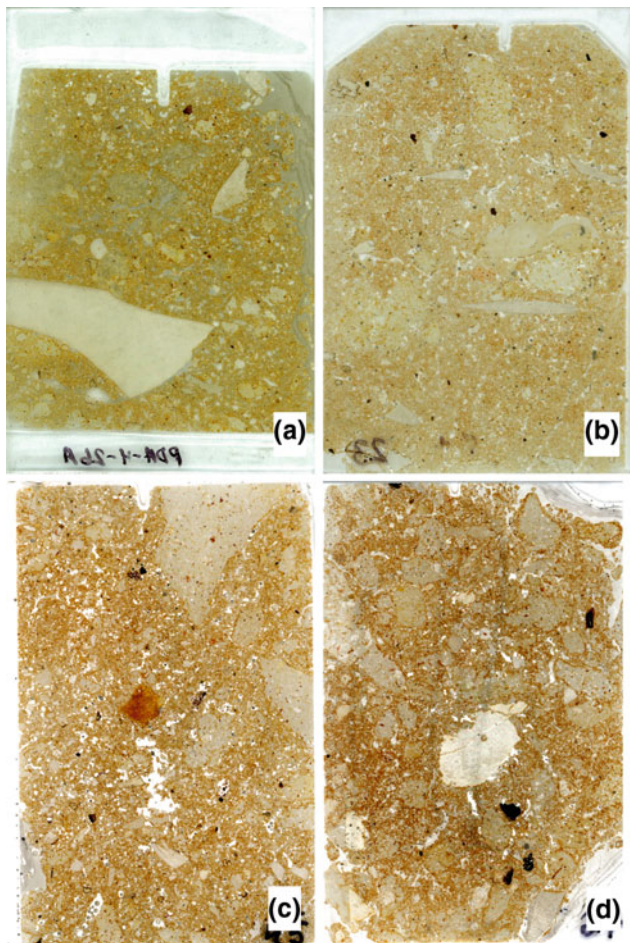


Fig. 2.24 **a** Scan of sample 26A (Layer 3B; Sq. E11). **b** Scan of sample 23 (Layer 3B; Sq. D11). **c** Scan of sample 45 (Layer 3A; Sq. E11). **d** Scan of sample 27 (Layer 3A; Sq. D11)

the sediments as viewed in the field, particularly the sharp erosional contacts at the base of Layers 5B, 4C, and 3B (Figs. 2.3b and 2.4a).

As stated above, the sediments in Layer 8 are the most striking in the field by their color, and the presence of intact hearths and redistributed hearth materials. These aspects are complemented in the thin sections by the relative abundance of burned bone, fat-derived char, some charcoal, and various forms of calcareous ashes. Although none of the overlying layers is as striking as those in Layer 8, some do contain remains of these anthropogenic elements. For example, Layer 6—particularly in the East section (e.g., Sq. E19, sample 4B; Fig. 2.15c)—exhibits bedded burned and unburned bones, flint debris, and a dark brown, organic-rich matrix. On the West Section, accumulations of burned bone in Layer 6 are much less abundant (e.g., sample 8—Sq. D13; Fig. 2.15d) and the matrix is more sandy and less organic. Above Layer 6, the amount of burned bone visible in the field and in thin section drops off, and only a few samples exhibit them, mostly in the form of generally isolated mm- to

cm-sized angular bits of burned bone (e.g., Figs. 2.8b, c and 2.9a, b, e). Interestingly, none of the deposits above Layer 6 displays organic-rich matrices.

Although some samples above Layer 8 contain burned bone, none includes charcoal, ash fragments, or organic groundmass. Layer 6 on the East Section is most similar to Layers 7 and 8 in color and content, as it also contains burned bones and occasionally, small fragments of charcoal. Layers 5 through 1 contain less groundmass and fewer limestone fragments than Layers 7 and 8.

Artifact Orientations

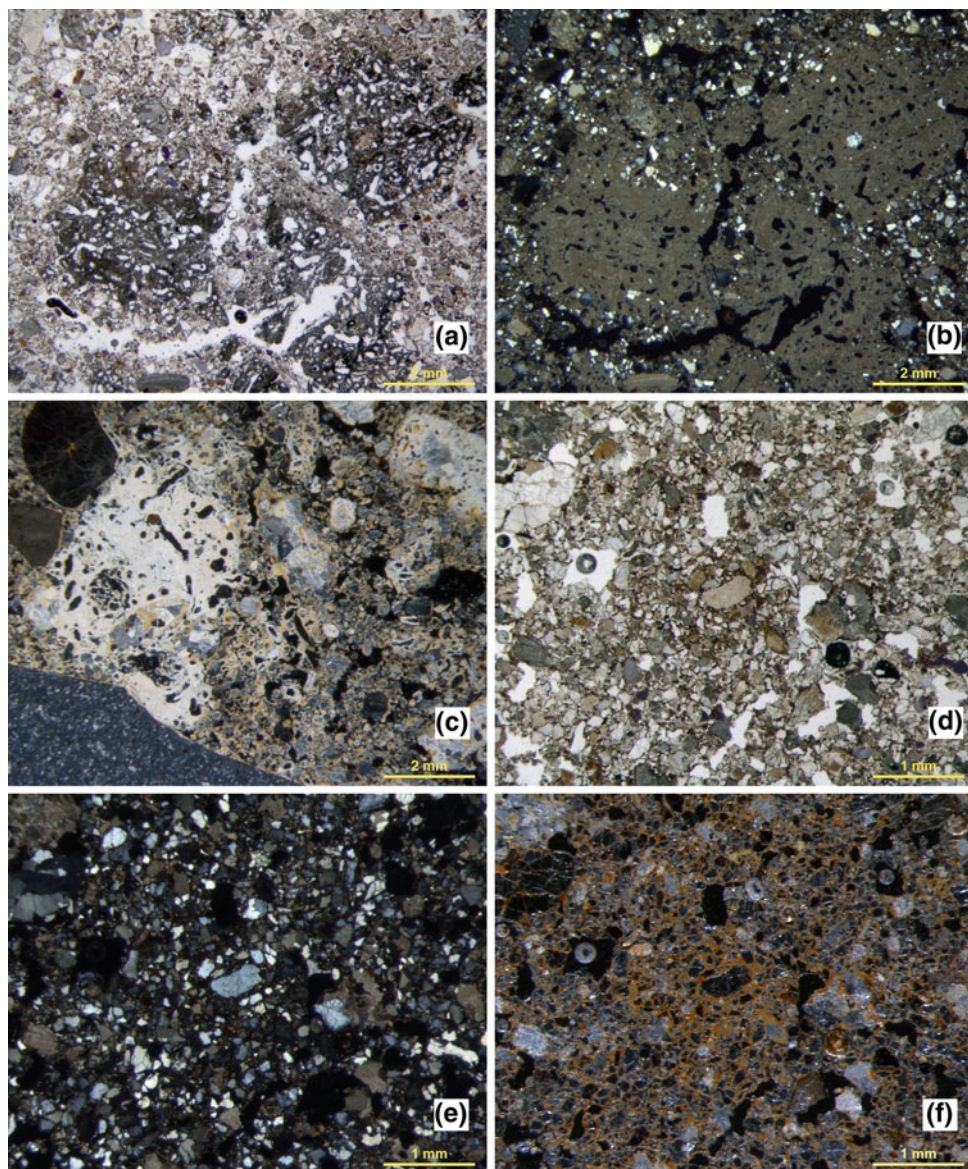
The methodology used to record artifact orientations with a total station is described elsewhere (Chap. 1). Most of the techniques applied here for analyzing and representing these data have been previously described (McPherron 2005); however, also presented here are new techniques for intra-site spatial analysis to understand better variability and the effects of sample size, and to compare levels statistically.

Methods

Because each elongated artifact is measured with only two points, its orientation can be described using only its bearing and plunge. The mean bearing angle and circular variance for a given level are calculated using circular statistics. The uniformity of the bearing angle distribution is assessed using Rayleigh's test. Significance ($p < 0.05$) indicates a nonuniform distribution of bearing angles the structure of which can be viewed using Rose diagrams. Because plunge values vary between 0 and 90° and do not cycle through this range (i.e., 90° and 0° are not the same thing and angles greater than 91° cannot exist), in contrast to previous publications (e.g., McPherron and Dibble 2007), the mean plunge angle and its variance are calculated using standard, rather than circular, statistics. The uniformity of plunge angles is assessed using a Kolmogorov–Smirnov (K–S) test with significance ($p < 0.05$) indicating a nonuniform distribution. In addition, the strength of the artifact orientations is reported here as the sum of the normalized orientation vectors (L), which includes both bearing and plunge information. Values approaching 1 indicate preferred orientations; zero indicates no preferred orientation.

To assess artifact orientations further, eigenvalues are computed on the normalized orientation vectors and transformed into shape ratios which are plotted on Benn diagrams (see Benn 1994; Lenoble and Bertran; McPherron 2005 for more details). The set of normalized three-dimensional vectors from a layer is reduced to three eigenvalues ranging from zero to one, descending in value, and totaling to one.

Fig. 2.25 **a** Sample 26A (Layer 3B; Sq. E11) showing reworked clasts of reworked calcified roots. PPL. **b** XPL view of **a**, showing the sharp borders of the calcified root fragment. **c** Sample 26A with different phases of calcification of roots, the earlier ones with reddish iron staining. Dark field illumination. **d** Sample 23 (Layer 3B; Sq. D11) composed predominantly of sand-sized components, mostly quartz with smaller amounts of limestone grains. PPL. **e** Sample 23. Same view as **d** but in XPL and showing the quartz-rich nature of the sample and relatively small proportion of calcitic grains. **f** Sample 23. Dark field illumination of **d** and **e**, with reddish iron-rich dusty clay coatings and interstitial fillings and overall lack of carbonate grains or components



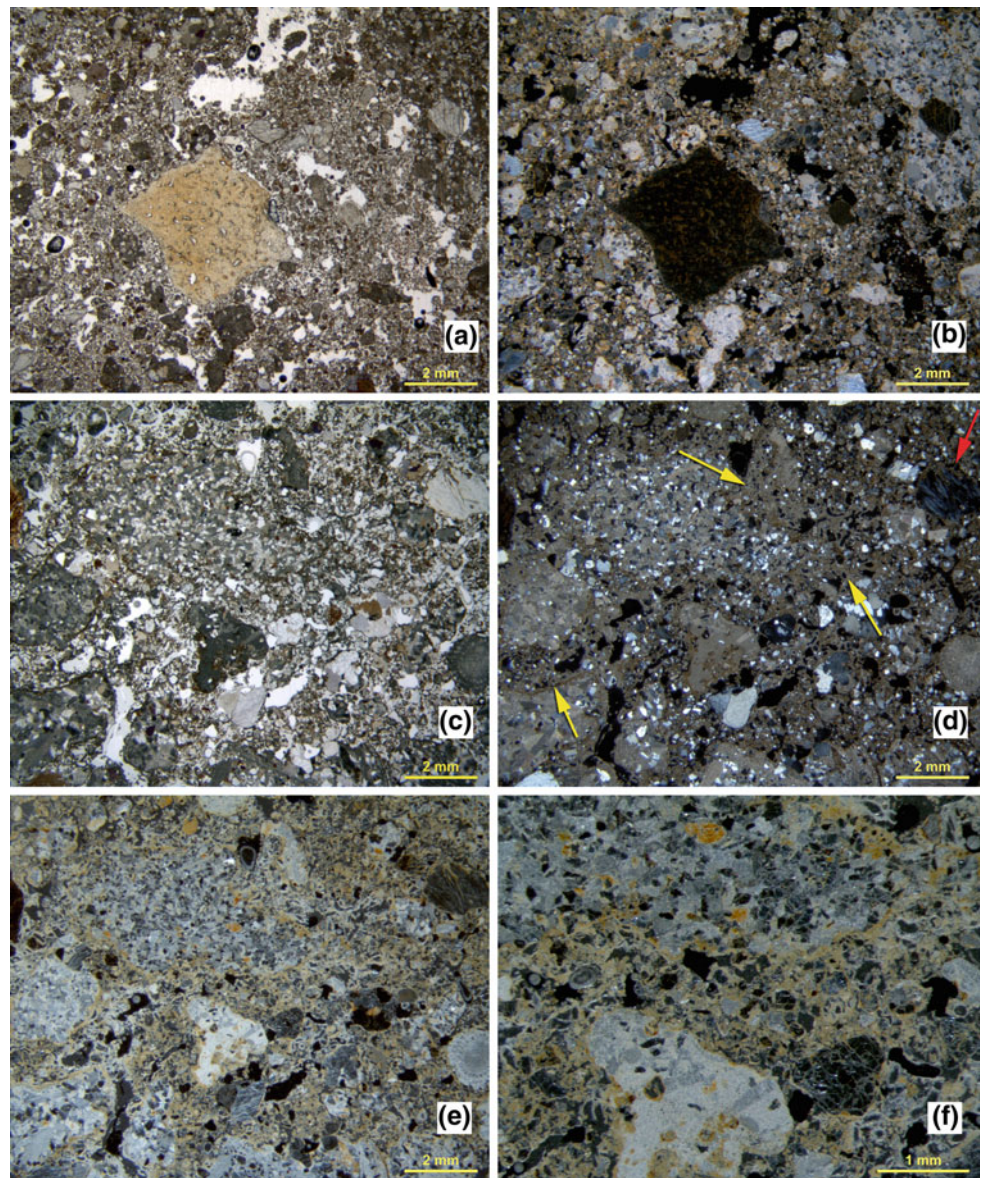
When the first eigenvalue is high (i.e., approaches 1) the orientations are highly linear. When the first two eigenvalues are roughly equal, the orientations are randomly distributed on a plane (though not necessarily on a horizontal plane). And when all three eigenvalues are roughly equal, the orientations are isotropic. These three patterns can be visualized using two shape ratios: elongation and isotropy. Elongation is calculated as $1 - E2/E1$ where $E2$ and $E1$ are the second and first eigenvalues, respectively. Isotropy is calculated as $E3/E1$ where $E3$ is the third eigenvalue.

The elongation and isotropy ratios are then plotted on a modified ternary diagram (a Benn diagram) in which the three poles correspond to linear, planar, and isotropic orientations. A ternary diagram with only two variables is preferred over a standard Cartesian XY plot because some regions of the XY space will never have points (because of

the mathematical constraints on eigenvalues listed above). In a Benn diagram, the planar region is the expected outcome for artifacts dropped on a flat (though not necessarily level) surface and left unmodified by subsequent depositional processes. Site formation processes will normally alter this state and introduce some combination of linearity or isotropy into the artifact orientations. As such, these processes will pull the plotted point away from the planar region of the Benn diagram. For instance, if the surface is irregular, variance in plunge angles will increase, and this will increase the isotropy (pulling the point closer to the isotropic pole).

There are no statistical tests to show whether a layer differs significantly from an ideal planar orientation, and it is difficult to know how many artifacts are necessary to have a robust pattern. Here, these issues are addressed through resampling. The Benn diagrams for each layer are displayed

Fig. 2.26 **a** Sample 45 (Layer 3A). Bone fragment in loose calcareous sand. PPL. **b** Sample 45. Dark field view of a showing granular nature of matrix composed of rounded coarse calcareous sand and granules. Some reddish iron-rich dusty clay is present in the matrix and coats some of the grains. **c** Sample 27 (layer 3A; Sq. E11), which is overall similar to sample 45 but somewhat more cemented by calcite. PPL. **d** Sample 27, XPL view of **c** showing cementation of limestone grains as well as abundant calcified roots (yellow arrows). A bone fragment (red arrow) can be seen in the upper right. **e** Sample 27 as in **c** and with dark field illumination. The widespread cementation of calcite is visible here. **f** Sample 27. Detailed view of **e** with secondary calcite cementing the grains, dark field



with 95% confidence intervals derived by drawing a random sample, with replacement, from the artifacts of that layer with a sample size equal to that layer. Each layer was resampled 10,000 times. This value was selected because it produced a relatively smooth and stable probability distribution. Similarly, there are no statistical tests of significance for differences in Benn ratios. Thus, to assess whether layers differed from one another, Fisher's exact test was estimated using resampling. This involved combining the two assemblages being compared and then drawing two random samples, without replacement, with sizes equal to the original two layers under comparison. Technically this involves randomly selecting a sample equal in size to one of the assemblages and then assigning the remaining artifacts to a second sample. The distribution of Euclidean distances is then derived using the elongation and isotropy ratios, and the

distance of the original two layers under consideration is compared to the resampling distribution to assign a probability to that distance. A one-tail probability of $p < 0.05$ was used to assess significance because in this case, we are only interested in one portion of the distance distributions, namely those that are likely dissimilar.

In addition to these statistical procedures and the Benn diagrams, the orientation distributions are displayed in Fig. 2.27 to help with their interpretation. Thus, for each layer, a plot is made showing the spatial distribution of the artifacts used in the analysis. In addition, a Schmidt lower hemisphere diagram shows the distribution of bearing and plunge values. Schmidt diagrams place one end of the vector representing the artifact orientation at the center of a sphere and then plot where the other end of the artifact exits the sphere. Here, the lower hemisphere is plotted, meaning that

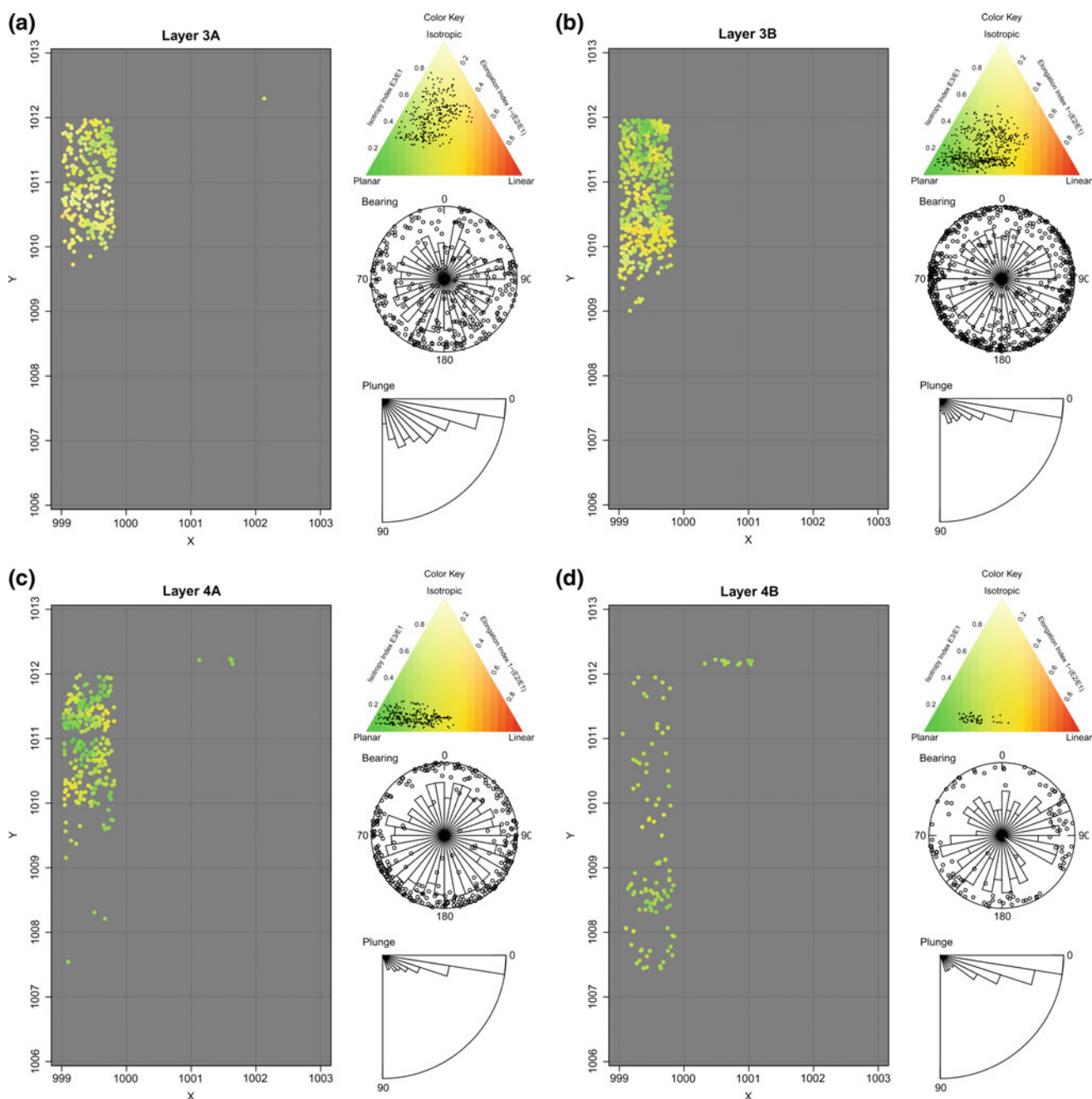


Fig. 2.27 a–k Pech IV artifact orientations. On the *left* is the distribution of finds used in the orientation analysis. The *color codes* represent where in the Binn diagram (on the *upper right*) an assemblage made of that artifact and its nearest 40 artifacts would

fall. *Middle right* is a Schmidt lower hemisphere diagram with a superimposed Rose diagram with ten degree intervals. *Bottom right* is a modified Rose diagram showing the distribution of plunge angles

the high point on each artifact is placed at the center of the sphere and as a result, the orientation vector must exit the lower hemisphere. To view this three-dimensional object in two dimensions, the exit point is projected onto the central plane of the hemisphere (a two-dimensional circle). Artifacts that are relatively flat will plot towards the margins of the circle. Artifacts that plunge steeply will plot towards the

center. The place where an artifact plots along the circle (0° – 360°) indicates the direction in which the artifact is sloping. At Pech IV, angles of 0° point directly into the cliff face, 180° angles point into the valley, and 90° angles point downstream. To better appreciate potential patterns in these dot plots, a Rose diagram (a circular histogram) is superimposed on the Schmidt diagram to summarize the number

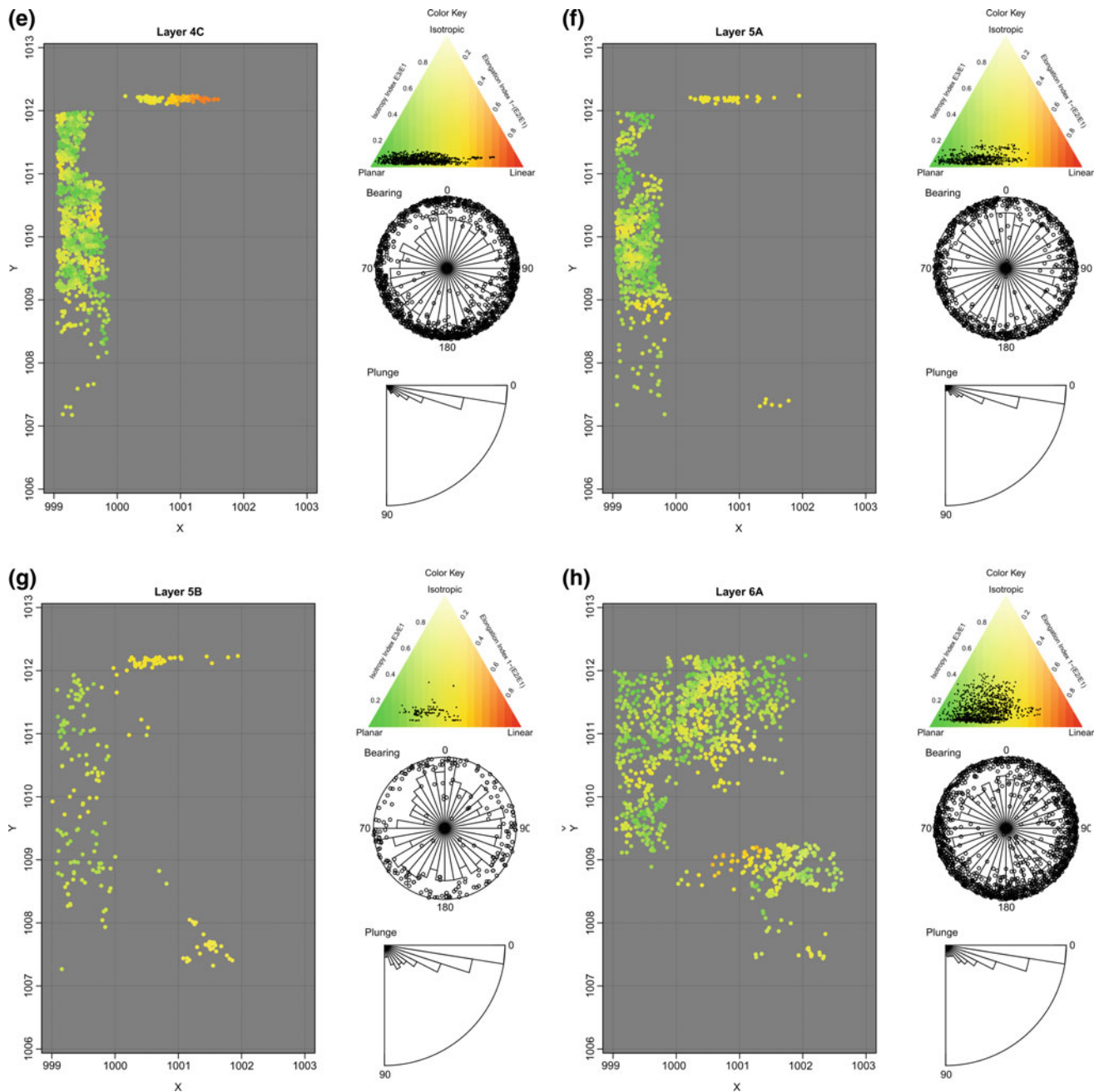


Fig. 2.27 (continued)

of bearing angles that fall within each Rose diagram interval (here 10°). Plunge angles are summarized separately using a modified Rose diagram that shows angles from 0° to 90° (again, plunge values greater than 90° are impossible).

In addition to this figure, spatial variability within a layer is assessed using Bann values calculated based on neighboring artifacts. Here, the nearest 40 artifacts in a layer are used to calculate Bann statistics (elongation and isotropy). A color space is then mapped onto the Bann

diagram so that a plan view of each layer can be plotted with the color of each artifact representing the position in Bann space of the ratios computed from the neighboring 40 artifacts. This number of artifacts was selected arbitrarily to balance having enough artifacts to compute meaningful Bann statistics and at the same time to remain sensitive to spatial variations in these values. Next to each of these plots, a Bann diagram key is plotted with the color space indicated and with each artifact's associated Bann values plotted.

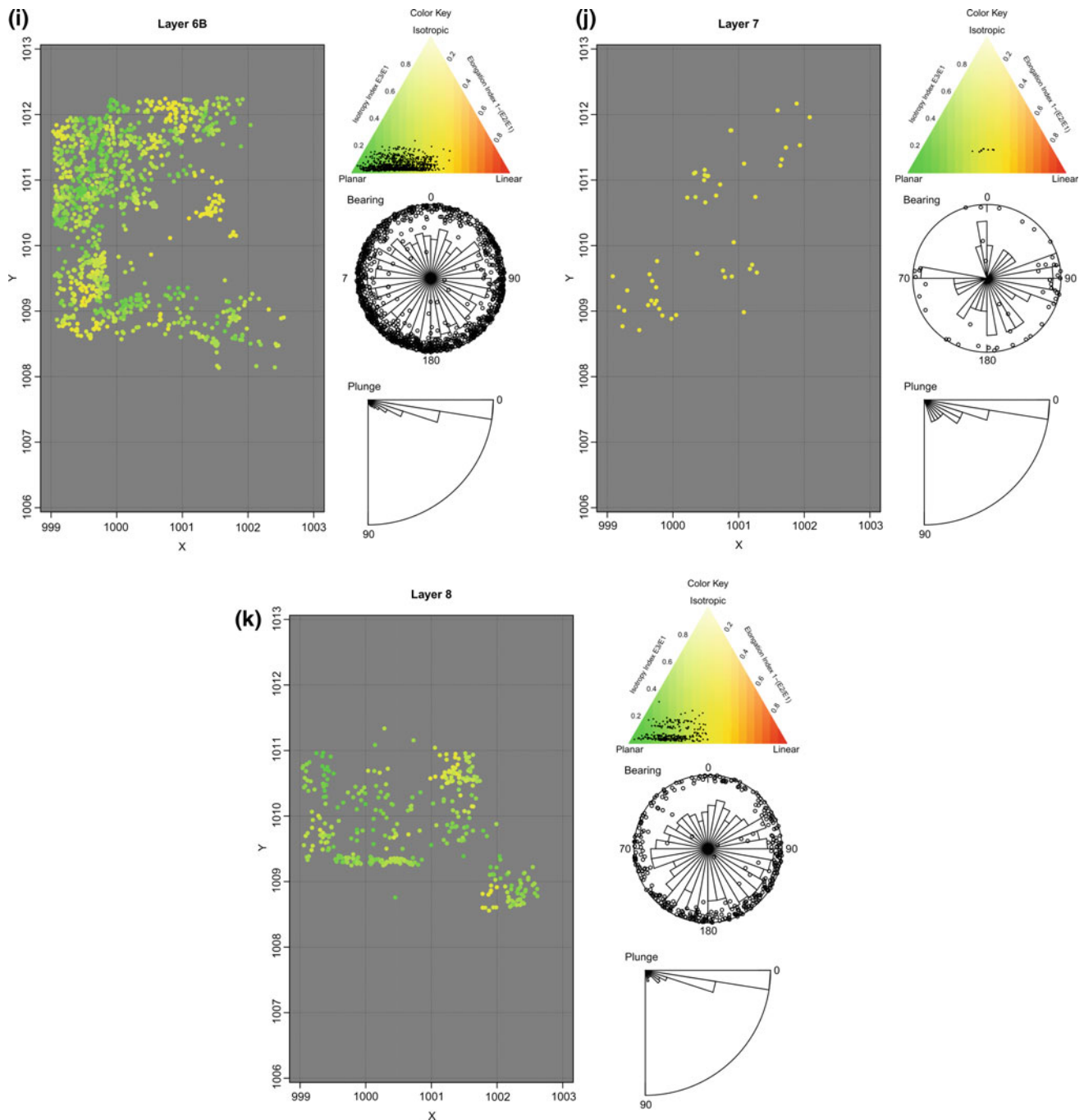


Fig. 2.27 (continued)

These diagrams give some indication of the variability within each layer that is not apparent in the 95% confidence intervals and at the same time give some indication as to whether this variability has a spatial component.

All of the statistics and plots presented here were generated in R (R Core Team 2014). Bearing angles were assessed using the CircStats package (Lund & R port by

Claudio Agostinelli 2012; CircStats: Circular Statistics 2012). The Rose diagrams were plotted with a modified version of code from this same package. Benn diagrams were modified from the ternary plots in the VCD package (Meyer et al. 2014). All of the remaining code was written by McPherron.

Table 2.4 Bearing and plunge statistics for the Pech IV layers

		Length		Bearing				Plunge			
Layer	N	Mean	s.d.	L	Mean	Var	P	L	Mean	Var	P
3A	318	0.052	0.023	0.17	170.3	47.4	0	0.92	24.6	23.1	0
3B	586	0.054	0.019	0.11	197.3	51	0	0.96	14	17.2	0
4A	301	0.066	0.027	0.17	172	47.5	0	0.98	10	11.9	0
4B	110	0.061	0.021	0.13	164.5	49.6	0.14	0.98	12.1	11	0
4C	1143	0.062	0.021	0.17	156	47.4	0	0.99	8.6	8.6	0
5A	764	0.061	0.022	0.05	175.7	54.5	0.16	0.99	8.9	9.4	0
5B	210	0.07	0.026	0.04	108.3	55	0.72	0.96	14	15.6	0
6A	1237	0.06	0.021	0.15	153	48.7	0	0.97	12.1	13.2	0
6B	1101	0.063	0.021	0.18	198.4	46.7	0	0.99	8.2	8.6	0
7	50	0.058	0.012	0.36	114.9	36.6	0	0.97	12.4	15.3	0
8	363	0.053	0.019	0.23	151.5	44	0	0.99	7.6	9.5	0

The first column is the sample size. The next two columns are the mean artifact length and standard deviation based on the distance between the two points used to record its orientation. Next are the bearing statistics with the vector magnitude statistic (L), the mean bearing, the circular variance, and the Rayleigh test for uniformity. The same are presented for the plunge angles

Table 2.5 Eigenvalues and Benn ratios (Isotropy and Elongation) for the Pech IV artifact orientations

Layer	E1	E2	E3	IS	EL
3A	0.397	0.386	0.217	0.546	0.029
3B	0.476	0.415	0.107	0.225	0.129
4A	0.491	0.45	0.059	0.12	0.082
4B	0.55	0.384	0.066	0.119	0.301
4C	0.499	0.462	0.039	0.078	0.073
5A	0.484	0.472	0.044	0.09	0.025
5B	0.456	0.444	0.1	0.22	0.027
6A	0.48	0.445	0.075	0.157	0.074
6B	0.507	0.457	0.036	0.071	0.1
7	0.582	0.337	0.081	0.14	0.42
8	0.498	0.468	0.033	0.067	0.06

Results

Summaries of the artifact orientations results are presented in Table 2.4 and Fig. 2.27. With the exception of Layers 5 and 4B, the layers show a nonuniform bearing angle. In nearly all of these cases, the mean angle is to the south or south-southeast. Inspection of the Schmidt-Rose diagrams confirms this general pattern. The one exception is Layer 7, which has a very small sample size. As for plunge angles, all showed a nonuniform distribution, which is normal for archaeological data. In these data, Layer 3A stands out with a relatively high average plunge angle of 23.1°. This is the highest angle we have seen in our combined archaeological data sets. The rest of the angles vary between 8° and 17°.

When the bearing and plunge angles are converted to eigenvalues (Table 2.5) and plotted on the Benn diagram (Figs. 2.28 and 2.29), there is some variability between the

layers. The elevated plunge angles of Layer 3A are obvious in this diagram and pull the point toward the isotropic pole. Layer 3B has high values as well, though not to the extent of Layer 3A. A permutations test (Table 2.6 and Fig. 2.29) indicates that Layers 3A and 3B are different. Additionally, when the 95% confidence interval is considered, it is clear that most of the variability within this layer relates to linearity and not isotropy. The same is true for Layer 4B. There is enough variability and a relatively low sample size to make for a broad 95% confidence interval that includes relatively undisturbed context close to the planar pole to more clearly disturbed context half way to the linear pole. These latter contexts are typically indicative of some downslope movement, due either to solifluction or water transport. As for the latter, the Schmidt-Rose diagram (Fig. 2.27) does not display the typical modal or weakly bimodal pattern typical of water transport. Layers 4C, 5A,

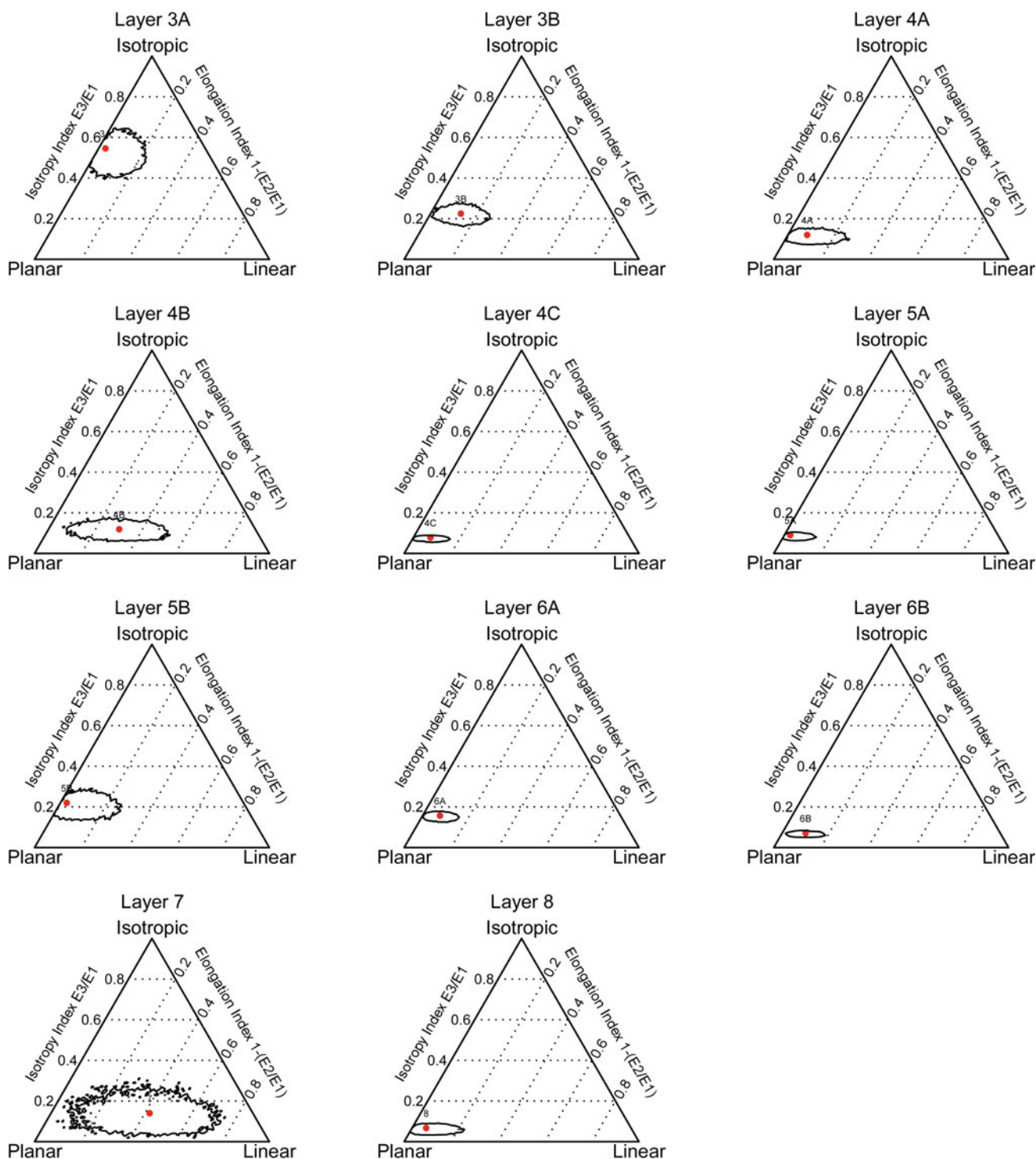


Fig. 2.28 Benn diagrams for each of the Pech IV layers with 95% confidence intervals calculated through resampling with 10,000 iterations

6A, 6B, and 8 are clearly quite close to the planar pole even considering their 95% probability distributions, and the permutations test shows that these layers are statistically indistinguishable from one another. Layer 5B is similar to Layers 5A, 6A and 4C, but it has a bit more isotropy and will

be discussed further at the end of this chapter. Layer 7 has a very large 95% confidence interval reflective of its low sample size and high internal variability. As a result, little can be said of its depositional processes based on the artifact orientations.

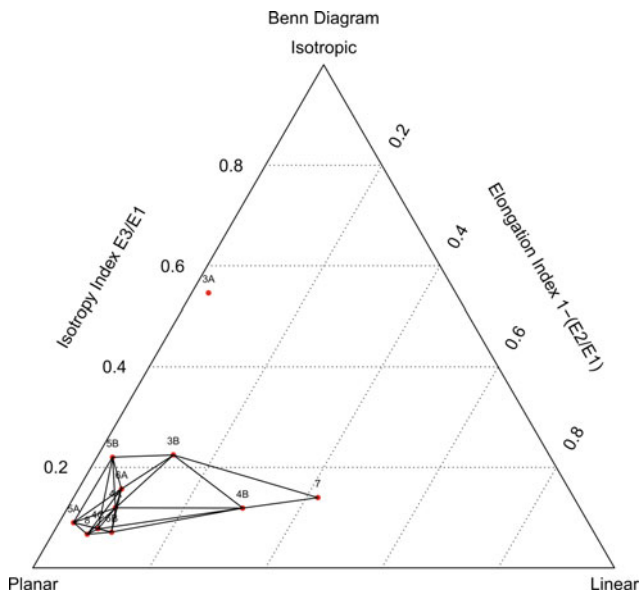


Fig. 2.29 Benn diagram of the Pech IV layers with lines indicating which layers are statistically similar (see Table 2.6)

Some of the above-described variability is spatially patterned (Fig. 2.27). For Layers 3A and 3B, for instance, higher levels of isotropy and linearity are in the southern portion of the excavation. This is where these layers come into contact with Layer 2, which is thought to be reworked Pleistocene material. Additionally, in the southern portion of these surfaces, the deposits are not under the collapse of the Pech IV cave. Perhaps this location resulted in some reworking of these deposits after deposition or perhaps it was the collapse itself that played some role in lifting these sediments. The spatial plots also show that the portion of Layer 4C against the north limit of the excavation, meaning against the cave wall, shows high degrees of linearity. This is likely an example of the so-called “wall effect” common in cave systems where there is water percolation and movement against the cave wall. A comparison of the 95% confidence

interval for Layer 4C and the spatial plot shows that in fact there is a great deal of highly localized variability within the deposit. However, these local pockets of more linear orientations are not systematically aligned enough in one direction to pull the assemblage average away from the planar pole. Layer 5A and 5B show the same wall effect pattern, though to a smaller degree than Layer 4C but with a similar level of internal variability.

Layers 8 to 6A were excavated across a larger surface, and Layer 6 was greatly impacted by large blocks of roof fall, particularly in the south and southeast portions of the excavation. In Layer 6A, these areas are where some linear and more isotropic pockets of artifacts can be found. Layer 6B, however, shows a more limited distribution, with most values having very low levels of isotropy with some pockets of higher levels of isotropy. The Layer 7 sample size is really too small to analyze spatially considering that 40 artifacts are grouped to make an analytical unit, and the layer consists of only 50 artifacts. Layer 8 shows a pattern not unlike Layer 6B.

Edge Damage

Methods

Edge damage is recorded with four intervals: none, 1-surface, 2-surface, and rolled. This approach differs from our study of Combe-Capelle Bas where the 1-surface interval was divided into interior versus exterior damage (Dibble et al. 1995). Assessing whether a piece is edge damaged or not (i.e., “none” vs. the other three categories) has a subjective component, whereas identifying where the damage is located and whether the damage is sufficient to classify the piece as rolled is less subjective. As for the latter, a piece is considered rolled if the edges and flake scar ridges are rounded due to abrasion. One-surface and 2-surface damage refer to whether there is damage on either the interior or exterior surface (1-surface) or on both surfaces (2-surface).

Table 2.6 Pair-wise permutations test Benn statistics for each of the Pech IV layers. Lower values indicate more distance (less probability of two samples coming from the same population)

[illegible]

A piece is considered damaged when there are multiple edge removals typically irregular in shape and size, typically abrupt, and typically noncontiguous (McBrearty et al. 1998).

An effort is made to exclude excavation and curation damage. The latter is likely not a large issue with the assemblages presented here as they were analyzed soon after excavation, and the artifacts were individually bagged. At one extreme, a single ding on an edge or even 2 or 3 very small and dispersed removals (cf. McBrearty et al. 1998) are not enough to be considered edge damage and at the other extreme, it can be difficult to separate edge damage from light scraper retouch. We consider these two cases to be the main area of subjectivity in this classification system. Note that the scale does not vary based on the geological context, that is, these observations are made independent of an object's geological context. Note too that this system does not distinguish pre-depositional use damage from post-depositional damage. An experimental trampling study designed to address this issue (McPherron et al. 2014) demonstrated (a) that edge damage is correlated with edge angles and (b) that all other variables being equal, exterior surfaces show more damage. Unfortunately, this study also demonstrated that size measures are only a weak predictor of edge angles and thus a poor predictor of edge damage. Likewise, as mentioned above, which surface was damaged (interior versus exterior) was not recorded for the Pech IV assemblage. Finally, the damage rates reported here are based on complete and proximal flakes only. Tools are excluded because they are presumably more likely to have use damage in addition to damage induced by trampling and other site formation processes.

Results

A summary of edge damage percentages is presented in Table 2.7. A few aspects are worth noting. First, Layers 8, 6A, 5A, 4C, 4B, 4A, 3B, and 3A are similar with high levels of undamaged pieces (between 66 and 77%). Second, Layer 7 stands in contrast with the lowest percentage of undamaged pieces and a very high percentage of two-surface damage and rolled pieces. Layers 6B and 5B fall in between these two groups, with Layer 5B showing higher levels of damage than in Layer 6B. The pattern in Layer 5B will be discussed below. While there are many possibilities, the pattern in Layer 6B could reflect some mixing of material at the contact between Layers 6B and 7, which was clear but not sharp, it could be the result of the roof fall in this layer, or it could represent increased trampling. As for the former, section plots of the rolled material from Layer 6 do not show that more pieces come from the bottom of the layer, as one would expect if mixing were the cause.

Breakage and Heated Flints

Methods

Lithic breakage rates are easily quantified as the percentage of proximal blanks (retouched and unretouched flakes retaining at least 50% of the platform) in the total sample of blanks (retouched and unretouched proximal and complete flakes):

Table 2.7 Edge damage on complete and proximal flakes. Layer 5B is reported for the whole layer and divided into samples labeled 5B-1 and 5B-2 (see below for an explanation)

Layer	No damage	1 surface	2 surfaces	Rolled	N
3A	77.3	16.7	5.9	0.1	982
3B	70.3	21.7	8.1	0	1685
4A	69.4	18	12.6	0	111
4B	70.4	22.2	7.4	0	27
4C	69.3	23.9	6.9	0	348
5A	66.9	25.6	7.4	0.1	844
5B	38.6	30.7	23.8	6.9	319
5B-1	26	27.3	31.3	15.3	150
5B-2	47.2	33.3	19.4	0	180
6A	66.7	23.2	9.9	0.2	1179
6B	48.2	30.9	19.4	1.5	1111
7	16.4	21.7	46	15.9	1719
8	72	20.1	6.6	1.3	1168

Table 2.8 The percentage of heated flints through the Pech IV sequence

Layer	N unburned	N burned	% Heated
3A	1089	12	1.1
3B	1849	11	0.6
4A	131	1	0.8
4B	31	0	0
4C	404	3	0.7
5A	911	11	1.2
5B	361	3	0.8
6A	1311	61	4.5
6B	1177	72	5.8
7	1813	165	8.3
8	1096	286	20.7

Table 2.9 A comparison of breakage rates in heated and unheated flakes

Layer	Complete blanks (N)	Broken blanks (N)	Ratio	Complete heated blanks (N)	Broken heated blanks (N)	Ratio	Chi-square	P
6A	861	450	1.91	15	46	0.33	42.63	<0.0001
6B	703	474	1.48	18	54	0.33	33.53	<0.0001
7	791	1022	0.77	50	115	0.43	10.99	<0.0001
8	680	416	1.63	124	162	0.77	32.55	<0.0001

$$\text{Breakage Index} = \frac{\text{Proximal Blanks}}{(\text{Proximal Blanks} + \text{Complete Blanks})} * 100$$

However, as is demonstrated below, it is clear that heating either breaks pieces or makes them more susceptible to breakage (or both). Heated lithics are a useful proxy for the use of fire since they are resistant to the kinds of taphonomic processes that might remove other lines of evidence, such as charcoal or heated sediment [e.g., Sandgathe et al. (2011), though it is important to bear in mind that the heat from a fire can alter objects located several centimeters below the fire itself (Aldeias et al. 2016)]. Identification of heating is reasonably straightforward: a lithic is considered heated if pot lids or crazing is present on its surface or on its edges. Color, such as reddening, is a less reliable measure of heating since different materials react differently to heating. Evidence for heating was assessed on all piece-provenienced lithics. Thus, here the frequency of heated artifacts and breakage in heated artifacts is considered as well, and finally the rate of artifact breakage on only the unheated lithics is presented.

Results

A summary of the percentage of heated artifacts is presented in Table 2.8. The frequency of heated artifacts is greatest in Layer 8 and decreases gradually upward. In Layers 5, 4, and 3, heating stays below 1.2%; Layer 6, which is dark colored

and contains burned bones on the East Section contains approximately 5% heated lithics. These data also show that heated artifacts are more likely to be broken (Table 2.9). Therefore, to control for this factor, the breakage patterns are presented here (Table 2.10) with heated artifacts removed from the calculation.

Even with heated artifacts removed, breakage rates are highest in the lower portion of the section. Layer 7 again clearly stands apart from the rest with elevated levels of broken artifacts. Above and below Layer 7, the rate drops below 50%, and in the rest of the sequence, breakage rates are between roughly 25 and 35%.

Small Finds

Methods

As discussed in Chap. 3, all sediments from the layers reported here were water screened through two size fractions: 2 and 6 mm. Each water-screened sample comes from one bucket of sediment excavated typically over an area equivalent to one-quarter meter square (though not necessarily aligned with square boundaries). Buckets are filled to a standardized volume of seven liters unless a layer change is encountered in which case they are closed prior to being full. Stones larger than 10 cm in maximum dimension are not included in the bucket volume. In our experience, depending

Table 2.10 The percentage of complete flake blanks along with their size measurements and two shape ratios

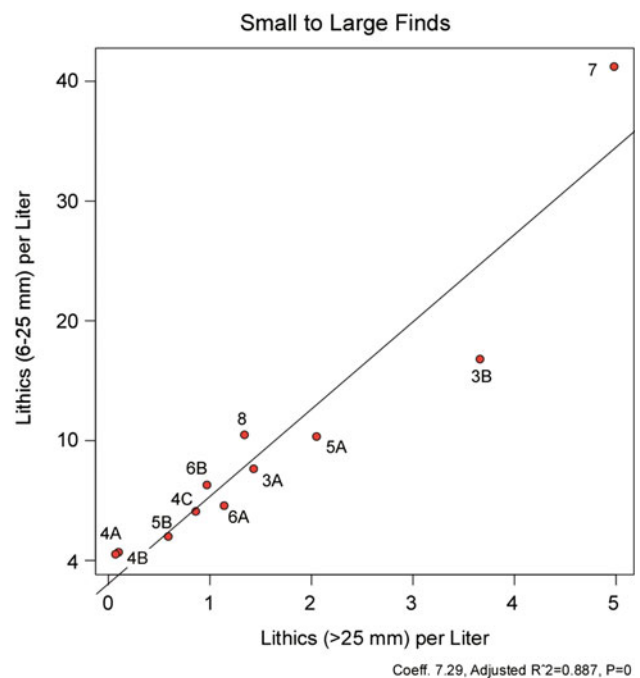
Layer	Complete blanks	Proximal blanks	% complete	Length (mean)	Width (mean)	Thickness (mean)	Refinement (mean)	Elongation (mean)
3A	828	273	75.2	33	23.7	8.1	2.9	1.4
3B	1344	516	72.3	33.1	23.6	7.1	3.3	1.4
4A	98	34	74.2	36.8	27.3	7.7	3.6	1.4
4B	26	5	83.9	39	27.6	8.7	3.2	1.4
4C	282	125	69.3	36.6	26.4	6.9	3.8	1.4
5A	654	268	70.9	37.8	24.2	6.4	3.8	1.6
5B	228	136	62.6	39.1	25.8	7.7	3.3	1.5
6A	876	496	63.9	39.8	26.8	7.2	3.7	1.5
6B	721	528	57.7	33.8	24.6	7.2	3.4	1.4
7	841	1137	42.5	34.2	24.3	8.5	2.9	1.4
8	804	578	58.2	36.5	24	6.1	3.9	1.5

on the number of stones larger than 10 cm and on sediment compaction, a 5 cm spit excavated over a quarter meter square corresponds to roughly 2.5 buckets. Buckets are provenienced by recording a point at the center of the excavated area once the bucket is full.

To assess Bordes' excavation techniques, we excavated, screened, and analyzed in exactly the same manner 87 buckets of sediment from his backdirt. An analysis of these data is presented here.

For Combe-Capelle Bas, the small fraction (2–5 mm) was analyzed (Kluskens 1995), but at subsequent sites that we excavated this fraction was not analyzed (but all of these samples are now archived in the MNP). These data are not discussed further here. For the large fraction (6–25 mm), the material was sorted into bones versus stones and treated separately. For the stone artifacts, we passed the large fraction through a set of stacked sieves with sizes of 20, 16, and 10 mm resulting in four size classes (20–25, 16–20, 10–16, and 6–10 mm), which were counted and weighed.

The analyses presented here are based solely on the stone data. In preparing this data set, artifacts that should have been piece provenienced (i.e., artifacts larger than 25 mm), have been removed from the small finds and included in the large find counts. Similarly, provenienced artifacts smaller than 25 mm were removed from the lithic analyses by giving them a special code ("toosmall"), and in the analyses presented here these pieces have been reintegrated into the small finds data set when layer totals are provided but not integrated when considering small finds on a bucket by bucket basis. The reason for this is that in our excavation system at that time piece-provenienced lithics were not easily associated with a particular bucket. Note that generally, there are relatively few such finds, particularly in relation to the overall sample size. In Layer 8, for instance, 84 small flakes were incorrectly provenienced (due to their

**Fig. 2.30** A plot of the density of large lithic finds (>25 mm) per liter versus small lithic finds (6–25 mm) per liter by layer

small size) from a total of 27,736 small flakes contained in the 6–25 mm fraction.

Results

Variability in the small finds from Pech IV can be analyzed in comparison to the large finds and internally using the data from the stacked screens. With regard to the former, it has been shown experimentally that the distribution of size

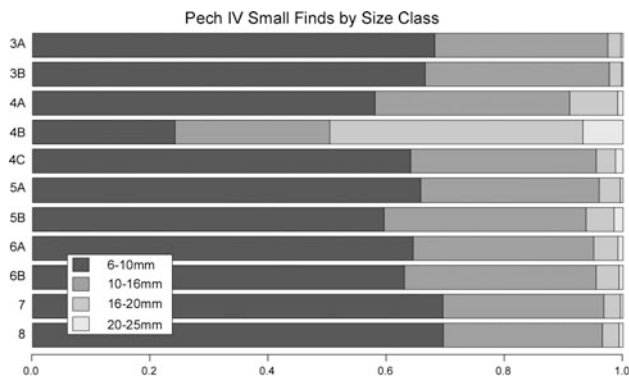


Fig. 2.31 The proportion of various size classes with the 6–25 mm lithics fraction recovered from the screens

classes is not effected by reduction intensity or raw material size (Lin et al. 2015). It is clear, however, that various site formation processes do affect size distributions. At Pech IV the ratio of large finds to small finds per liter show a highly linear relationship (Fig. 2.30). Layer 3B has proportionally more large flakes and Layer 7 has proportionally more small ones, and both layers have relatively high artifact densities in comparison with the other layers. This was already clear from excavation of these units, especially Layer 7, which other measures and the geological observations presented here have shown underwent severe post-depositional disturbance. With regard to internal variability in size classes (i.e. within the 6–25 mm fraction), with the exception of Layer 4B, the data show very similar distributions throughout the sequence (Fig. 2.31).

Setting aside Layer 4B for the moment, what is interesting about these data is perhaps *not* what they tell us of site formation processes, but how little they vary considering the amount of variability in lithic technology that exists in the sequence. For instance, Layers 3A and 3B, which show similar distributions and display the presence of biface production, have relatively low retouched tool counts, and have a blank technology based on Levallois and discoidal approaches. The Layer 3 distribution, however, is very similar to that of Layer 8, which has a high percentage of retouched tools and a high incidence of Levallois, and to Layer 7, which is difficult to describe technologically because it is so broken and damaged due to cryoturbation. The industries of Layer 6 are characterized by low tool production but an increased production of small flakes using a variety of techniques including Levallois (Dibble and McPherron 2006). These small flakes drop below the 25 mm size cut-off for proveniencing artifacts, and it perhaps shows in the size class distributions with the larger flakes being slightly more numerous than in, for instance, Layer 8. However, Layers 5B through 4C, which plot similarly to Layer 6, do not show an emphasis on small flake production,

but they do show evidence of Levallois technology and a return to retouched tool production. Layer 4A represents an entirely different technology of blank production (Quina) with very high retouched tool frequencies and very little evidence of on-site blank production (see Chap. 6). Thus, as was shown experimentally already (Lin et al. 2015), we are not able to see a relationship between technology and small flake distributions in our data.

The pattern in the one outlier, Layer 4B, is interesting. The technology of this layer is intermediate between that of Layers 4C and 4A, but the size class distribution is not suggestive of a mix of the two layers. The smallest size class (6–10 mm) shows a deficit, which is consistent with the selective removal of small finds by water. The artifact orientations for this layer show a rather high level of linearity and especially a high contrast to Layers 4A and 4C, which have very low linearity. Linearity (or bimodality) is also consistent with water flow. However, there is no apparent evidence for running water that is observable in the thin sections (e.g., sample 28, Fig. 2.19b; sample 49B, Fig. 2.20b), so perhaps the size distribution may be a result of artifact import, rather than removal of material.

Note that in terms of large (>25 mm) artifact densities and small (6–25 mm) find densities, Layer 7 shows several patterns distinct from the rest of the sequence. Both the number of large lithic artifacts per liter (5.0) and small lithic artifacts per liter (50.2) are far greater than any other layer at the site. This is not surprising given the high level of breakage. However, when breakage—including heat-related breakage—is corrected for in the large artifact data by considering only platform flakes and tools, the artifact density (2.3 per liter) is still at the high end of the range for the site as a whole, but below that of Layer 3B (2.3). Additionally, the ratio of small to large lithics (10.08), while at the high end, is within the range of variation seen within the sequence.

Discussion

The stratigraphy, general nature of the deposits and site formation based on artifact analyses are discussed above. Here, we turn to a discussion of the field and microscopic observations that contribute to understanding the entire site history, including geogenic and anthropogenic aspects of site formation.

The thin sections from Pech IV show that the quartz and carbonate sand, as well as larger limestone fragments are derived from breakdown of the quartz-rich limestone bedrock. This conclusion is based on the clear similarity in grain size, sorting, and roundness of the loose quartz in the matrix to the quartz in the limestone. In addition, most minor coarse fraction components such as glauconite and mica are also

found as trace components in the limestone bedrock. Many micromorphology samples reveal fragments of limestone that are actively dissolving and contributing quartz sand to the sediment in situ (dissolving limestone is distinguished by its undulating grain edges). Some fragments also weather internally and contain vughs and infillings of fine material, or coatings of reddish brown iron-rich clay. In some samples, the carbonate component of the limestone was completely dissolved, leaving behind a residuum of quartz sand, and some muscovite and glauconite. Therefore, the origin for nearly all of the coarse sediments in the site is ultimately the cave environment.

A volumetrically minor component of the fine sediment fraction is also derived from limestone weathering and the breakdown of its insoluble components. This material is represented by weathered glauconite and muscovite grains, as well as silt-sized grains of iron (Fe) and manganese (Mn) oxides, which are partially responsible for giving many of the deposits a redder color (Fig. 2.6). In addition, some of the Fe/Mn fraction observed in the groundmass also originated from the relict Tertiary soils and deposits on the plateau (*sidérolithique*; Texier [2009]). Finally, a more significant factor in imparting the red color is the formation of reddish brown dusty clay coatings in voids and on grains. These coatings are widespread in the Pech IV deposits, but are particularly well developed in the East Section and in deposits in squares D and E in the West Section.

Many thin sections also display post-depositional calcium carbonate that occurs as localized fine micritic root coatings (Figs. 2.18a and 2.22f); they can also be found as isolated individual coatings or as aggregated ones (e.g., Figs. 2.21c, 2.22e and 2.25a–c). In the case of the latter, the surrounding matrix is well indurated, and it is possible to observe on the West Section a broad zone of cemented deposits (Fig. 2.4a). This zone includes Layers 4 and 3 from squares H through F11 and as such, they appear to indicate locations of previous driplines: they give the impression of migrating upward and northward toward the back of the cave (see Fig. 2.4a). It is worth noting that the calcification of the rootlets is generally the last diagenetic event because, for the most part, the rootlets developed after the formation of most Fe-rich dusty clay coatings. However, in some instances both seem to have precipitated alternately, as Fe-rich zones are precipitated or formed on carbonate, which are then later pierced by calcified roots (Fig. 2.18a).

Another, rather different type of secondary carbonate occurs at the base of Layer 8 (sample 54, square E13—Fig. 2.11c–f), which in the field appeared as a large well-indurated block of “breccia”, with bone, many pores, and calcite hypocoatings. Visible in thin section are cm-sized clasts of limestone, quartz sand, and bone tightly cemented with microsparite (Fig. 2.11e–h). In addition, acicular microsparite needles coat voids (Fig. 2.11c–f), some

of which exhibit previous coatings of iron-rich dusty clay. This sample (54), which rests on bedrock, appears to have been cemented with calcite by water flowing on the bedrock, which at the same time was favorable environment for root growth as shown by the numerous vesicles and chambers that perforate a dense matrix (Fig. 2.11c).

The composition and both internal organization and external geometry of the anthropogenic components provide clear evidence that burning events occurred during deposition of Layer 8 and possibly Layer 6. Layers 8–6 all show elevated percentage of heated flints. These burning events, exemplified by the intact stringers of ash overlying carbon-rich layers, likely correspond to the round combustion structures excavated in 2002.

The fissures present in some of the cemented layers indicate that the cementation likely occurred relatively soon after deposition and not much later. On the other hand, Layer 8 also exhibits features associated with carbonate dissolution: as mentioned above, many limestone fragments appear to be actively dissolving and many cemented ash fragments often contain thin channel voids, which are characteristic of calcite depletion (Bullock et al. 1985). Compared to Layers 5 through 1, however, carbonate in the lowest layers is relatively well preserved. This preservation may result from the physical protection and groundwater buffering capacity of the limestone roof blocks of Layer 6B. In any case, the ashes, which are primarily composed of calcite, do not show any signs of secondary phosphatic diagenesis as is the case at Roc de Marsal (Goldberg et al. 2012). In fact, secondary phosphatization was extremely rare in any of the samples.

Trampling

Most of the bone fragments visible in thin section are typically equant to rectangular in shape. However, some of the elongated ones—particularly in Layer 8—are fractured but contiguous and conjoinable (Figs. 2.9e, f and 2.10a, d), features that point to clear evidence of trampling (Goldberg et al. 2012; Miller et al. 2010). Such trampling supports the intensive fire activity demonstrated by the superposed hearth and rake-out layers in Layer 8. This activity also seems to be localized at the cave entrance, just inside the extant dripline at the time. On the other hand, trampling certainly occurred in overlying layers that were away from the entrance, but the lack of appropriate sediments (mostly gravel, pebbles and sand with few bones) preclude their traces from being preserved, or at least evident. In terms of edge damage on lithics, the amount of damage seen in Layer 8 is typical of most of the layers at the site, with only some other layers showing higher amounts of damage (particularly Layers 7, 6B and 5B). In any case, trampling of varying intensity in Layer 8 may also contribute to the compact nature of the ash

layers, as well as to mixing of burned and unburned bones, ashes, and limited charcoal within the layer. In addition to trampling, such episodes of mixing may also have been produced by hearth rake-out activities, whereby the remains of existing hearths were spread out laterally from their original location, providing a substrate for the next fire episode. In this regard, as pointed out above, we note that the thickest part of Layer 8 appears in squares H/I 14 and trends SW from there (Figs. 2.2, 2.3a, c and 2.5b,c).

Depositional Processes

Micromorphological and field evidence indicate relatively few depositional processes operating at Pech IV, although as pointed out above, we have excavated only at what was the former entrance and its immediate surroundings. The most important source of sediment is the bedrock, which furnishes a variety of clasts, the most striking of which are roof fall in the form of large slabs that are concentrated at the entrance of the cave (Fig. 2.4a). These large spalls are dramatic, and as pointed out above, they began to accumulate in Layer 6 in the central part of the cave (Sq. F and G) with initial collapse of the overhanging ceiling. With time, successively larger decimeter-sized slabs fell from the ceiling toward the direction of the entrance where we witness an accumulation of imbricated slabs that prograded outward to the south (Figs. 2.3a–c and 2.5d): blocks in Layer 6 occur in square G14, whereas those in Layers 5 and 4 can be found in squares G14–J14 and H14–K14, respectively. Less volumetrically important are smaller, cm-sized blocks that are particularly abundant in Layer 4 and in the southern part of Layer 3 (Figs. 2.3a–c and 2.4a).

The dislodging of the limestone clasts from the roof is presumably a combined effect of chemical and physical weathering. The accumulation of the larger slabs, however, while likely fostered by weathering, more readily represent instability of the roof as it was weakened by initial collapse in Layer 6 time. However, eventually its configuration as a relatively thin, overextended roof protruding from the cliff face (see present-day Pech I for a modern analogy) produced the “internal exfoliation” of collapse from the interior outward (Fig. 2.32). It is worth stressing here that at the time of accumulation of the large slabs of Layers 5 and 4, the entrance to the cave was somewhat obstructed, and occupation took place in a restricted space between the back wall to the north and the large slabs of roof fall to the south.

The finer fraction (predominantly quartz sand and limestone pebbles) was liberated by dissolution of the bedrock, accumulated initially by gravity. However, lateral transport took place by solifluction, as can be seen in the field by sharp contacts between layers, especially between Layers 5B/6 and 3B/4 (Fig. 2.3a–c); in addition, many of the cm-sized clasts

in these units are well rounded (see above; e.g., Figs. 2.12, 2.13c, 2.9b–c, 2.19a, d and 2.20b). Moreover, movement on a smaller (granular scale) was likely accomplished through the action of frost/soil creep (Bertran et al. 1997; van Vliet-Lanoë 1985; Vliet-Lanoë 1982).

Other fine materials are derived from red soils and sediments on the plateau (*sidérolithique*) that have been incorporated into the sedimentary fill via colluviation and gravity. Moreover, a significant part of the red color in the sediments from the East Section (Fig. 2.7b)—and particularly close to the bedrock walls in the West Section (the so-called “wall effect”; Fig. 2.7c)—is a result of weathering/dissolution of the bedrock (e.g., iron-rich minerals such as glauconite), as well as translocations of iron-rich dusty clay that coat voids and grains (e.g., Figs. 2.9c, f and 2.18a, d, e). The iron-rich reddish coatings are strongest against the north wall (Figs. 2.3b and 2.7a) where water would naturally concentrate, leading to preferential dissolution here. But dusty iron-rich coatings occur away from the wall so their origin is more likely associated with dripping water from the roof or perhaps some slight runoff that allows for translocation of the detrital silty clay. It is not clear whether these wall effects were of sufficient intensity to account for the linearity seen in the artifact orientations along the north wall as well.

As stated above, most of the Pech IV sediments were generated internally from dissolution of bedrock leading to the deposition of coarse (cm- to dm-sized) limestone clasts and finer cm-, granule-, and sand-sized quartz and limestone grains; during excavation several pieces of travertine were recovered (e.g., square E11). These lines of evidence support the concept that Pech IV is a collapsed cave and is analogous to the situation visible at Pech I, ~80 m to the NW (Fig. 2.1b). As the hillslope eroded slightly obliquely to the axis of the jointing and Pech de l’Azé karstic system, the overhangs of both caves were destabilized, resulting in the collapse of the cave roof as outlined above—at Pech IV first as internal collapse starting with Layer 6 and later by the retreat of the brow. This retreat is recorded in the microstratigraphy as secondary calcite accumulations that appear to migrate northward and stratigraphically upward through time. Final roof collapse resulted in the reduction of the overhang to a few meters, traces of which are visible on the West Section of the current excavations. Remains of the overhang are more prominent in the East Section where the roof collapse is thicker and appears to represent a final collapse that took place *after* many of the layers had already been deposited (see Figs. 2.7a, b and 2.8). In passing, it is interesting to note that the retreat of the cave towards grid northwest means the current excavation sampled an ever-changing location relative to the dripline.

During his excavations, Bordes observed evidence in his Level J₁ (our Layer 5A) of cryoturbation in the form of rounded limestone blocks and damaged flints (see also

Chap. 1), both of which appeared to be more pronounced in the front of the site. In the field and in thin section, cryoturbation is generally conveyed by rounded limestone pebbles and distinct artifact inclination and mixing (see above). Interestingly, in Pech II cryoturbation was visible as pockets of rounded/abraded pebbles in Layer 4D (also Layer 5 and “X”; (Bordes 1972; Laville et al. 1980); other micromorphological evidence at Pech II for cold climate features was illustrated by silty cappings and coatings on grains, as well as ice lensing (Goldberg 1979). Although some of the layers at Pech IV do contain rounded fragments of limestone, micromorphological observations do not reveal similar types or degrees of reorganization of the fine fraction into cappings as at Pech II; some dusty clay cappings can be seen at Pech IV but they are relatively muted in comparison to those of Pech II. This lack of microscopic expression of cold climate suggests that rounded limestone blocks from Layer 6 were possibly not rounded in situ through freeze–thaw, as is the case at Pech II. Rather, they could be reworked from older non-prehistoric, possibly phreatic gravels from inside the cave.

On the other hand, the distribution of limestone clasts in Layer 5 and the abundance of relatively fresh micro-éboulis (cm-sized limestone grains) are suggestive of solifluction (Bertran and Texier 1999). Evidence in support of this can also be found in the archaeological measures of site formation processes in Layer 5B. The artifact orientations show higher levels of isotropy than the layers immediately above and below. There is also an elevated percentage of rolled pieces (6.9%). When the distribution of rolled pieces is plotted (Fig. 2.33), it is clear that they are not distributed throughout the layer but rather form a lens within it. This lens was not noticed and isolated during excavation. Therefore, here a 2D kernel density estimate is applied to the projected Y and Z coordinates of the rolled pieces, and a 0.5 contour interval on the resulting density matrix is used to isolate the lens (Layer 5B-1) from the rest of the layer (5B-2). With these two subsamples, some archaeological site formation indicators can be compared. As shown in Table 2.11 and Fig. 2.34, the artifacts of subsample 5B-1 show a much higher level of linearity in their orientations. The sample size for subsample 5B-1 is low ($N = 43$); however, in this case permutations test show that while the 95% confidence intervals do overlap to some extent, the two samples (5B-1 and 5B-2) are statistically distinct at the $p < 0.05$ level. Next, with regard to edge damage, sample 5B-1 shows a lower percentage of undamaged pieces and a higher percentage of pieces with damage on two surfaces (Table 2.12). This is unsurprising, as generally in our data sets two-surface damage is elevated in assemblages with elevated rolled pieces, but it further confirms the integrity and the associated differences in site formation processes

affecting the two subsamples. Finally, breakage levels are higher in subsample 5B-1 (Table 2.13), but the difference is not significant ($X^2 = 2.41$, $p = 0.12$).

Because Pech IV was occupied during a series of climatic fluctuations (Jacobs et al. 2016), it is interesting that the sediments do not record more evidence of past environments. Although cold climate features, such as ice lensing require both cold temperatures and a source of moisture in order to form, they also need fine material to retain water. Thus, a reasonable explanation of the differences in expression of micromorphological features between Pech II and IV may be related to differences in sediment grain size: the Pech II sediments are generally finer and contain more clay- and silt-sized particles, which enable the development and preservation of freeze–thaw textures because they retain moisture and inhibit water drainage. Hence, at Pech IV the paucity of finer groundmass and predominance of coarse sediment (sand-through pebble sizes) may, therefore, not preserve most macroscopic expressions of climate processes. Whereas roof collapse and the deposition of limestone blocks have also been linked to climatic processes—specifically cold and dry periods (Laville et al. 1980)—their specific interpretations are not clear. Thus, although the deposits at Pech IV contain both large roof blocks and smaller clastic contributions that may in a general way reflect climate, nothing more definitive can be said at this point.

Sequence of Formation

When occupation of Pech IV began, the morphology of the site was more consistent with a cave than a rockshelter. The earliest deposition was primarily anthropogenic in nature (Table 2.14; Fig. 2.31). Activity took place directly on the exposed surface of the bedrock. This activity included the deposition of anthropogenic materials (e.g., bone, lithics, char, some charcoal, ashes) mixed with natural cave detritus (e.g., quartz sand, some silt). Most ash is present as stringers and cemented ash grain clusters, which implies an interesting sequence of events. The ash was likely deposited in several thin layers corresponding to ephemeral hearth-like features or single rake-out events. Immediately after deposition, gravitational settling and other sedimentary processes caused some unconsolidated ash to filter through the sediment profile and shelter nearby large grains. The remaining ash layers were quickly cemented by (drip or soil?) water. After cementation, the ash layers were fractured by trampling, and some of the sediments became mixed, possibly during later hearth rake-out activities. The ash fragments were then subjected to some calcite dissolution, as evidenced by the development of voids (vughs) and a few highly porous fragments.

Layer 7 marks a major cold event as shown by its cryoturbated structure. Moreover, it contains a rather rich lithic assemblage dominated by heavily damaged, rolled, and abundant broken pieces but without the differential removal of a particular size class. This latter point makes water transport unlikely. The artifact densities are comparable to those in Layer 3B, a layer that shows little post-depositional alteration. Bone densities in Layer 7 are the lowest in the Pech IV sequence and may be a result of these same post-depositional processes.

The first major roof fall event (Layer 6B) produced massive, flat-lying blocks of limestone that protected the combustion features from further trampling and acted as a chemical buffer that saturated groundwater in carbonate before it reached the lowest layers. This saturated water perched above the bedrock and locally cemented the bottom of Layer 8.

The first roof collapse event likely changed the morphology of the cave to a more open spatial configuration, as the sediments immediately above the limestone blocks contain iron and quartz concretions of subsurface pedogenic origin (Fig. 2.31). Combustion activities may have continued for a short period or shifted in location, as evidenced by the burned bones of Layer 6 on the East Section and by the continued presence of heated lithics in this layer. The resulting sediments were not protected from carbonate dissolution, however, and the only remnants of these activities are burned bones, heated lithics, and occasional small fragments of charcoal. The large roof fall concentrated in squares D–E–F–G 11–12–13–14 is also contemporaneous with noncalcareous sand accumulation from inside the cave system. A thin activity surface was deposited before a second collapse. Following this second collapse, accumulation of massive sand continued, punctuated by smaller roof falls (individual blocks), spreading to G–H 11–12–13–14. The northern squares (D–E–F 11–12–13–14) experienced

marked erosion of Layer 6A followed by infilling of stony sand. Strong inclination of the surface in E–F 11 combined with chaotic orientation of stones and thickening of Layer 5B in square G11 suggest a possible solifluction lobe banked up against the roof fall. Although this feature is not visible in microscale, an analysis of artifact orientations, breakage, and edge damage shows a feature with Layer 5B that is consistent with this interpretation. This phase (Layer 5) marks the last major period of block collapse at the entrance (squares I, J, K) and the beginning of a different mode of collapse: the backward retreat of the brow towards the north. At this point, the morphology of the site becomes more like a rockshelter than a cave. Again, the above scenario shows that retreat of cave overhang towards grid northwest indicates that our excavation samples from bottom to top represent a changing location relative to the dripline.

We can surmise that once the cave began to collapse during the onset of Layer 6, the surface of the deposits was periodically covered with snow. Thus, whereas much of the sedimentary infill is composed of breakdown products of the limestone bedrock with initial sedimentation by gravity, snowmelt must have played a part in mobilizing what was lying on the ground. Initially in Layer 6 time, a sloping surface was inherited from or conditioned by the bedrock floor, which slopes up to the north (Figs. 2.3a–c and 2.4a). This slope, though slight, was enough to cause movement of the sediment by solifluction or soil/frost creep, which explains many of the features observed in thin sections (e.g., granular, loose nature of the fabrics). In addition, the presence of water and percolation beneath former surfaces in the past would also encourage weathering of the material on the surface, leading to the formation of red iron-rich dusty clay coatings and cappings seen on many of the grains.

Reddish brown silty clay accumulates in the north part of the site, while imbricated roof blocks mark the retreat of the brow in the south (Fig. 2.31). Cemented zones in the

Table 2.11 Eigenvalues and Benn shape ratios for the sublevels of Layer 5B

Level	E1	E2	E3	IS	EL	N
5B-1	0.555	0.334	0.111	0.2	0.397	43
5B-2	0.49	0.421	0.089	0.181	0.141	152

Table 2.12 Edge damage for the sublevels of Layer 5B. Rolled is removed because it is the basis of separating the two sublevels

	None	Interior	Exterior	Exterior/interior	N
5B-1	30.7	7.9	25.2	36.2	27
5B-2	47.2	11.7	21.1	20	180

Table 2.13 The percentage of complete flakes for the sublevels of Layer 5B

	Complete	Proximal	% complete
5B-1	108	74	59.34
5B-2	136	65	67.66

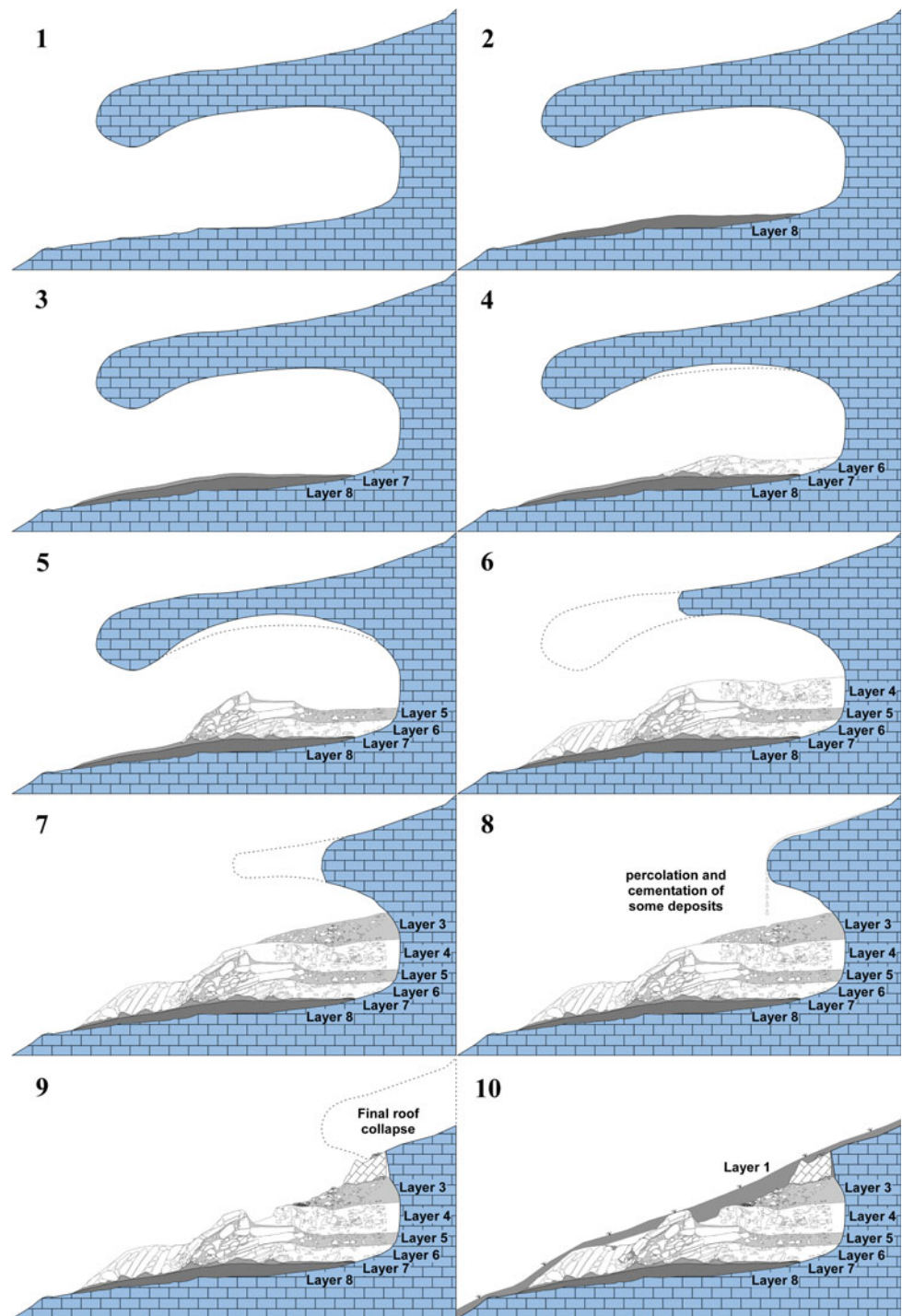
Table 2.14 Summary of Pech de l'Azé IV history

Phase	Layer	Events
1	8	Anthropogenic accumulation of bones, ash, char and organic matter, and inwashing of sand from interior of cave and with little rock fall. Some intact hearths, but mostly laterally displaced combustion materials as a result of hearth rake out or simply trampling. The anthropogenic deposits thin laterally toward the north and south and are thickest just inside the former position of the brow, which trended ENE/WSW. They are deposited directly on bedrock and are well indurated and calcite-cemented at the base by water trapped at bedrock/sediment interface
2	7	Influx of heavily abraded/rolled (cryoturbated) flints in sandy matrix. Subsequent deformation by rock fall of Layer 6 hinders our ability to determine if Layer 7 was originally of uniform or variable thickness (i.e., whether it took the form of a solifluction lobe). Although no inclination of the layer was observed, it is reasonable to assume it was derived (in part) from the direction of the interior of the cave. Flat contact at base. Upper part is irregular and eroded by Layer 6, resulting in variable thickness of layer. <i>Brief cold period?</i>
3	6B	Accumulation of large slabs of rock fall in squares D–E–F–G 12–14, which are mostly broken along bedding planes and originate from the central part of the then-extant cave roof. Coevally, (corresponding to the base of Layer 6B) some sandy deposits began to accumulate by disaggregation of the roof and soil/frost creep, particularly near the north wall. Anthropogenic inputs of burned bones, particularly in the East Section. Rounded limestone clasts with cappings suggest cryoturbation and weak freeze–thaw. <i>Possible climatic significance = cold with alternating freeze–thaw?</i> alternating freeze–thaw, although this is not supported by the faunal analyses
4	6A	Continued deposition of homogeneous, massive sand by soil/frost creep that is penecontemporaneous with deposition of angular slabs of rock fall in square E12 and large blocks in squares F–G 12, 13, and 14; the latter continue to fall from the interior of the cave ceiling, producing an imbricated structure, with successive blocks being deposited further out toward the entrance. Local overtopping of large blocks by sand. <i>Same conditions as Layer 6B</i>
5	5B 5A	Loose blocks continue to fall in squares G–H 11–12–13–14. To north (squares D–E–F 11–12–13–14) marked erosion of Layer 6A by Layer 5B followed by deposition of calcareous disaggregated limestone sand and rounded by soil/frost creep or solifluction. Stones are fresh and tend to be well rounded but they are flatter and more angular in square C closer to the wall. Strong dip/inclination of surface in E–F 11 toward the W. Chaotic orientation of stones and thickening of Layer 5B in square G11 point to distal part of solifluction lobe banked up against the roof fall to the south, and associated with stone lifting. With time, the clasts become more angular and flatter. Dispersed mm- to cm-sized rounded and angular burned bone fragments indicate reworking of anthropogenic inputs; no intact burning features were observed
7	3A 3B	Accumulation of fine gravel (some angular but mostly rounded) in a sandy matrix that are eroded into Layer 3B with a sharp contact. It contains rare larger, fist-sized pieces of roof fall, and extends basically from squares D to F. Artifacts are also bedded and tend to follow the dip, although some are on edge. The roof at this time seems to have been above the F line, as the sediment in these squares is cemented. The cave was nearly full at this time, and the deposits came close to the level of the ceiling. This layer appears to represent fine-grained solifluction of the geological sediments, but the artifacts are quite sharp and fresh, so no or little transport of the flints seems to have occurred [it is also possible that because the matrix is so fine grained, that artifacts are not abraded]. Bone and limestone clasts have thin Mn coatings representing presence of water, perhaps associated with former dripline These deposits are laterally truncated by a channel situated under the then-extant drip line that is later filled in by Layer 2
8	2	Cutting and filling of channel into Layers 3A and 3B beneath the then-extant overhang, situated over squares E and F. It is filled with cm-sized pieces of bedrock consisting of both angular blocks and rounded cobbles produced by roof retreat and slumping from the adjacent hillslope, as well as also reworking of Layer 3A material that slumped in from the side of the channel
9		Final collapse of remaining nub of roof above square D11 as shown on the W section by the pivotal rotation of the large tilted block at the top of the section that is close to the present bedrock back ledge of the cave. On the E Section, this last phase of collapse is shown by thick accumulation of large slumped blocks of roof that also seal the deposits
10	1A 1B 1C	Medieval (?) erosion of slope, coupled with colluviation of cm-sized rocks in dark brown organic clay sand

sediments represent positions of former drip lines, which move northward with each collapse event. Truncation and erosion of Layer 4A by angular gravelly sand with a sharp contact indicates possible cryoclastism. These cold climate deposits are laterally truncated by a channel that formed from flowing water under the then still extant drip line. Deposition of Layer 2 fills the channel with cm-sized pieces of bedrock consisting of both angular blocks and rounded

cobbles produced by roof retreat and slumping from the adjacent hill slope. This layer also contains some reworking of Layer 3A material that slumped in from the side of the channel. During historic times, final slumping of roof occurred, as shown by the rotation of the roof block above square D11. Final erosion of the slope, coupled with colluvial accumulation, buried the site by cm-sized rocks in dark brown organic clay sand.

Fig. 2.32 Evolution of Pech de l'Azé IV



Integrity of the Archaeological Record

As noted above, the geological dynamics described above show that sediments are essentially locally derived and transported and that any transport was local, i.e., confined to

the immediate environs of the site itself. The vast majority originated from the limestone as roof fall and disaggregation products; only small contributions from the plateau (e.g., *sidérolithique*) were noted. Furthermore, lateral transport was confined to creep, which mobilized sediments on the

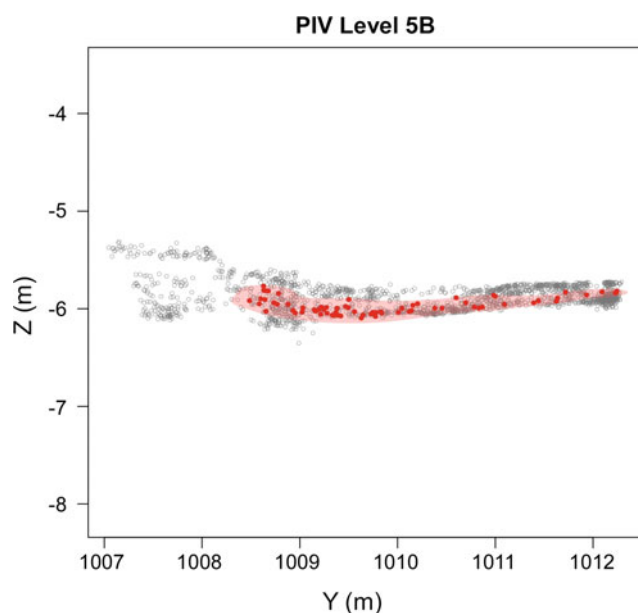


Fig. 2.33 The distribution of rolled lithics in Layer 5B as shown from a sagittal section view. The *red line* represents a kernel density estimate of the rolled pieces. All artifacts that fall within this *red line* are labeled as 5B-1. The remaining artifacts are 5B-2

granular scale. Some solifluction was noted in Layers 5B, 4C, and 3B. Although the artifact orientations suggest some re-alignment of the artifacts with the orientation of the cave system, there is no evidence from the various observations presented here of massive reworking of the archaeological material. A few layers show some substantial post-depositional disturbances (particularly Layer 7 and parts of Layer 5), but these appear to have modified the assemblages very locally and essentially in place, if at all. In other words, such processes did not likely result in substantial artifact transport: sediments moved but the artifacts did not.

The relatively widespread use of fire in Layer 8 did not change the displacement of artifacts to a major extent, as was the case at Roc de Marsal (Aldeias et al. 2012). Trampling did result in comminution of bone and perhaps mm to cm vertical displacements of artifacts, and rake out possibly moved artifacts over a surface in the order of perhaps cm or dm; probably not more than that since individual lenses in Layer 8 are at the most 30 cm across. On the other hand, in the lower layers, fire resulted in increased levels of breakage, inflated small find counts, and burned bones.

Concluding Comments

Geoarchaeology and site formation at Pech IV were evaluated using detailed field observations, soil micromorphology, and attribute analysis of the lithic finds, including their

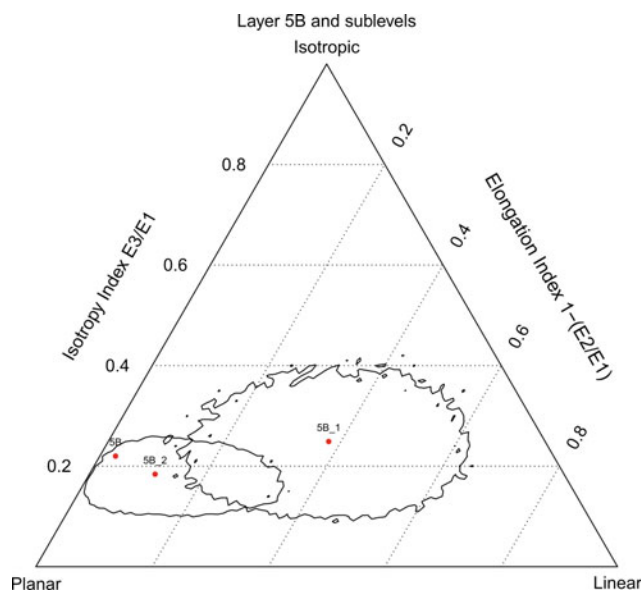


Fig. 2.34 Benn diagram for Layer 5B complete and the sublevels of Layer 5B. The boundaries on 5B-1 and 5B-2 represent 95% confidence intervals. A permutations test shows them to be statistically distinct

orientations, size, density, and breakage characteristics. In addition to updating Bordes' stratigraphy, we now have a clearer understanding of the site history and formation processes.

Layer 8—and to some extent, Layer 6 (particularly in the East Section)—is characterized in the field by its dark color and bedded anthropogenic components. These include chert, burned bone, char, and ashes, which are preserved to some extent as intact lenticular combustion structures, but mostly as redistributed components through the action of hearth rake out. These combustion structures represent isolated events, as we do not tend to find superposition of intact hearths one directly on top of another.

Whereas both intact hearths and associated sediments occur throughout Layer 8, sediment thickness is arranged in a linear west-northwest trend that generally parallels the position of the former brow of the cave, and occupation appears to have occurred just inside of the dripline, where we observe in thin section numerous examples of trampling. Thus, although Layer 8 is characterized by burning activities, they are not distributed evenly throughout the cave space or specifically through time, as the top of Layer 8 appears to be richer in organic matter and ashes, although the latter occur as both intact lenses and reworked clasts of cemented ashes. Numerous attempts were made to excavate the Layer 8 sediments using *décapage* technique but, owing to the thin, lenticular nature of the combustion features and their redistribution by rake out, it was impossible to follow surfaces over more than the scale of centimeter. The intact lenticular nature of the hearths are reminiscent of some of

those at Hayonim and Kebara Caves (Israel) (Goldberg and Bar-Yosef 1998) and like virtually all Middle Paleolithic hearths are not associated with rock paving or enclosures.

Observations of the site's morphology and setting, as well as the location, bedding inclinations and directionality of the lithics, data demonstrate that the site is in fact a remnant of a phreatic cave system (similar to Pech I and II): it was breached by backward erosion of the valley, which cut the phreatic tube diagonally. This type of erosion resulted in the overhang that Bordes observed and which gave the impression of the site being a rockshelter.

Overall, our stratigraphic subdivisions broadly match those of Bordes, although there is not a one-to-one correspondence. This is not surprising, as his subdivisions were based on a mix of lithological and typological attributes. Furthermore, based on lithostratigraphy and comparative lithic analysis between his collections and ours, we were able to link the East and West Sections, thereby showing that contemporaneous occupations occurred throughout the excavated space. We are not dealing with two separate "sub-sites."

The most striking evidence for Neanderthal use of fire is found within Layer 8, with its large quantities of highly burned bone and lithic contents, ash and char. The amount of burned bone and lithics decreases in Layer 6, which is still dark colored, and drops off dramatically above that. Nevertheless, micromorphological analysis showed the presence of burned bone in Layers 5A, 4A, and 3A. They occur in these upper layers without any association of combustion features, charcoal, or ashes. At the moment, they demonstrate that fire was used—even though apparently to a very low extent in these layers, but without any other associated burned materials, it is difficult to assess what their implications for fire are at the site. As the bone fragments in these upper samples are in low concentrations, it is likely that they were not heated in place but rather that they were derived from somewhere relatively close by, perhaps on the order of meters away. Nevertheless, burned bone counts from the layers, more or less mirror the observation of burned bones observed in thin sections.

The high degree of isotropy in Layer 3A is intriguing and unique. The micromorphology shows a number of the limestone clasts with a variety of orientations and a high degree of bioturbation as reflected in the porosity. Moreover, a greater degree of trampling in this part of the site does not seem likely as Layer 3 has the lowest amount of rolled pieces. The reasons for this amount of isotropy remain unclear.

Overall, there is no *striking* evidence for climate change within the deposits except for the clear cryoturbation in Layer 7 and solifluction in Layer 5B. In addition, there are some cappings in the deposits, but they are sporadic and not well developed. As mentioned, the lack of ice lensing or

other indicators of cold climates are not present, likely due to the lack of fine material in the sediments.

References

- Aldeias, V., Dibble, H., Sandgathe, D., Goldberg, P., & McPherron, S. (2016). How heat alters underlying deposits and implications for archaeological fire features: A controlled experiment. *Journal of Archaeological Science*, 67, 64–79.
- Aldeias, V., Goldberg, P., Sandgathe, D., Berna, F., Dibble, H., McPherron, S., et al. (2012). Evidence for Neandertal use of fire at Roc de Marsal (France). *Journal of Archaeological Science*, 39(7), 2414–2423.
- Arpin, T. L., Mallol, C., & Goldberg, P. (2002). Short contribution: A new method of analyzing and documenting micromorphological thin sections using flatbed scanners: applications in geoarchaeological studies. *Geoarchaeology—An International Journal*, 17(3), 305–313.
- Benn, D.I. (1994). Fabric shape and the interpretation of sedimentary fabric data. *Journal of Sedimentary Research*, 64(4), 910–915.
- Berna, F., & Goldberg, P. (2008). Assessing Paleolithic pyrotechnology and associated hominin behavior in Israel. *Israel Journal of Earth Sciences*, 56, 107–121.
- Bertran, P., Héty, B., Texier, J.-P., & Van Steijn, H. (1997). Fabric characteristics of subaerial slope deposits. *Sedimentology*, 44(1), 1–16. doi:10.1111/j.1365-3091.1997.tb00421.x.
- Bertran, P., & Texier, J.-P. (1999). Facies and microfacies of slope deposits. *CATENA*, 35(2–4), 99–121.
- Bordes, F. (1972). *A tale of two caves*. New-York: Harper & Row Publishers.
- Bordes, F. (1975). Le gisement de Pech de l'Azé IV: Note préliminaire. *Bulletin de la Société Préhistorique Française*, 72, 293–308.
- Braillard, L. (2000). La dynamique de mise en place et l'évolution du remplissage de l'abri sous roche Sur-les-Creux à Tanay (Vouvy VS). *Bulletin de la Murithienne*, 118, 41–58.
- Bullock, P., Fedoroff, N., Jongerius, A., Stoops, G., Tursina, T., & Babel, U. (1985). *Handbook for soil thin section description*. Wolverhampton: Waine Research.
- Capdeville, J. P., & Rigaud, J. P. (Cartographer). (1987). Notice Explicative de la Feuille Sarlat-la-Canéda à 1/50 000.
- Courty, M.-A., Goldberg, P., & Macphail, R. I. (1989). *Soils and micromorphology in archaeology*. Cambridge: Cambridge University Press.
- Dibble, H., Lenoir, M., Holdaway, S., Roth, B., & Sanders-Gray, H. (1995). Techniques of Excavation and Analysis. In H. Dibble & M. Lenoir (Eds.), *The middle paleolithic site of Combe-Capelle Bas (France)* (pp. 27–40). Philadelphia: University of Pennsylvania, University Museum Press.
- Dibble, H., & McPherron, S. (2006). The missing mousterian. *Current Anthropology*, 47(5), 777–803.
- Goldberg, P. (1979). Micromorphology of Pech-de-l'Azé II sediments. *Journal of Archaeological Science*, 6, 1–31.
- Goldberg, P., & Bar-Yosef, O. (1998). Site formation processes in Kebara and Hayonim Caves and their significance in Levantine prehistoric caves. In T. Akazawa, K. Aoki, & O. Bar-Yosef (Eds.), *Neandertals and modern humans in Western Asia* (pp. 107–125). New York: Plenum.
- Goldberg, P., & Berna, F. (2010). Micromorphology and context. *Quaternary International*, 214(1–2), 56–62.
- Goldberg, P., Dibble, H., Berna, F., Sandgathe, D., McPherron, S., & Turq, A. (2012). New evidence on Neandertal use of fire: Examples from Roc de Marsal and Pech de l'Azé IV. *Quaternary International*, 247(1), 325–340.

- Goldberg, P., & Macphail, R. I. (2003). Strategies and techniques in collecting micromorphology samples. *Geoarchaeology*, 18(5), 571–578.
- Goldberg, P., & Macphail, R. I. (2006). *Practical and theoretical geoarchaeology*. Oxford: Blackwell Publishing.
- Jacobs, Z., Jankowski, N., Dibble, H., McPherron, S., Soressi, M., Sandgathe, D., et al. (2016). The age of three Middle Palaeolithic sites: single-grain optically stimulated luminescence chronologies for Pech de l'Azé I, II and IV in France. *Journal of Human Evolution*, 95, 80–103.
- Karkanas, P., Rigaud, J.-P., Simek, J. F., Albert, R. M., & Weiner, S. (2002). Ash bones and guano: A study of the minerals and phytoliths in the sediments of Grotte XVI, Dordogne, France. *Journal of Archaeological Science*, 29(7), 721–732.
- Kluskens, S. L. (1995). Archaeological taphonomy of Combe-Capelle Bas from artifact orientation and density analysis. In H. Dibble & M. Lenoir (Eds.), *The Middle Paleolithic Site of Combe-Capelle Bas (France)* (pp. 199–243). Philadelphia: The University Museum Press.
- Laville, H., Rigaud, J.-P., & Sackett, J. (1980). *Rock shelters of the Périgord*. New York: Academic Press.
- Ligouis, B. (2006). Jais, lignite, charbon et autres matières organiques fossiles: Application de la pétrologie organique à l'étude des éléments de parure et des fragments bruts. In J. Bullinger, D. Leesch, & N. Plumettaz (Eds.), *Le site magdalénien de Monruz, volume 1: premiers éléments pour l'analyse d'un habitat de plein air. Archéologie neuchâteloise* (Vol. 33, pp. 197–216). Neuchâtel: Service et musée cantonal d'archéologie.
- Lin, S.C., McPherron, S.P., & Dibble, H.L. (2015). Establishing statistical confidence in Cortex Ratios within and among lithic assemblages: A case study of the Middle Paleolithic of southwestern France. *Journal of Archaeological Science*, 59, 89–109.
- Lund, U., & R port by Claudio Agostinelli. (2012). CircStats: Circular statistics. (2012). S-plus original. Retrieved from <http://CRAN.R-project.org/package=CircStats>.
- Madella, M., Jones, M. K., Goldberg, P., Goren, Y., & Hovers, E. (2002). Exploitation of plant resources by Neanderthals in Amud Cave (Israel): The evidence from phytolith studies. *Journal of Archaeological Science*, 29(7), 703–719.
- McBrearty, S., Bishop, L., Plummer, T., Dewar, R., & Conard, N. (1998). Tools underfoot: Human trampling as an agent of lithic artifact edge modification. *American Antiquity*, 63(1), 108–129.
- McPherron, S.J. (2005). Artifact orientations and site formation processes from total station proveniences. *Journal of Archaeological Science*, 32(7), 1003–1014.
- McPherron, S., & Dibble, H. (2007). Artifact orientations from total station proveniences. In A. Figueiredo & G. Velho (Eds.), *The world is in your eyes*, pp. 161–66. Tomar, Portugal: CAA.
- McPherron, S., Dibble, H., & Goldberg, P. (2005). Z. *Geoarchaeology*, 20(3), 243–262.
- McPherron, S., Braun, D. R., Dogandžić, T., Archer, W., Desta, D., & Lin, S. C. (2014). An experimental assessment of the influences on edge damage to lithic artifacts: A consideration of edge angle, substrate grain size, raw material properties, and exposed face. *Journal of Archaeological Science*, 49, 70–82.
- Meyer, D., Zeileis, A., & Hornik, K. (2014). vcd: Visualizing categorical data. R package version 1.3–2.
- Miller, C. E., Conard, N. J., Goldberg, P., & Berna, F. (2010). Dumping, sweeping and trampling: experimental micromorphological analysis of anthropogenically modified combustion features. *P@lethnologie: Revue francophone en Préhistoire*. <http://www.palethnologie.org>.
- Salomon, J.-N., & Astruc, J.-G. (1992). Exemple en zone tempérée d'un paléocryptokarst tropical exhumé (la cuvette du Sarladais, Dordogne). In J.-N. Salomon & R. Maire (Eds.), *Karsts et évolutions climatiques* (pp. 432–447). Bordeaux: Presses Universitaires de Bordeaux.
- Sandgathe, D., Dibble, H., Goldberg, P., McPherron, S., Turq, A., Niven, L., et al. (2011). On the role of fire in Neandertal adaptations in Western Europe: Evidence from Pech de l'Azé and Roc de Marsal, France. *PaleoAnthropology*, 216–242.
- Soressi, M., McPherron, S., Lenoir, M., Dogandžić, T., Goldberg, P., Jacobs, Z., et al. (2013). Neandertals made the first specialized bone tools in Europe. *PNAS*, 110(35), 14186–14190.
- Stoops, G. (2003). *Guidelines for analysis and description of soil and regolith thin sections*. Madison, WI: Soil Science Society of America.
- Team, R.C. (2014). R: A language and environment for statistical computing. Vienna, Austria: R Foundation for Statistical Computing.
- Texier, J.-P. (2009). *Histoire géologique de sites préhistoriques classiques du Périgord une vision actualisée la Micoque, la grotte Vaufrey, le Pech de l'Azé I et II, la Ferrassie, l'abri Castanet, le Flageolet, Laugerie Haute*. Paris: Édition du Comité des travaux historiques et scientifiques.
- Turq, A., Dibble, H., Goldberg, P., McPherron, S., Sandgathe, D., Jones, H., et al. (2011). Les Fouilles Récentes du Pech de l'Azé IV (Dordogne). *Gallia préhistoire*, 53, 1–58.
- van Vliet-Lanoë, B. (1985). Frost effects in soils. In J. Boardman (Ed.), *Soils and quaternary landscape evolution* (pp. 117–158). Chichester: Wiley.
- Villagran, X. S., Schaefer, C. E. G. R., & Ligouis, B. (2013). Living in the cold: Geoarchaeology of sealing sites from Byers Peninsula (Livingston Island, Antarctica). *Quaternary International*, 315, 184–199.
- Vliet-Lanoë, B. V. (1982, 1981 March 2–6). *Structures et Microstructures Associées à la Formation de Glace de Ségrégation: Leurs Conséquences*. Paper presented at the Fourth Canadian Permafrost Conference, Calgary, Alberta.

The Middle Paleolithic Site of Pech de l'Azé IV

Dibble, H.L.; McPherron, S.J.P.; Goldberg, P.; Sandgathe, D.M. (Eds.)

2018, XXIV, 236 p. 149 illus., 43 illus. in color.,

Hardcover

ISBN: 978-3-319-57522-3